３．結　論

3.1　高周波数遮断特性の高精度化

東日本で発生したスラブ内地震や海溝型地震の大地震および中小地震を対象に，観測記録にみられる高域遮断フィルターの検討を行なった．

対象としたスラブ内地震は全 27 地震で，その M_J の範囲は 4.1～7.0，震源深さの範囲は 56～77km である．解析対象地震には 2003 年 05 月 26 日 18 時 24 分に宮城県沖で発生した M_J 7.0（震源深さ 70km）が含まれる．この大地震については，高域遮断周波数 f_{max} 9.1Hz，べき乗数 s 1.02，その他の中小地震の高域遮断周波数 f_{max} は 9~25Hz，べき乗数 s は 0.77~3.14 と推定された．

対象としたプレート境界地震は全 18 地震で，その M_J の範囲は 4.5～7.2，震源深さの範囲は 37～51km である．解析対象地震には 2005 年 8 月 16 日 11 時 46 分に宮城県沖で発生した M_J 7.2（震源深さ 42km）等，M_J が 6.0 を越える地震が 3 地震含まれる．2005 年 8 月 16 日 11 時 46 分の大地震については，高域遮断周波数 f_{max} 9.7Hz，べき乗数 s 0.98，中小地震の高域遮断周波数 f_{max} は 9~23Hz，べき乗数 s は 0.98~2.20 と推定された．

高域遮断周波数 f_{max} の値の地震規模依存性および応力パラメータ依存性について検討を行なった．スラブ内地震，プレート境界地震ともに，地震規模の大きな地震，応力パラメータが大きい地震は f_{max} の値が小さくなる傾向が一般的に認められるが，さらなるデータの蓄積が必要であろう．

最後に，M_J 6.0 程度以上の大地震の高域遮断フィルターについて，既往研究事例を含めて比較を行なった．その結果，大地震の高域遮断周波数 f_{max} の値は一部を除いて 7～9Hz 程度であり，地震タイプや地域による顕著な差は認められなかった．べき乗数 s の値は 0.8～1.8 の範囲に分布しているが，地殻内地震については比較的小さく，スラブ内地震やプレート境界地震はやや大きいという特徴があるように思われる（表 3.1-1, 図 3.1-1～図 3.1-3 参照）．

今後とも，さらなる検討を進めていく必要があると考えられる．

表3.1-1　大規模地震の高域遮断フィルター

地殻内地震		スラブ内地震		プレート境界型地震	
2003年宮城県北部地震 本震 (M_J：6.4)	$P(f)=\frac{1}{\sqrt{1+\left(\frac{f}{8.0}\right)^{2\times0.93}}}$	2001年芸予地震 本震　(M_J：6.7)	$P(f)=\frac{1}{\sqrt{1+\left(\frac{f}{7.8}\right)^{2\times1.51}}}$	2011年東北地方太平洋沖地震 本震 (SMGA1) (M_w：8.1)	$P(f)=\frac{1}{\sqrt{1+\left(\frac{f}{7.0}\right)^{2\times1.37}}}$
	$Q(f)=60.0\times f^{0.95}$		$Q(f)=147.0\times f^{0.88}$		$Q(f)=104.7\times f^{1.02}$
2005年福岡県西方沖地震 本震 (M_J：7.0)	$P(f)=\frac{1}{\sqrt{1+\left(\frac{f}{6.5}\right)^{2\times0.90}}}$	2004年紀伊半島南東沖地震 (前震,2004.9.5 19:7) (M_J：7.1) (本震, 2004.9.5 23:57) (M_J：7.4)	$P(f)=\frac{1}{\sqrt{1+\left(\frac{f}{7.7}\right)^{2\times1.69}}}$	2011年東北地方太平洋沖地震 本震 (SMGA3) (M_w：8.3)	$P(f)=\frac{1}{\sqrt{1+\left(\frac{f}{5.7}\right)^{2\times1.37}}}$
	$Q(f)=112.0\times f^{0.70}$		$Q(f)=149.2\times f^{1.00}$		$Q(f)=104.7\times f^{1.02}$
2008年岩手・宮城内陸地震 本震 (M_J：7.2)	$P(f)=\frac{1}{\sqrt{1+\left(\frac{f}{9.4}\right)^{2\times0.84}}}$	2004年紀伊半島南東沖地震 余震 (2004.09.07 08:29) (M_J：6.5)	$P(f)=\frac{1}{\sqrt{1+\left(\frac{f}{7.9}\right)^{2\times1.83}}}$	2011年東北地方太平洋沖地震 本震 (SMGA5) (M_w：7.8)	$P(f)=\frac{1}{\sqrt{1+\left(\frac{f}{8.4}\right)^{2\times1.02}}}$
	$Q(f)=60.0\times f^{0.95}$				$Q(f)=104.7\times f^{1.02}$
福島県浜通り正断層型地震 (2011.04.11 17:16) (M_J：7.0)	$P(f)=\frac{1}{\sqrt{1+\left(\frac{f}{8.0}\right)^{2\times0.78}}}$	2004年紀伊半島南東沖地震 余震 (2004.09.08 23:58) (M_J：6.5)	$P(f)=\frac{1}{\sqrt{1+\left(\frac{f}{5.0}\right)^{2\times1.54}}}$	2011年東北地方太平洋沖地震 余震 (2011.03.12 22:15) (M_J：6.2)	$P(f)=\frac{1}{\sqrt{1+\left(\frac{f}{7.4}\right)^{2\times0.84}}}$
	$Q(f)=70.8\times f^{0.97}$		$Q(f)=149.2\times f^{1.00}$		$Q(f)=104.7\times f^{1.02}$
富士山付近を震源とする地震 (2011.03.15 22:31) (M_J：6.4)	$P(f)=\frac{1}{\sqrt{1+\left(\frac{f}{8.5}\right)^{2\times1.65}}}$	2003年宮城県沖の地震 (2003.5.26 18:24) (M_J：7.0)	$P(f)=\frac{1}{\sqrt{1+\left(\frac{f}{9.1}\right)^{2\times1.02}}}$	2002年宮城県沖の地震 (2002.11.03 12:37) (M_J：6.3)	$P(f)=\frac{1}{\sqrt{1+\left(\frac{f}{12.2}\right)^{2\times1.31}}}$
	$Q(f)=53.3\times f^{0.75}$		$Q(f)=110.5\times f^{0.87}$		$Q(f)=93.0\times f^{0.89}$
		＊2011年東北地方太平洋沖地震本震のSMGA1，SMGA3，SMGA5は入倉・倉橋(2011)のそれぞれに対応している．		2005年宮城県沖の地震 (2005.08.16 11:46) (M_J：7.2)	$P(f)=\frac{1}{\sqrt{1+\left(\frac{f}{9.7}\right)^{2\times0.98}}}$
					$Q(f)=93.0\times f^{0.89}$
		＊＊赤文字：本業務における結果		2005年宮城県沖の地震 (2005.12.02 22:13) (M_J：6.6)	$P(f)=\frac{1}{\sqrt{1+\left(\frac{f}{9.5}\right)^{2\times1.51}}}$
					$Q(f)=93.0\times f^{0.89}$

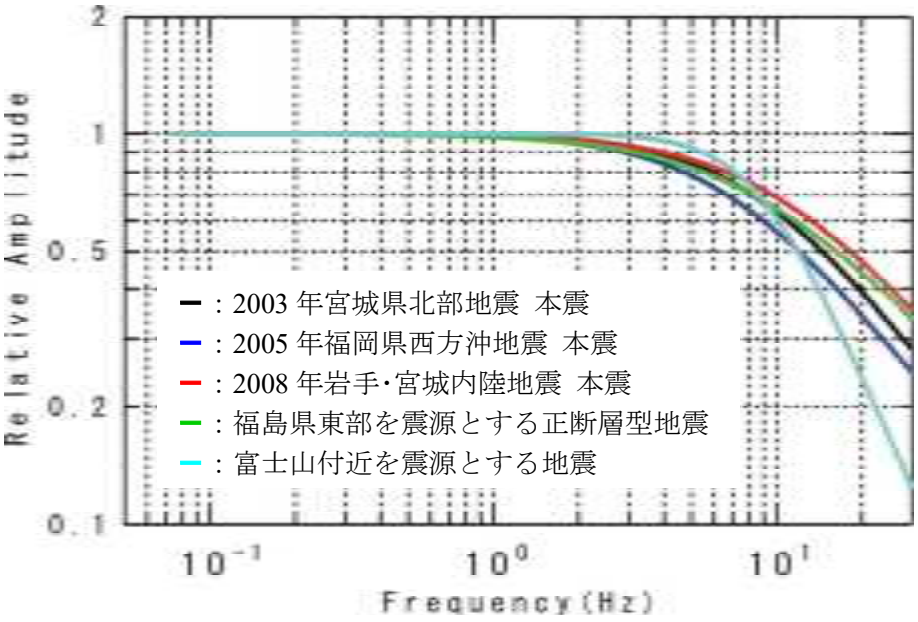

図 3.1-1　高域遮断フィルター（地殻内地震）

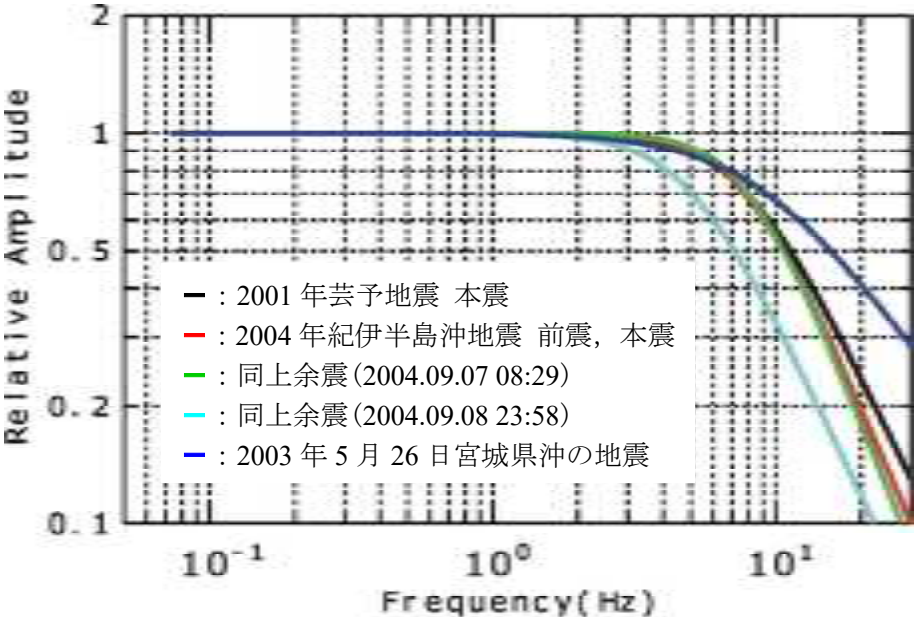

図 3.1-2　高域遮断フィルター（スラブ内地震）

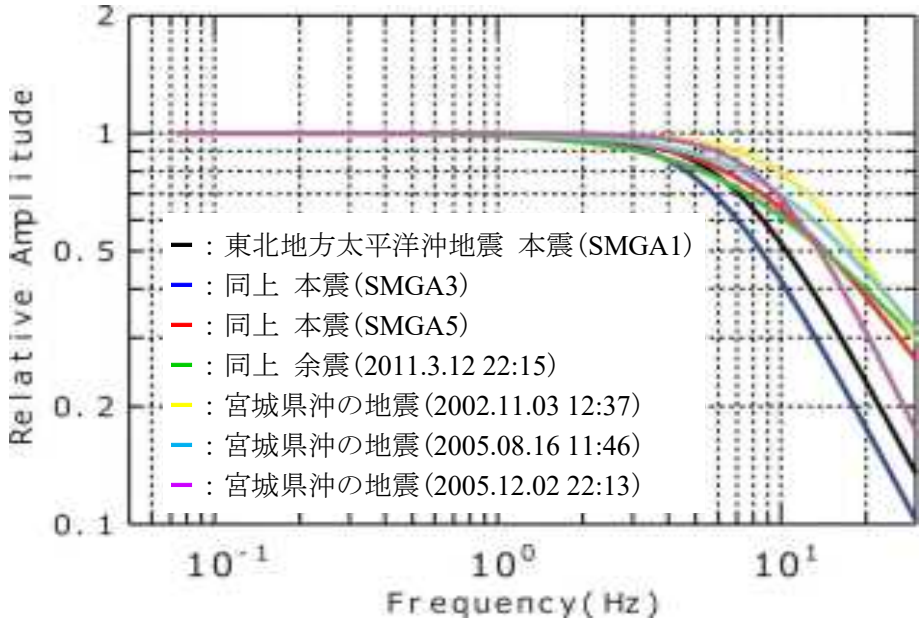

図 3.1-3　高域遮断フィルター（プレート境界地震）

3.2　広帯域地震動予測のための東北地方太平洋沖地震の震源モデルの高度化

3.2.1　特性化震源モデルによる強震動評価（長周期帯域）

2011 年東北地方太平洋沖地震の震源モデルの高度化のため，周期 10 秒程度まで精度のあるグリーン関数を構築し，中長周期帯域まで精度のあるグリーン関数を用いた震源インバージョンを目指す．この震源インバージョン結果に基づき，特性化震源モデルを作成し，M9 クラスの強震動予測手法の適用性について検討を行うことを目標とした．まず，15 観測点について小地震を用いて速度構造モデルを改良した．この改良した速度構造モデルを用いてグリーン関数を計算し，周期 10－100 秒の地震動を説明する震源モデルを逆解析で求めた（図 3.2.1）．以前の速度構造モデルを用いたものよりも，今回改良したモデルでは，ABIC 最小値の示す震源モデルが良好な結果を示した．また，破壊過程は海溝沿いで破壊開始後 110 秒以降にも破壊が進むという，やや複雑で，その信頼性に吟味が必要という結果となった．

得られた震源モデルから，最終すべり分布から求めたアスペリティ領域と，最大モーメントレート密度分布から求める HRA 領域をそれぞれ取り出し，観測波形への寄与を調べた．その結果，断層深部で切り出された HRA は，宮城県付近の特徴的な強震動をかなり説明する．強震動を説明する領域として，従来からのすべり量分布からはこの領域は切り出されていないことから，このような地震では，HRA で取り出すことが重要であることが明かになった．一方，海溝沿いのアスペリティは地震動波形への影響はあまり大きくないという結果が得られた．これは，強震動予測ではこの領域からの地震動はあまり重要ではないことを示していると同時に，海溝沿いの大すべり域の信頼性については観測点カバレッジを広げるなどして，より慎重に検討する必要があることを示している．また，福島県以南の観測記録をアスペリティあるいは HRA で説明できていない．これらの問題のため，現状では有効な特性化震源モデルを構築するに至っていない．

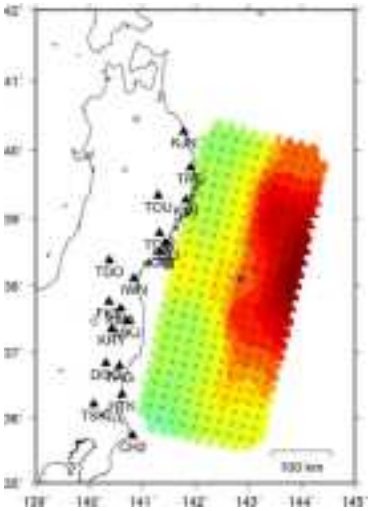

図 3.2.1-1　最終すべり量分布を地図上に投影したもの．

3.2.2　特性化震源モデルによる強震動評価（短周期帯域）

本検討では,短周期帯域の強震動予測手法として広く利用されている統計的グリーン関数法に赤澤･他(2009)による非定常地盤増幅特性の概念を導入し，2011 年東北地方太平洋沖地震の観測波形のシミュレーションを行った。そして，周期数秒以下の短周期帯域（0.5～10Hz）の強震動評価を通じて手法の適用性を検証した。震源モデルには，川辺・釜江(2013)と Kurahashi and Irikura(2013)によりにより提案された SMGA モデルを利用した（前者を川辺モデル，後者を倉橋モデルと称する）。

シミュレーション結果の一例を図 3.2.2-1 に示す。非定常地盤増幅特性を用いた場合のシミュレーション波形は振幅スペクトルのみを用いた場合と比較して後続波の継続時間が長くなり，地震観測記録の特性を良く再現することができた。この結果は，非定常地盤増幅特性により，地盤増幅特性の位相特性が適切に評価された効果であると考えられる。時刻歴波形の振幅の大きさに着目すると，比較的地盤が良質である観測点でのシミュレーション波形は，地震観測記録の振幅を比較的良好に再現することができた。これらの結果は，非定常地盤増幅特性を導入した統計的グリーン関数法が，周期数秒以下の短周期帯域で有用であることを示している。

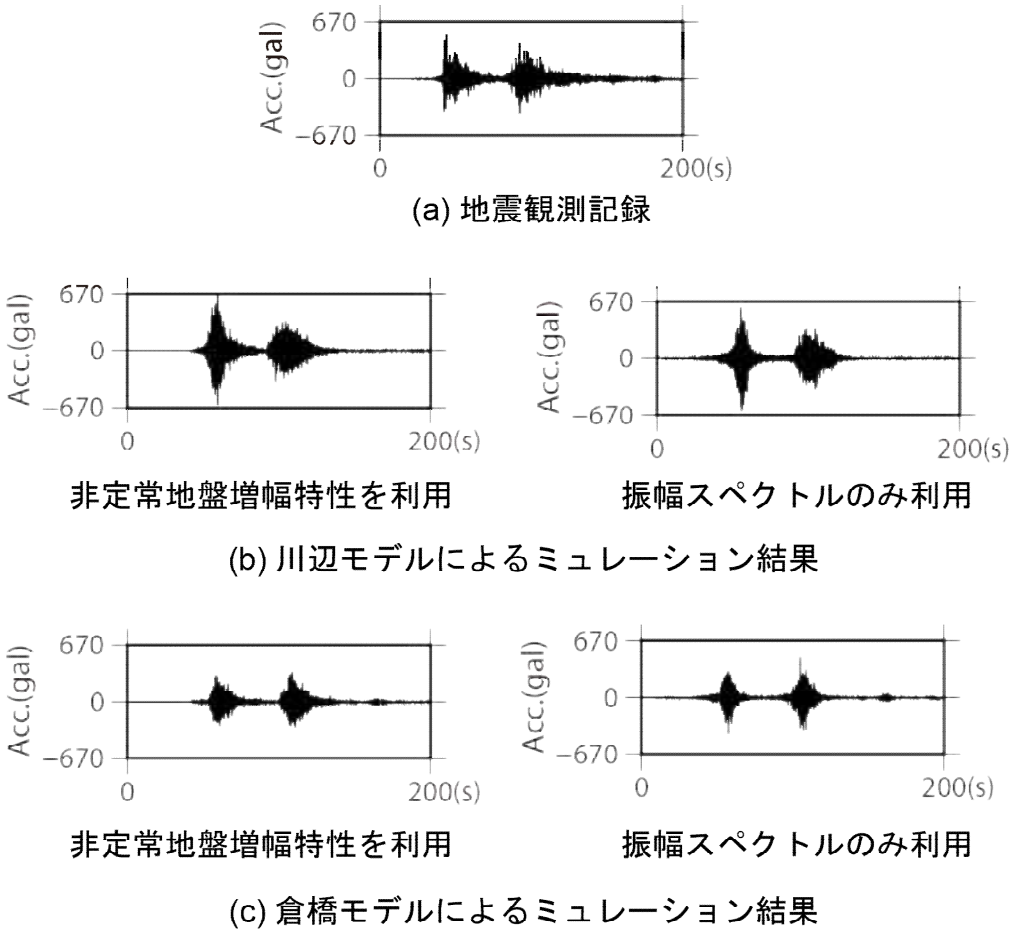

図 3.2.2-1　シミュレーション結果の一例（MYGH12 の NS 成分）

3.3　動力学的シミュレーションによる巨大海溝型地震の特性化の検討

我々は地球物理学的観測結果を取り込んで，2011 年東北沖地震を対象にすべり弱化摩擦則を用いた 2 次元と 3 次元の動力学破壊シミュレーションを実施した。計算結果から以下のことが明らかになった。（１）破壊エネルギーが断層傾斜方向（深さ方向）で異なる。（２）海溝側の浅い部分の応力は弱く，そのため大きなすべりが生じる（高周波数の地震動生成が小さい)。（３）臨界すべり量が浅い部分と深い部分で異なる（浅い部分と深い部分での地震動の周波数帯が異なる)。このモデルでは，破壊は海溝側の浅い部分に到着し，次に逆の深い方向へ破壊が進展することが確認できた。また，浅い部分から深い部分で地震動生成の周波数帯域が変動することも確認できた（図 3.3－1 参照)。

本研究において，2 次元計算と 3 次元計算における初期条件の相違が難しい問題として残っている。しかしながら，本検討の結果は次のステップの成果に繋がると考える。すなわち，昨年度計算した疑似動力学的な巨大地震サイクル・シミュレーションと一致する動力学的な破壊シミュレーション結果を出すことは重要であろう。さらに，3 次元の動力学的シミュレーションのプログラムにおいて，観測波形と比較可能な合成地震動を計算するための 3 次元速度構造モデルの導入準備もできている。

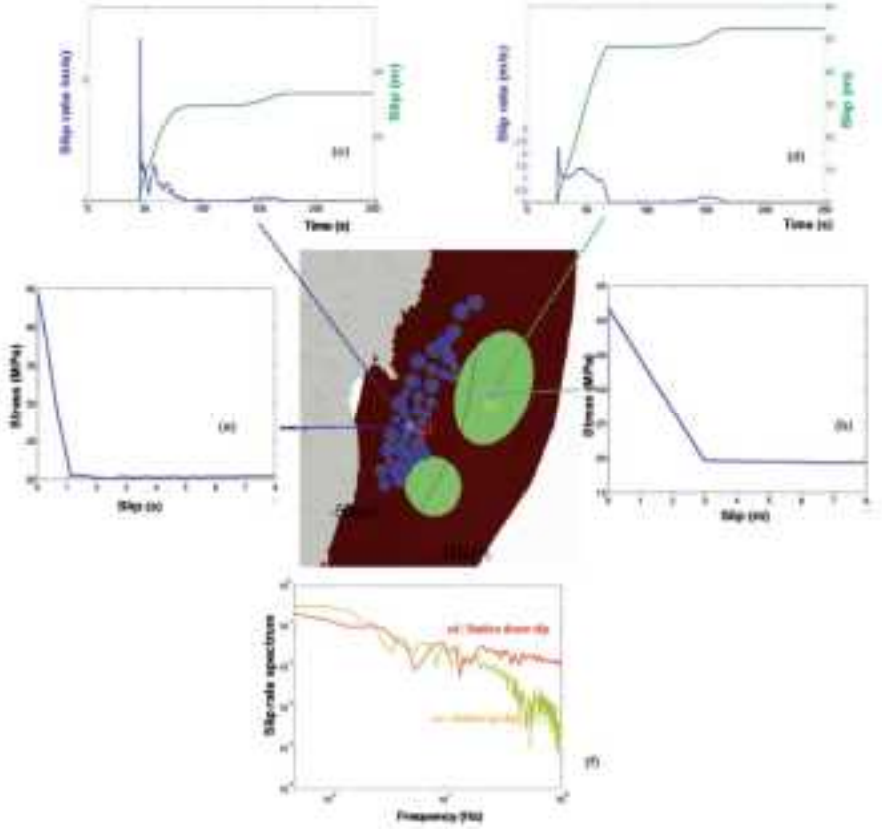

図 3.3－1　浅い大きなアスペリティと深い小さなアスペリティ領域おけるすべり量，すべり速度，すべり弱化関数，すべり速度スペクトルの相違。　（中央）アスペリティの概念配置図。

3.4　すべり速度に基づく震源特性化手法の整備

3.4.1　プログラム開発

疑似動力学的な QDYN と完全動力学的な SPECFEM3D の破壊シミュレーションのコンポーネントを開発した。この地震サイクル・シミュレーションは次のステップで進められる：(1)疑似動力学的なシミュレーション→(2)地震発生→(3)動力学的な破壊シミュレーション→(4)地震の破壊の終わり→次の地震サイクルのシミュレーション。

3.4.2　M8 クラスの動力学シミュレーション

今年度，マグニチュード 7～8.3 の地震を対象に完全動力学的シミュレーションを実施し，90 個の地震に対して最終すべり量と最大すべり速度に基づいたスケーリング則の検討を実施した。その結果を図 3.4-1 に示す。図 3.4－1(1)は最終すべり量から抽出されるアスペリティ領域のスケーリング則を示しており，経験的な関係式（Somerville et al.，1999）との良い一致を示す。しかし，アスペリティ数は経験的結果に比べて明らかに過小評価である。図 3.4－1(2)は最大のすべり速度に基づいたアスペリティのスケーリング則を示す。完全動力学的なモデリングに基づいた最終すべり量あるいは最大すべり速度から抽出されるアスペリティ面積は，これまでの運動的震源モデルの主要な震源パラメータの経験則と非常に良い一致を示す。ただし，最大アスペリティの面積が地震モーメントと比例していない。

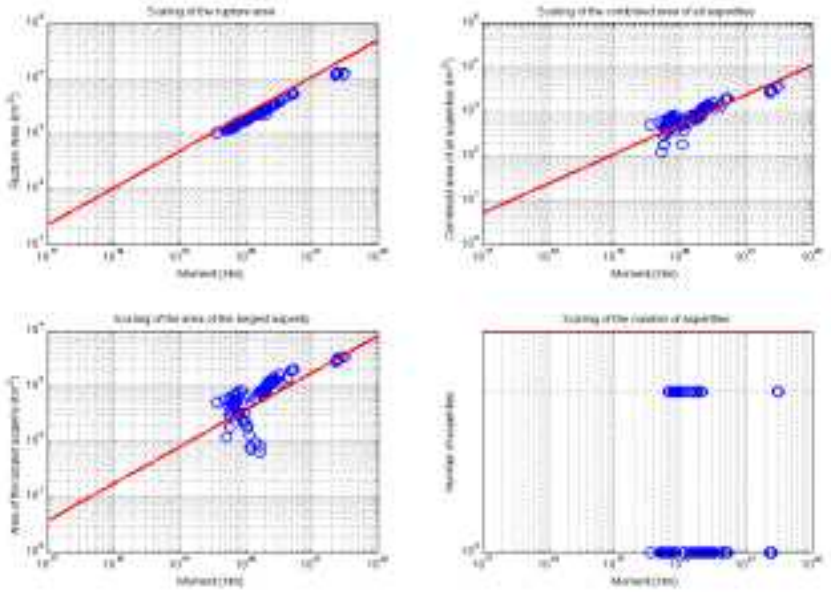

図 3.4－1(1)　最終すべり量で規定されるアスペリティのスケーリング則（完全動力学モデル）。

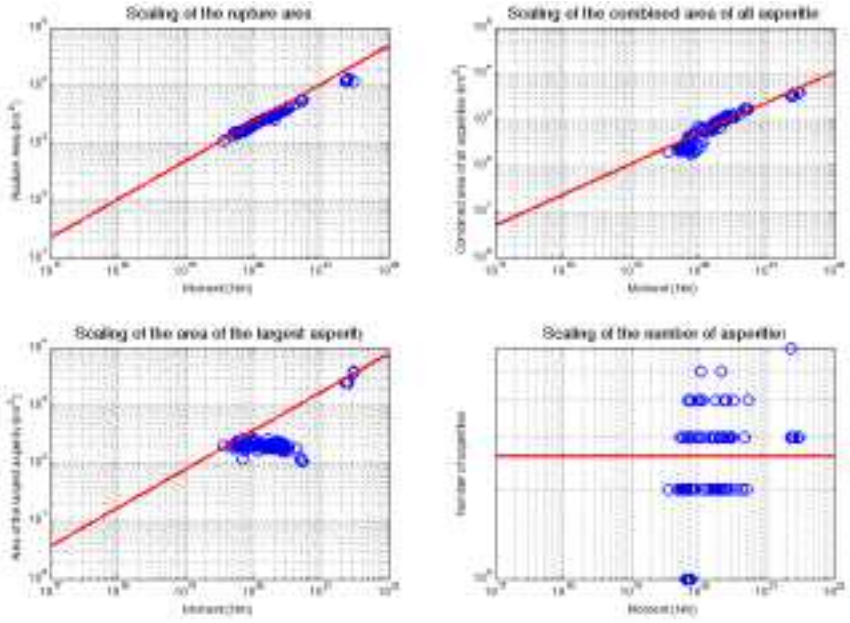

図 3.4－1(2)　最大すべり速度で規定されるアスペリティのスケーリング則（完全動力学モデル）。

3.4.3　空間相関分析

最終すべり量と最大すべり速度に対して，ノンゼロ・オフセット相関分析方法を利用し，両パラメータの空間相関分析を行った。ほとんどの相関係数は 0.8 より大きく，完全動力学的なモデリングによって得られた最終すべり量と最大すべり速度には非常に強い相関関係が認められた。

図 3.4－2 は，ずれの範囲内での相互相関関数の最大値および位置の関係を示す。最大値は，水平ゼロ線より約 5km 下に位置している。これは，最大すべり速度で規定されるアスペリティが最終すべり量で規定されるアスペリティから傾斜方向（深さ方向）に対して約 5km 下に位置していることを意味する。一方，水平方向では，両アスペリティの関係は，走行方向に対して±10～20ｋｍ以内に位置することを意味している。なお，破壊伝播方向は相関関数の最大値が現れる位置に影響を及ぼしており， 具体的には，破壊開始点が断層破壊域の右側にある場合（破壊伝播が右から左の場合），最大の相関関係は破壊開始点の左側に現れ，逆についても同様である。

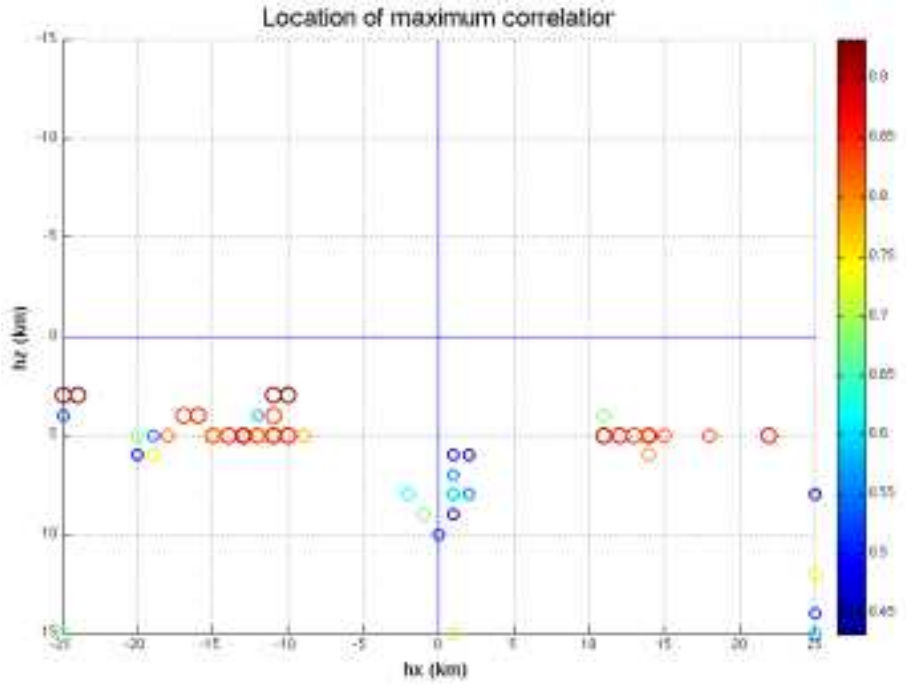

図 3.4－2　最終すべり量で規定されるアスペリティ位置に対する最大すべり速度によるアスペリティ位置の関係。○の色は最大相関係数の値を示す。

付　録

内容

Task 1. Multi-cycle Simulations for Non-Characteristic and Characteristic Events

The two tasks of this project require dynamic earthquake rupture simulations with non-uniform spatial distributions of initial stresses and friction parameters that are consistent with each other. It is common practice in computational earthquake dynamics to set initial conditions and fault strength independently. This approach disregards the spatial relations between stress and strength that arise throughout the earthquake cycle. For instance, aseismic slip during the inter-seismic period generates stress concentrations near the edges of strong asperities, and smaller magnitude earthquakes on weaker asperities leave stress concentrations around their rupture areas. Mechanical consistency between stress and strength can be introduced by simulating the whole earthquake cycle involving both seismic and aseismic deformation, i.e. short episodes of fast, dynamic slip separated by long periods of quasi-static, slow slip.

We are building a computational framework for large 3D earthquake cycle simulations. It combines two different programs: (1) QDYN, a quasi-dynamic solver based on the boundary element method (Luo and Ampuero, 2012), and (2) SPECFEM3D, a dynamic solver based on the spectral element method (Basini et al., 2012). Our team develops QDYN and the dynamic rupture components of SPECFEM3D. Both codes can simulate slip on non-planar faults. Only the second one can incorporate heterogeneous crustal velocity models. The workflow for earthquake cycle simulations is outlined as follows:

1. start quasi-dynamic simulation with QDYN
2. stop QDYN right before an earthquake starts (e.g. if slip velocity exceeds 1 cm/s)
3. convert the outputs of QDYN (stresses and friction variables) into inputs for SPECFEM3D
4. start dynamic rupture simulation with SPECFEM3D
5. stop SPECFEM3D at the end of the seismic rupture (e.g. when slip rate becomes too low)
6. convert the outputs of SPECFEM3D into inputs for QDYN
7. return to step 1 to simulate the next earthquake cycle

We compute a sequence of multiple earthquake cycles (typically more than 10) and discard the initial cycles from our analysis to avoid dependence on arbitrary initial conditions (the discarded cycles are called “warm-up cycles”). Implementation and verification of this framework is still underway. The results generated in year 1 of this project were based only on quasi-dynamic simulations (QDYN). In year 2 we developed the interface between QDYN and SPECFEM3D (step 3 in the outline above), which is required to include elastodynamics in the source scaling analysis. The criterion to switch between the two solvers is based on a threshold of slip velocity (~1 cm/s), as done in our previous 2D work (Kaneko et al, 2008).

We identified a bottleneck in the coupled QDYN-SPECFEM3D simulations. On faults governed by rate-and-state friction, earthquakes are preceded by a slow nucleation process, a long period in which slip accelerates gradually. Because the current dynamic solver uses constant time steps, simulating this long nucleation process requires a large number of time steps, hence expensive simulations. We developed an artificial rupture initiation procedure to guarantee that the rupture accelerates in a reasonable time without affecting the main properties of the dynamic rupture. The approach involves a "time-weakening" procedure, introduced for slip-weakening simulations by Andrews (1985), by which we prescribe a

space-time-dependent reduction of friction coefficient that forces initial rupture growth at controlled speed. The dynamic solver considers the smallest value between this prescribed friction coefficient and the one computed by rate-and-state, so that eventually, beyond a critical distance, the rupture becomes spontaneously controlled by rate-and-state friction. We set the prescribed initial rupture speed to 2 km/s over a maximum radius of 10 km (these settings remain to be optimized).

Task 2. Source Scaling and Correlations in Multi-cycle Simulations of Non-Characteristic and Characteristic Events

2.1 Introduction

The analysis of earthquake scaling relations conducted in Year 1 was based on *quasi*-dynamic simulations. Compared to fully dynamic simulations, these reproduce well the final slip and size of earthquakes, but not their rupture speed and peak slip velocity. This limitation may affect the definition of asperities and strong motion generating areas. To avoid this issue, we conducted dynamic simulations corresponding to 90 events with magnitudes between 7.0 and 8.3. Some examples are shown in Figure 1, and the full set is shown in Appendix C. Including elasto-dynamics did not increase the segmentation or complexity of the ruptures: most have a single, broad strong motion generation area.

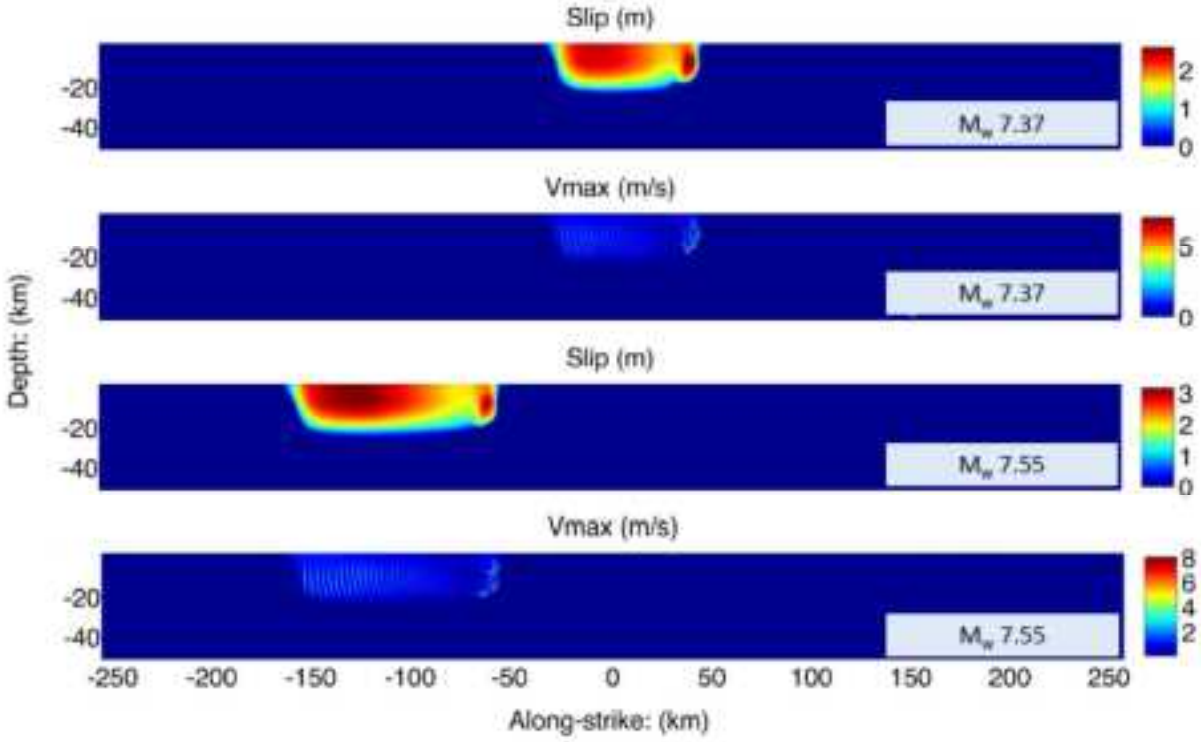

Figure 1: Spatial distribution of final slip and peak slip velocity of two simulated earthquakes (Mw 7.37 and 7.55, respectively) computed with the dynamic code SPECFEM3D based on initial conditions obtained with the quasi-dynamic code QDYN.

2.2 Scaling Relation Analysis

In previous work (Ampuero et al., 2013), we analyzed about 3000 events obtained from quasi-dynamic multi-cycle simulations for a wide range of magnitudes ($6.0 < M < 8.0$). We defined asperities based on final slip and computed the scaling relations of various source parameters as shown in Figure 2. They show good agreement with the empirical scaling relations proposed by Somerville et al. (1999).

This year we produced 90 events by full dynamic modeling and performed scaling analysis with both final slip and peak slip rate. The slip and maximum slip velocity distributions of the

set of 90 fully dynamic models are shown in Appendix C, in decreasing order of seismic moment. The File ID number in Appendix C indicates the order in which the events occurred.

Figures 3 and 4 show scaling relations with asperities defined based on final slip and peak slip rate, respectively. This set of 90 events contains 81 non-characteristic events in the magnitude range of 7.03 to 8.04, and 9 characteristic events in the magnitude range of 8.24 to 8.32, with a gap in seismic moment separating these two sets of events. The characteristic events were obtained in early cycles of the multi-cycle simulation (i.e., in the warm-up cycles), suggesting that they may have been perturbed by the initial conditions and may not be truly representative of characteristic events. The slip and maximum slip velocities of the asperities of the characteristic events have stress drops that are about twice those of the non-characteristic events.

The 90 dynamic models that we developed correspond to the 3D Random Dc Model (Model R) described in last year's report (Ampuero et al. 2013). As we noted in that report, the slip distributions generated by Model R are rather smooth, which may lead to unrealistic scaling of second order source properties such as the number of asperities.

The scaling relations for asperities based on final slip (Fig. 3) for the dynamic models show good agreement with the empirical relations (Somerville et al. 1999). There is some deviation from the empirical relation for the area of the largest asperity, and the number of asperities is clearly below the empirical line. This may indicate that a higher degree of heterogeneity of friction parameters is needed in the dynamic modeling.

The number of asperities derived based on peak slip rate (Fig. 4) is evenly distributed around the empirical prediction, but unlike the case for slip asperities, the area of the largest asperity does not scale with seismic moment. The scaling analysis of asperities based on both final slip and peak slip rate show that the kinematic source models produced by full dynamic modeling in this study show reasonably good agreement with the empirical relations for the major source parameters. We expect that we can improve the scaling relation for the number of asperities defined by final slip by considering alternative models of spatial heterogeneity of friction parameters.

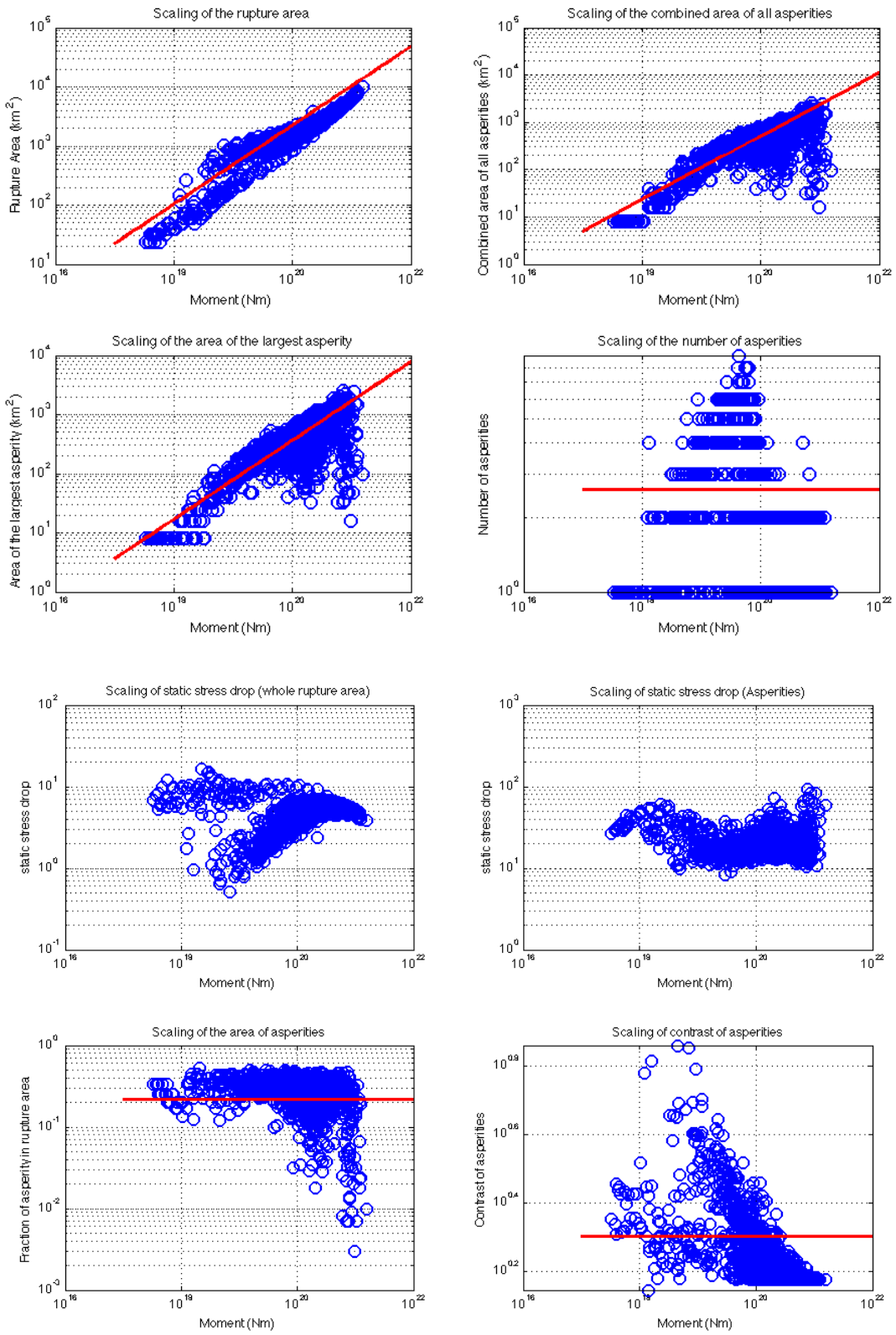

Figure 2. Scaling relations from slip distribution obtained by quasi-dynamic modeling. Aseismic slip is excluded in the analysis.

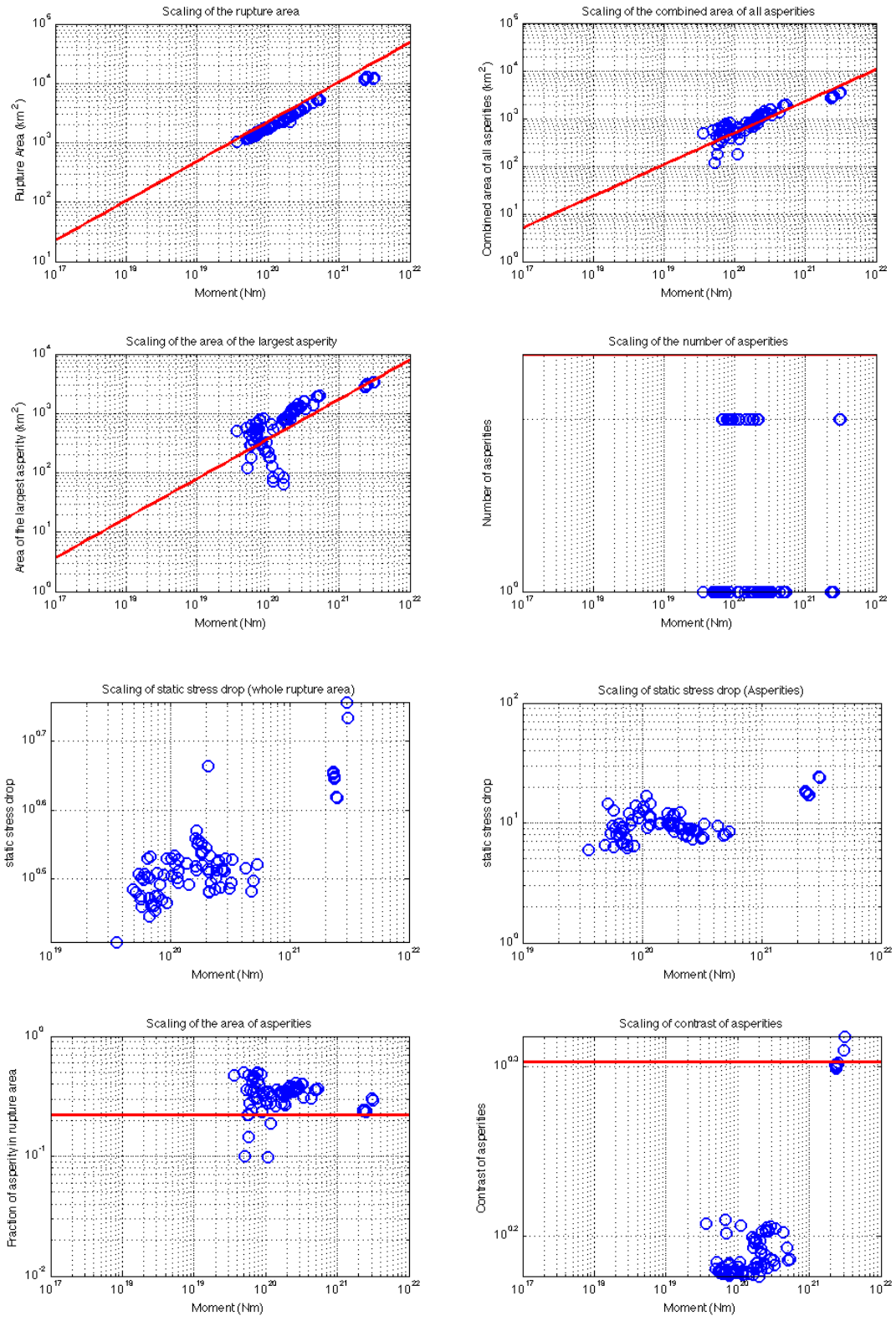

Figure 3. Scaling relations from slip distribution obtained by full dynamic modeling. The set of 9 large events (Mo > 1.0E21) on the right side were obtained in early cycles of the multi-cycle simulation (i.e., in the warm-up cycles), suggesting that they may have been perturbed by the initial conditions and may not be truly representative of characteristic events.

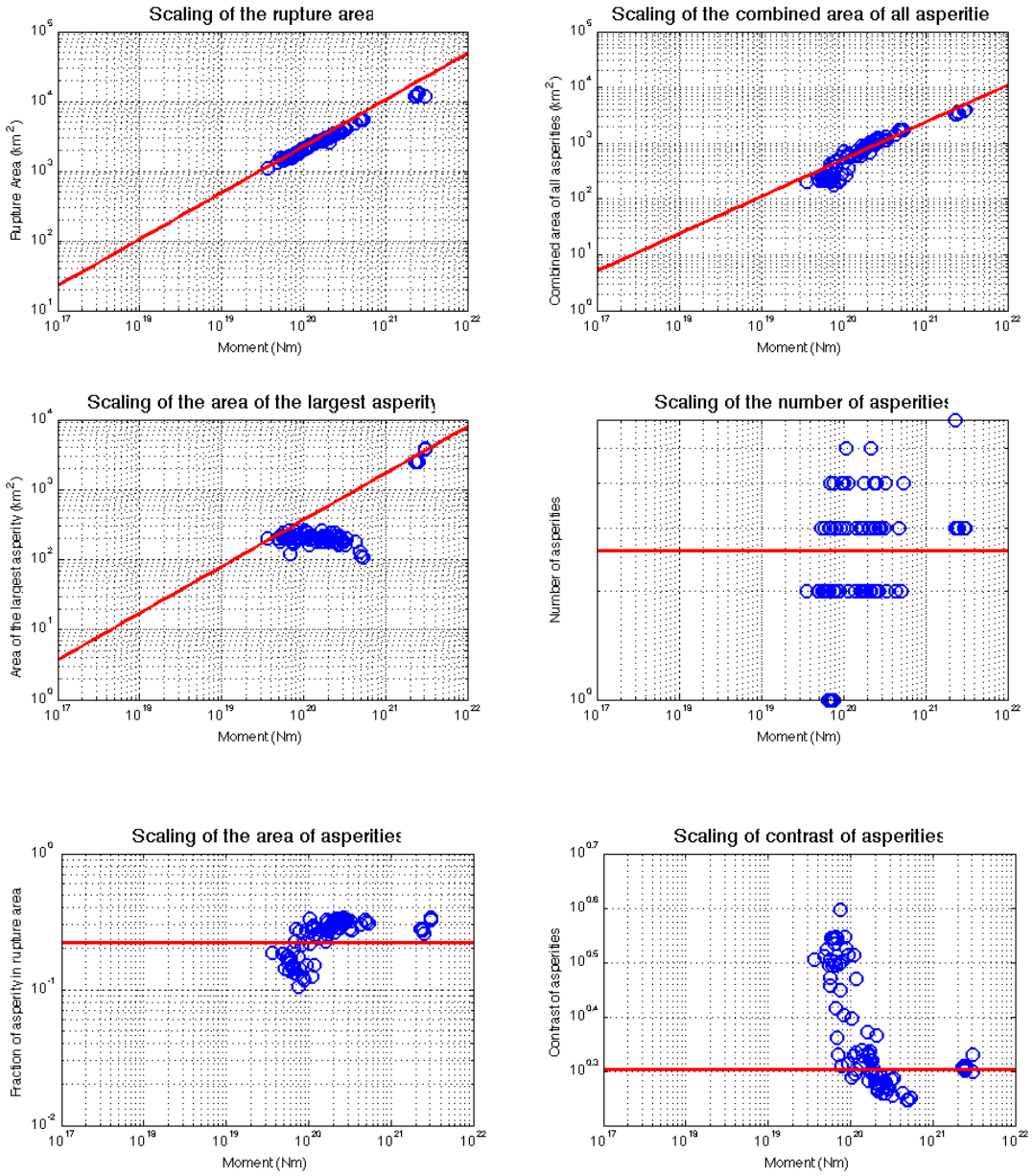

Figure 4. Scaling relations from peak slip rate distribution obtained by full dynamic modeling.

2.3 Spatial Correlation Analysis

We also performed spatial correlation analysis between slip and peak slip rate, based on the non-zero offset correlation analysis method (Song and Somerville 2010; Song et al. 2014). Figure 5 shows the histogram of maximum correlation coefficients for 90 events. The maximum values vary between 0.45 and 0.95, but most of the coefficients are larger than 0.8, which indicates very strong correlation between slip and peak slip rate obtained by full dynamic modeling in this study.

Figure 6 shows the amplitude and location on the fault plane of the maximum cross-correlations. In general, the maximum correlations are located about 5 km below the horizontal zero line. This means that on average the peak slip rate asperity is shifted about 5 km in the down-dip direction from the slip asperity. In the horizontal direction, they are shifted in either direction ($10 < hx < 20$ km or $-20 < hx < -10$ km), or located along the vertical zero line. Rupture propagation direction affects the horizontal shift of the location of the maximum correlation. Specifically, if the hypocenter is located on the right side of rupture area, the maximum correlation is located on the left side, and vice versa. Relatively small magnitude events ($Mw < 7.2$) in the database show correlation maximums in the middle with smaller values.

Figure 7 shows several examples of the spatial correlation structure. For full set of figures see Appendix D. The spatial correlation analysis shows that there is strong correlation between slip and peak slip rate parameters obtained by full dynamic modeling in this study. In addition, the peak slip rate asperity is located about 5 km downward from the slip asperity and shifted by about 10~20 km in the horizontal direction, depending on the rupture propagation direction.

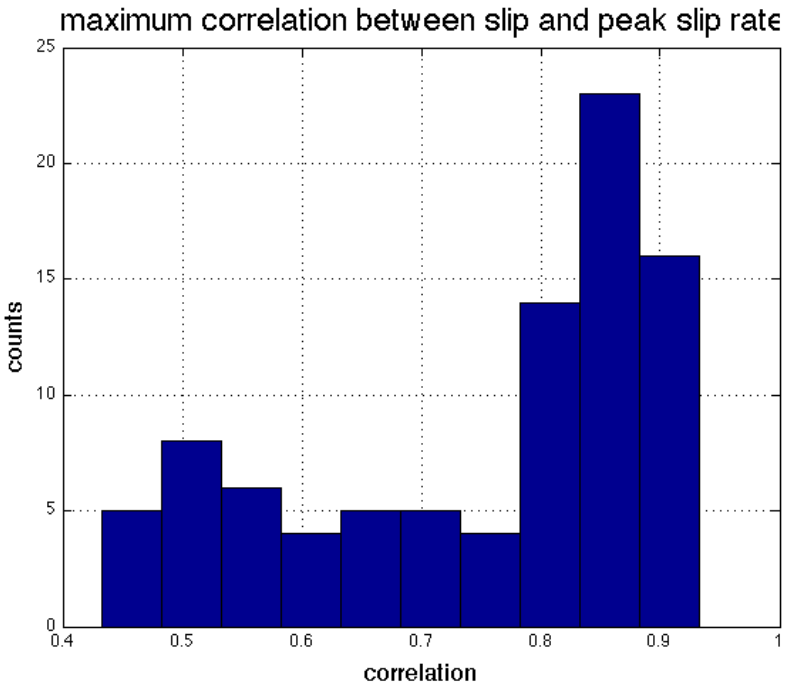

Figure 5. Histogram of maximum correlation coefficients

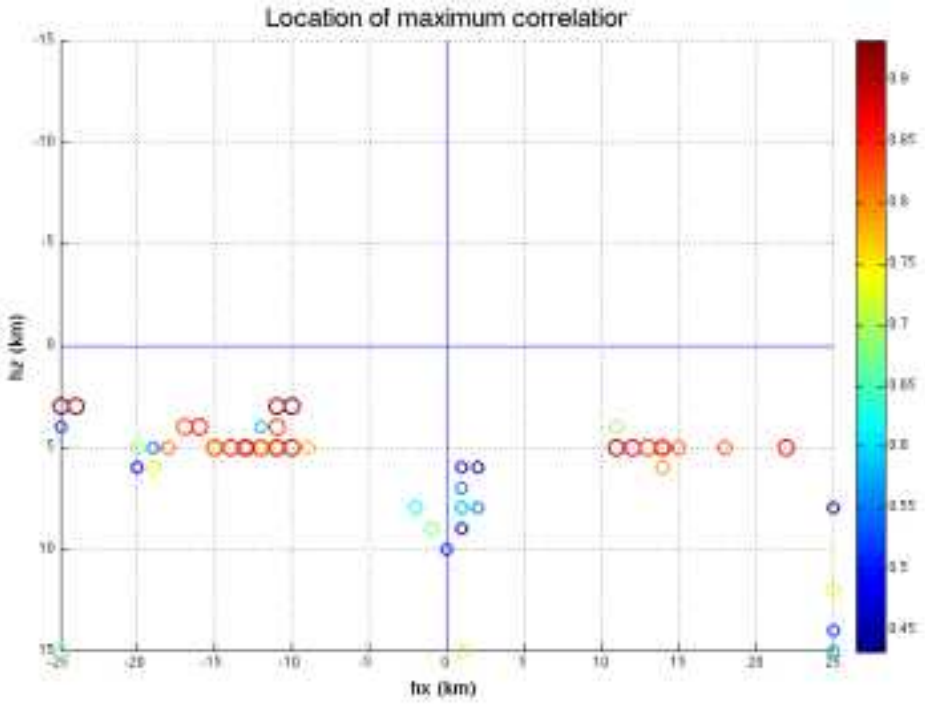

Figure 6. Locations of maximum correlations on the fault plane. The color of the circles indicates maximum correlation coefficient values.

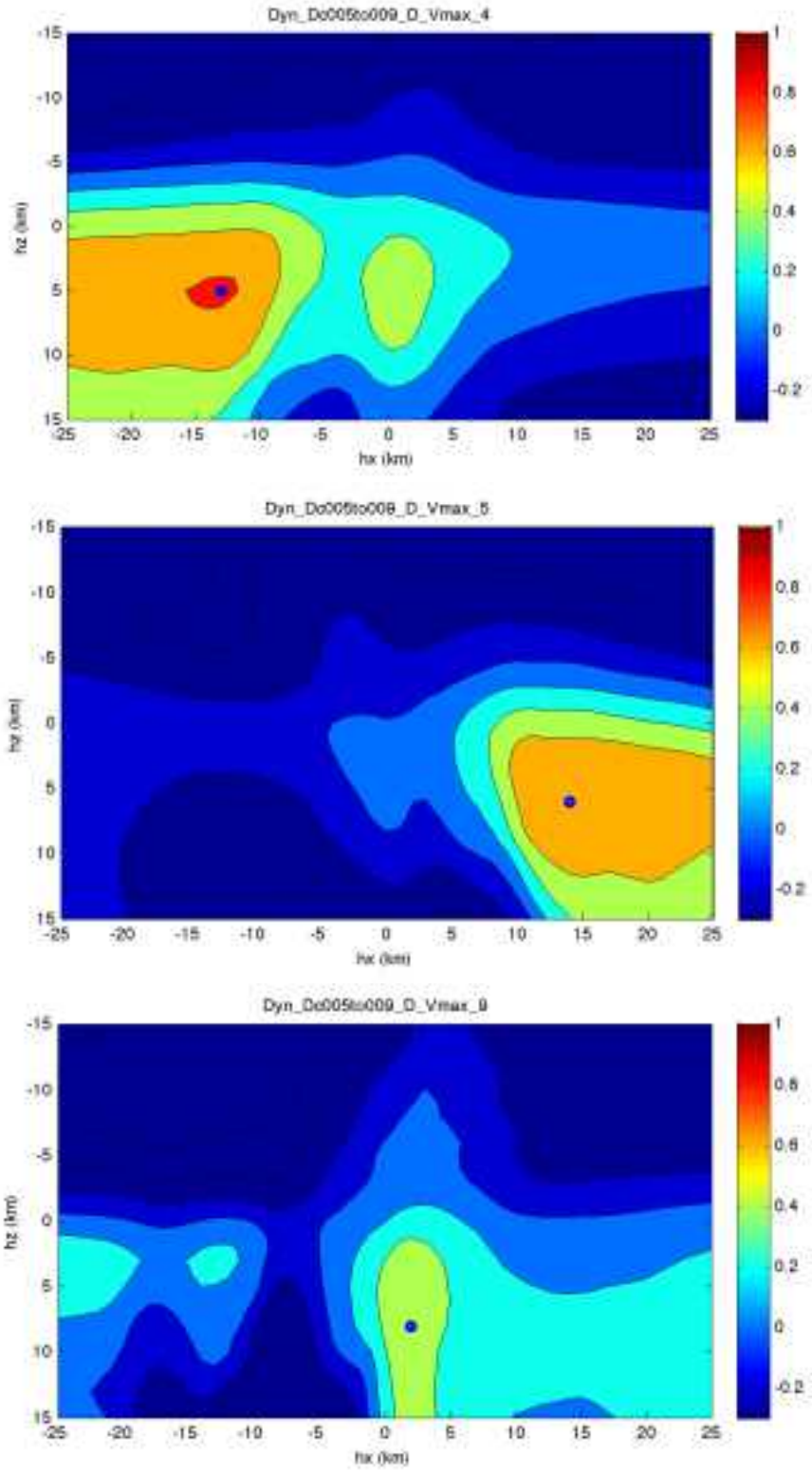

Figure 7. Three examples of cross-correlation between slip and peak slip rate: M7.55 (upper), M7.36 (middle), and M7.24(lower).

Task 3. Dynamic Simulation of M9 2011 Tohoku Earthquake

We completed a study of the 2011 Tohoku-Oki earthquake based on 2D dynamic rupture simulations under slip-weakening friction in which initial stress conditions and friction parameters are constrained by geophysical observations (Huang et al, 2013; Appendix A). The computations were based on our 2D spectral element code SEM2DPACK (Ampuero, 2012). In particular, we determined the fracture energy and along-dip extent and amount of stress deficit in the shallow region required to generate large slip at the trench while keeping the shallow high-frequency radiation low, and the ratio of deep to shallow critical slip distance necessary to explain the different frequency content of slip at different depths (Fig. 8). The model also generates a down-going secondary slip acceleration front when the rupture reaches the trench (Fig 8-a).

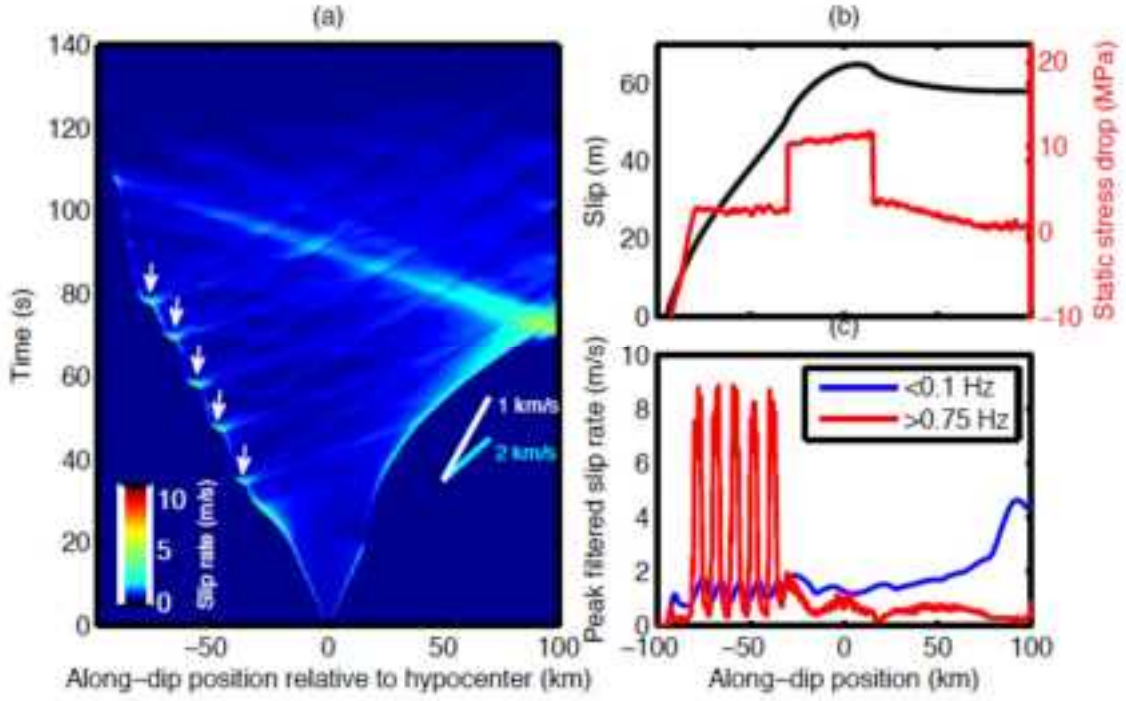

Figure 8. Spatial temporal distribution of slip rate (a), along-dip distribution of final slip and static stress drop (b) and along-dip distribution of low-pass filtered (<0.1 Hz) and high-pass filtered peak slip rates (>0.75 Hz) (c) in a 2D slip-weakening model of the Tohoku-Oki earthquake. In (a) the deeper regions are to the left and the white arrows indicate the regions of high-frequency radiation bursts. A down-going, secondary slip acceleration front emerges when the primary rupture front reaches the surface. From Huang et al (2013).

These 2D simulation results served as guidance to set up a 3D dynamic rupture simulation using the SPECFEM3D code (Galvez et al, 2014; Appendix B). In collaboration with the ETH Zurich group, we developed a minimalistic slip-weakening model that reproduces first order features of the earthquake. In particular, includes a non-planar megathrust fault surface and reproduces the reactivation of slip by a secondary front coming from the trench (Fig. 9) and the variability along depth of the frequency content of slip (Fig. 10).

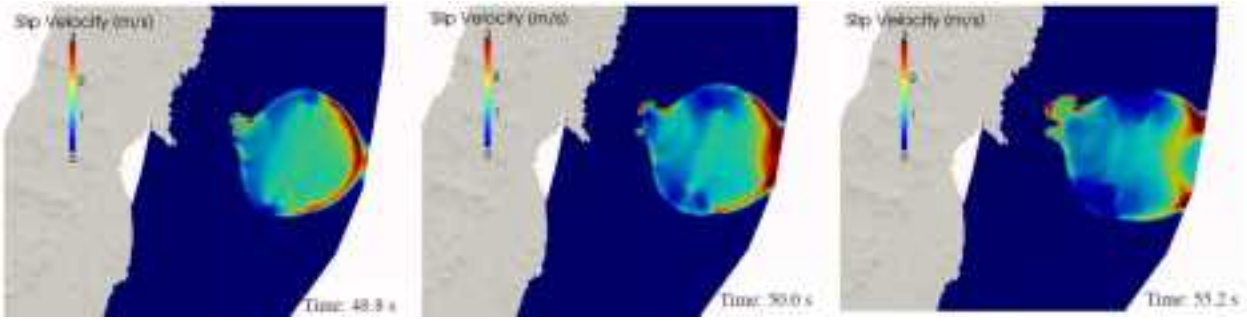

Figure 9. Spatial distribution of slip velocity at three different times, showing the emergence of a down-going secondary rupture front when the primary front reaches the trench. These are results from a 3D dynamic rupture model of the Tohoku-Oki earthquake (Galvez et al., 2014).

These 2D and 3D studies remain conceptual and suffer from the separate setting of initial stresses and frictional properties. Nevertheless, these results set the stage for our next step: to generate dynamic ruptures consistent with the quasi-dynamic megathrust earthquake cycle simulations computed in year 1. The 3D dynamic code is also ready to incorporate a 3D velocity model to compute synthetic ground motions that can be compared to observations.

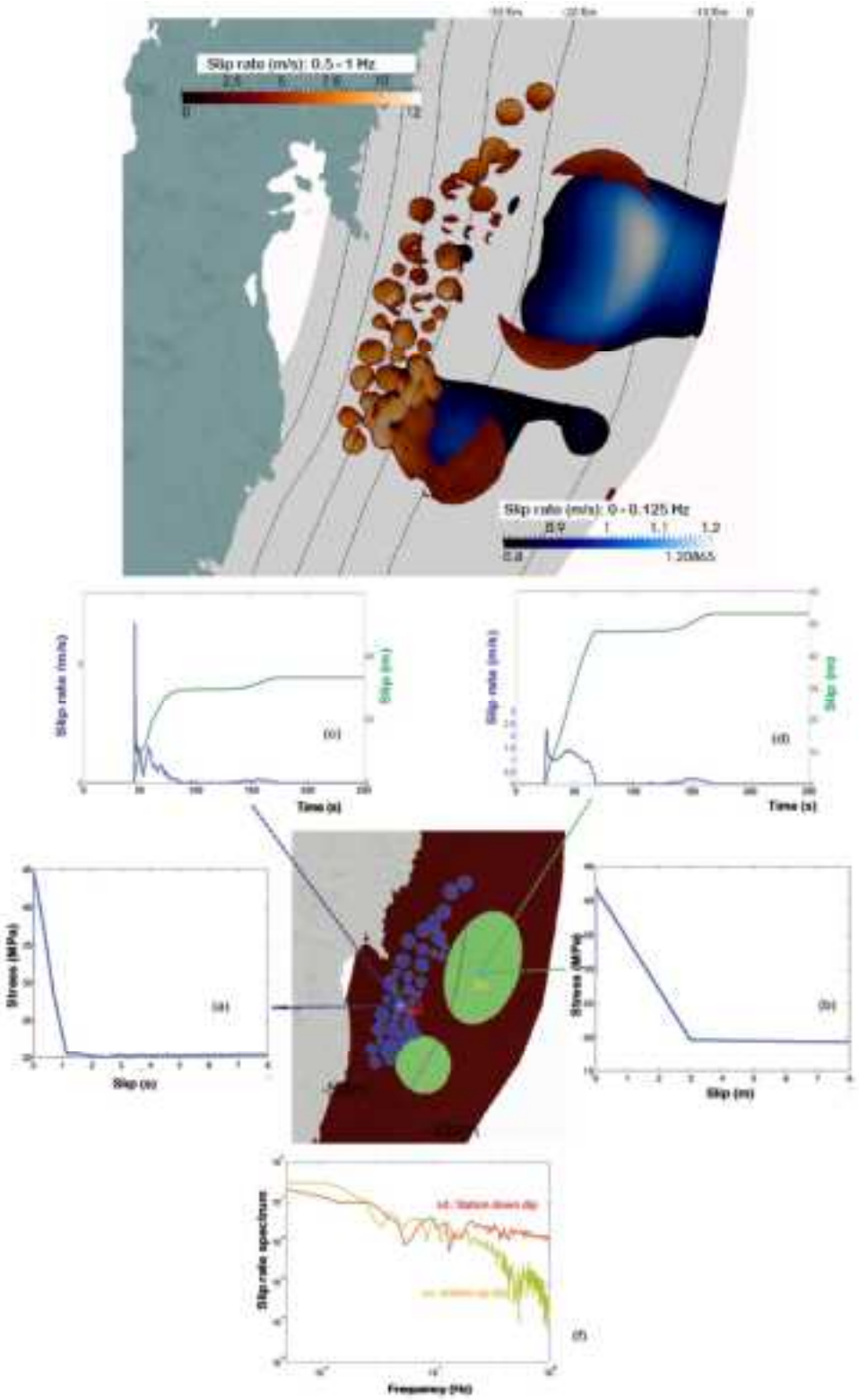

Figure 10. Top: Spatial distribution of peak slip rate in the 0-0.125 Hz and 0.5-1 Hz frequency bands in a 3D dynamic rupture model of the Tohoku earthquake (Galvez et al., 2014). Bottom: Slip, slip rate, slip-weakening curves and slip velocity spectra at two locations on the fault, a shallow point in the main asperity and a deep point in a secondary asperity. The middle plot shows the assumed geometry of the asperities.

References

Andrews, D. J. (1985), Dynamic plane-strain shear rupture with a slip-weakening friction law calculated by a boundary integral method, Bull. Seismo. Soc. Am., 75 (1), 1-21.

Ampuero, J. P. (2009), SEM2DPACK, A spectral element method tools for 2D wave propagation and earthquake source dynamics, User's Guide, version 2.3.6. Available online at http://www.sourceforge.net/projects/sem2d/.

Ampuero, J.-P., Y. Luo, S.G. Song, and P. Somerville (2013). Multi-cycle simulations of M8 and larger strike-slip earthquakes and Dynamic simulation of M9 2011 Tohoku earthquake**,** Project report to GeoResearch Institute

Dublanchet, P., P. Bernard, and P. Favreau (2013), Interactions and triggering in a 3-D rate-and-state asperity model, J. Geophys. Res. Solid Earth, 118, 2225–2245, doi:10.1002/jgrb.50187

Galvez, P., J.-P. Ampuero, L. A. Dalguer, S. N. Somala and T. F. Nisse-Meyer (2014), Dynamic earthquake rupture modeled with an unstructured 3D spectral element method applied to the 2011 M9 Tohoku earthquake, manuscript submitted to Geophys. J. Int.

Huang, Y., J.-P. Ampuero and H. Kanamori (2013), Slip-weakening models of the 2011 Tohoku-Oki earthquake and constraints on stress drop and fracture energy, Pure. Appl. Geophys., 1-14, doi:10.1007/s00024-013-0718-2

Kaneko, Y., N. Lapusta and J.-P. Ampuero (2008), Spectral-element modeling of spontaneous earthquake rupture on rate and state faults: Effect of velocity-strengthening friction at shallow depths, J. Geophys. Res., 113 (B9), B09317, doi:10.1029/2007JB005553.

Somerville, P.G., K. Irikura, R. Graves, S. Sawada, D. Wald, N. Abrahamson, Y. Iwasaki, T. Kagawa, N. Smith and A. Kowada (1999). Characterizing earthquake slip models for the prediction of strong ground motion. Seismological Research Letters, 70, 59-80.

Song, S., L.A. Dalguer, and P.M. Mai (2014). Pseudo-dynamic source modeling with 1-point and 2-point statistics of earthquake source parameters, *Geophys. J. Int.*, 196, 1,770-1,786.

Song, S., P. Somerville (2010). Physics-based earthquake source characterization and modeling with Geostatistics, *Bull. Seism. Soc. Am.* 100, 482-496.

Appendix A. Slip-Weakening Models of the 2011 Tohoku-Oki Earthquake and Constraints on Stress Drop and Fracture Energy (Huang et al., 2013).

Pure Appl. Geophys.

DOI 10.1007/s00024-013-0718-2

Pure and Applied Geophysics

Slip-Weakening Models of the 2011 Tohoku-Oki Earthquake and Constraints on Stress Drop and Fracture Energy

Yihe Huang,[1] Jean-Paul Ampuero,[1] and Hiroo Kanamori[1]

Abstract—We present 2D dynamic rupture models of the 2011 Tohoku-Oki earthquake based on linear slip-weakening friction. We use different types of available observations to constrain our model parameters. The distribution of stress drop is determined by the final slip distribution from slip inversions. As three groups of along-dip slip distribution are suggested by different slip inversions, we present three slip-weakening models. In each model, we assume uniform critical slip distance eastward from the hypocenter, but several asperities with smaller critical slip distance westward from the hypocenter. The values of critical slip distance are constrained by the ratio of deep to shallow high-frequency slip-rate power inferred from back projection source imaging. Our slip-weakening models are consistent with the final slip, slip rate, rupture velocity and high-frequency power ratio inferred for this earthquake. The average static stress drop calculated from the models is in the range of 4.5–7 MPa, though large spatial variations of static stress drop exist. To prevent high-frequency radiation in the region eastward from the hypocenter, the fracture energy needed there is in the order of 10 MJ/m^2, and the average up-dip rupture speed cannot exceed 2 km/s. The radiation efficiency calculated from our models is higher than that inferred from seismic data, suggesting the role of additional dissipation processes. We find that the structure of the subduction wedge contributes significantly to the up-dip rupture propagation and the resulting large slip at shallow depth.

Key words: Tohoku-Oki earthquake, dynamic rupture model, stress drop, fracture energy, energy partitioning, subduction wedge.

1. Introduction

Analyses of a wealth of data generated by the 2011 Tohoku-Oki earthquake have unveiled several unique features: (1) Rupture propagated through the shallow region (defined here as the region up-dip of the hypocenter), and it resulted in a large slip. This is supported by slip inversions (Simons 2011; Ide *et al.* 2011; Yue and Lay 2011; Yagi and Fukahata 2011; Lee *et al.* 2011; Wei *et al.* 2012; Iinuma *et al.* 2012) and static measurements by ocean-bottom pressure gauges and bathymetric data (Fujiwara *et al.* 2011; Ito *et al.* 2011; Sato *et al.* 2011; Kido *et al.* 2011; Kodaira *et al.* 2012). Several slip models are schematically shown in Fig. 1a. (2) High-frequency ($\sim$1 Hz) energy radiation was mostly concentrated down-dip from the hypocenter. Under the assumption that the advancing front of high-frequency radiation coincides with the rupture front, the down-dip rupture velocity was estimated to be as low as $\sim$1 km/s (Meng *et al.* 2011; Kiser and Ishii 2012).

The extensive observations available for this event warrant efforts to understand the basic physics responsible for these unique observations. To this end, we carry out dynamic rupture simulations for this earthquake. Previous studies suggest that heterogeneities of fault friction or stress are needed to explain the spatial variations of rupture behavior during this earthquake (Kato and Yoshida 2011; Aochi and Ide 2011; Duan 2012; Goto *et al.* 2012; Huang *et al.* 2012) as well as the complex temporal characteristics of historical earthquakes (Igarashi *et al.* 2003; Tajima *et al.* 2013). Furthermore, a key question is what causes the rupture to propagate through the shallow region. Numerical simulations suggest that waves reflected inside the subduction wedge induce large transient stress changes on the fault, which promote the up-dip rupture propagation (Huang *et al.* 2012) despite the stable, velocity-strengthening frictional behavior expected in fault zones at shallow depth (Kozdon and Dunham 2013). Other models invoke fault weakening mechanisms in the shallow region, such as shear heating of pore fluids, to promote unstable slip (Yoshida and Kato 2011; Noda and Lapusta 2013).

[1] Division of Geological and Planetary Sciences, California Institute of Technology, 1200 E. California Blvd. MS 252-21, Pasadena, CA 91125, USA. E-mail: yihe@gps.caltech.edu

Birkhäuser

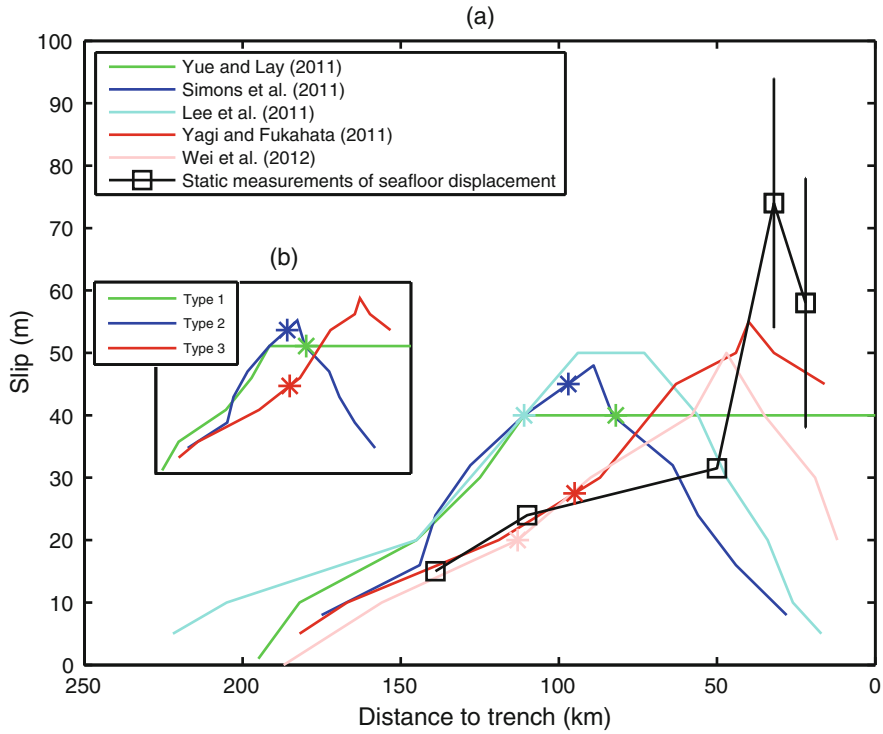

Figure 1
a The along-dip slip distributions across the hypocenter inferred from five slip inversions. The hypocenter used in each inversion is shown as a *star*. The displacement of sea floor is shown in *black*, including five measurements at or near the latitude of the hypocenter from Sato *et al.* (2011), Ito *et al.* (2011) and Kido *et al.* (2011). **b** The three types of along-dip slip distributions

In this paper, we attempt to find numerical models that can provide some useful constraints on the overall physical properties of the earthquake, such as stress drop and fracture energy. To keep the number of assumptions as few as possible, we use a simple elastic model with slip-weakening friction. We will focus on the along-dip rupture process near the latitude of the hypocenter and will try to explain the various observations in the shallow and deep regions, such as variations of slip, radiation frequency spectrum and rupture velocity.

2. *Model Setup and Observational Constraints on Model Parameters*

We consider a shallow-dipping fault with a dip angle of 14° embedded in a 2D elastic half space. The fault is 200 km long in the along-dip direction. The hypocenter is located in the middle. Material properties such as density ρ (3,000 kg/m^3), Poisson's ratio ν (0.25) and shear modulus μ (30 GPa) are uniform throughout the medium. We solve the problem using a 2D spectral element code (Ampuero 2009) and the unstructured mesh shown in Fig. 2a (Huang *et al.* 2012). We prescribe an artificial nucleation procedure in the hypocentral region. The friction coefficient is forced to drop over a certain time scale from static to dynamic levels inside a region with time-dependent size (Andrews 1985). After reaching a critical nucleation size which is much shorter than the total rupture length, the rupture propagates spontaneously to both up-dip and down-dip directions. The linear slip-weakening friction law governs the remaining part of the fault, and the model contains five free parameters: initial shear stress τ_0, normal stress σ_n, static friction coefficient μ_s, dynamic friction coefficient μ_d and critical slip distance D_c (Fig. 2b). We constrain these model parameters using several observations, as described next.

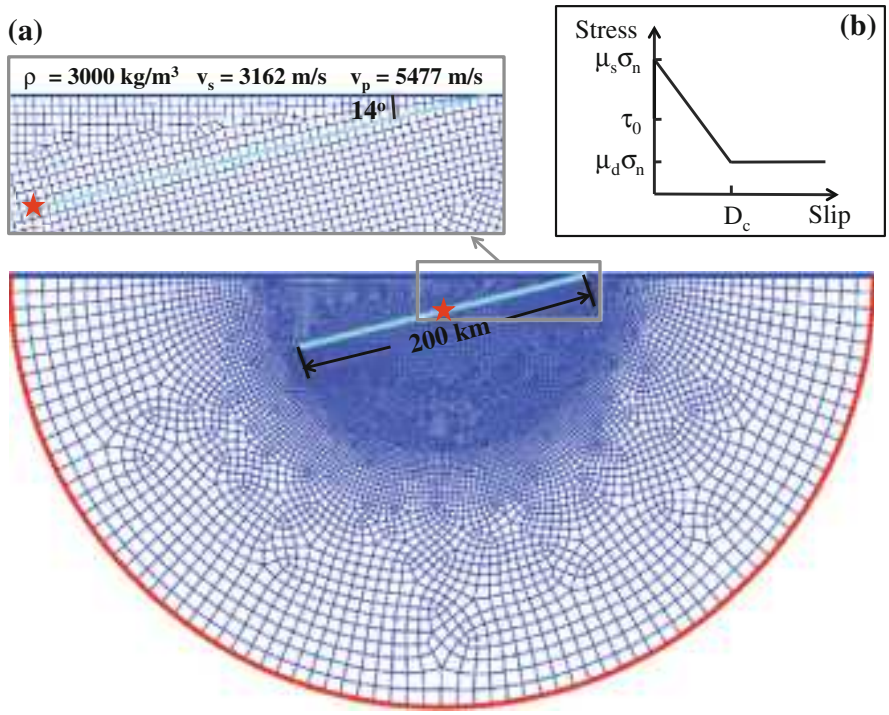

Figure 2

a The unstructured mesh with a free boundary on the top (*blue line*) and an absorbing boundary in a semicircular (*red line*). The hypocenter is in the middle of the 200-km-long fault (*turquoise line*). The zoom-in picture shows the mesh around the fault and the dip angle of the fault. The density, S velocity and P velocity are indicated on the top of the zoom-in picture. **b** Linear slip-weakening law. Stress increases from initial shear stress τ_0 to static strength $\mu_s\sigma_n$ first, and then decreases linearly to dynamic strength $\mu_d\sigma_n$ when slip reaches the critical slip distance D_c. The shear stress then remains at the dynamic strength level

2.1. *Normal Stress σ_n and Friction Coefficients μ_s and μ_d*

We adopt a normal stress profile from the Nankai region, which has an effective normal stress of about 10 MPa up to a horizontal distance of 20 km from the trench (Tobin and Saffer 2009). Further away from the trench, the normal stress is increased to 100 MPa by a vertical gradient of 6 MPa/km, and kept constant in deep regions (Fig. 3). We initially assume a constant static friction coefficient $\mu_s = 0.6$ and dynamic friction coefficient $\mu_d = 0.2$. As we will illustrate in Sect. 3, the friction coefficients have to be modified in some regions to reproduce the observations.

2.2. *Stress Drop $\tau_0 - \mu_d\sigma_n$*

The distributions of stress drop $\tau_0 - \mu_d\sigma_n$ are inferred from the coseismic final slip distributions shown in Fig. 1a. The static stress drop that results from our calculations is different from $\tau_0 - \mu_d\sigma_n$ due to overshoot, and we will discuss the distribution of the static stress drop later in Sect. 4. For each slip inversion, we measured roughly the slip at several locations in the along-dip direction across the hypocenter. The figure aims to show the overall differences of the inferred slip profiles, rather than reproduce the details of each model. We find that, although in all models large slip is concentrated in the shallow region, the slip profiles are highly variable up-dip from the hypocenters, which are shown by stars. Overall, they fall into three types (Fig. 1b): (1) almost constant slip in the shallow region (green line in Fig. 1a), (2) peak slip near the hypocenter (blue and turquoise lines in Fig. 1a) and (3) peak slip between the hypocenter and the trench (red and pink lines in Fig. 1a). Static measurements of seafloor displacements (black line in Fig. 1a) seem to favor

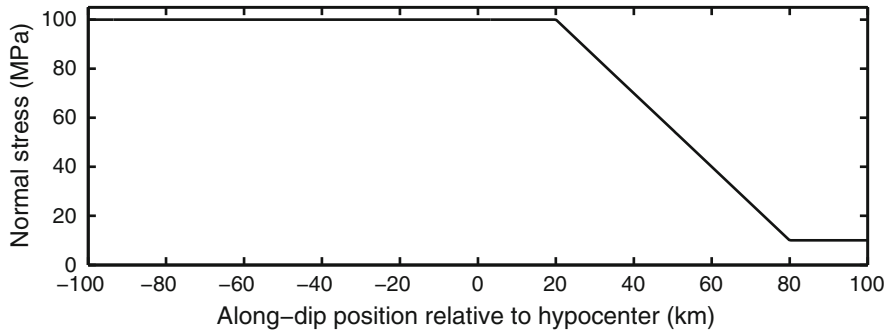

Figure 3
The along-dip distribution of normal stress in all three models

large slip near the trench, but have large uncertainties (Ito *et al*. 2011) and possibly involve post-seismic deformations. Hence, we consider the three possible slip profiles in our numerical models.

2.3. Critical Slip Distance D_c

The results from back-projection source imaging constrain the high-frequency slip-rate power in the deep region. Huang *et al.* (2012) found that the ratio between deep and shallow high-frequency slip-rate power is at least 10. In order to generate high-frequency radiation in dynamic rupture models, heterogeneities of either fracture energy or initial stress are needed (Madariaga 1983). However, only stress concentrations such as the residual stresses at the edge of a previous slip event can be as efficient as an abrupt change of fracture energy. For computational convenience, we choose to set heterogeneities of fracture energy by varying the value of D_c in our slip-weakening model. To reproduce the spatial contrast of high-frequency radiation, we set a uniform D_c in the shallow region, but several small asperities with much smaller D_c in the deep region. In reality the deep region may have variations of both fault strength and stress, which in combination can give rise to strong high-frequency radiation. A deep region with small asperities also agrees with the fact that earthquakes have repeatedly occurred there in the past (e.g., Igarashi *et al*. 2003; Tajima *et al.* 2013). The spacing of small asperities in our model is conceptual rather than corresponding directly to earthquakes of specific magnitude. However, given the same stress conditions, the spacing needs to be large enough to prevent the down-dip rupture from propagating faster than 1 km/s.

It is noteworthy that in such an asperity model the deep/shallow D_c ratio is determined by the high-frequency slip-rate power ratio, as illustrated in Fig. 4. The amplitude spectrum of slip rate at a certain location on the fault tends to the final slip D at very low frequency. Figure 4 shows two amplitude spectra, one for a deep region with final slip D^d and the other for a shallow region with final slip D^s. Each amplitude spectrum has two corner frequencies: the lower one is related to the time required for slip to reach its final value, or rise time t_{ris}; and the higher one is related to the time required for slip to reach D_c, or process zone time t_{pz} (see also Fig. 5c in Kaneko *et al*. 2008). The latter can be approximated as $t_{pz} \sim \frac{\mu D_c}{(1-\nu)\Delta\tau_s A_{II}(v_R) v_R}$, where ν is Poisson's ratio, v_R is rupture velocity, $\Delta\tau_s$ is the strength drop, i.e., the difference between static and dynamic strength $(\mu_s - \mu_d)\sigma_n$, and A_{II} is a function of rupture speed in mode II given by equation 5.3.11 in Freund, L. B., Dynamic fracture mechanics (Cambridge Univ. Press, Cambridge (1990). As D^d, D^s, t^d_{ris} and t^s_{ris} can be inferred from the slip inversions, and the high-frequency slip-rate power ratio from the back projection, the ratio t^d_{pz}/t^s_{pz} can be determined, so is the deep/shallow D_c ratio D^d_c/D^s_c. Besides, the back projection is carried out in a certain frequency band (e.g., 0.5–1 Hz in Meng *et al*. 2011). The center of the back-projection frequency band, f_{bp}, should be larger than the second corner frequency in the shallow region, $f_{bp} > \frac{1}{t^s_{pz}}$. This provides a lower bound for D^s_c. We show a detailed mathematical derivation of deep/

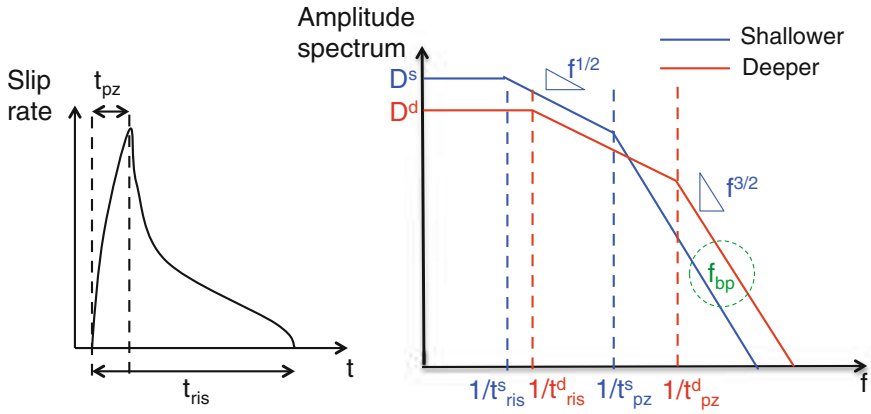

Figure 4
Slip rate function with two time scales: rise time t_{ris} and process zone time t_{pz} (*left*). Amplitude spectrum of the slip rate functions for shallow and deep regions, respectively, denoted by subscript 's' and 'd' (*right*). The frequency of back projection f_{bp} is indicated by a *dot circle*

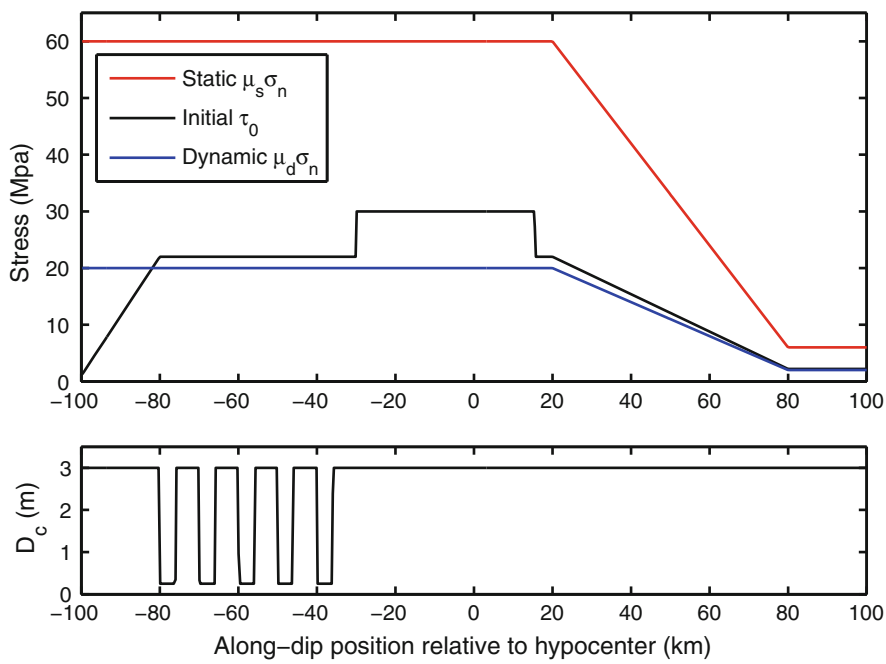

Figure 5
The along-dip distributions of initial shear stress, static strength, dynamic strength (*top*) and critical slip distance (*bottom*) in the first model

shallow D_c ratio in terms of high-frequency slip-rate power ratio in the "Appendix".

3. Results from the Three Models

In this section, we will present dynamic rupture simulations for the three different models that reproduce the three types of along-dip slip profiles (Fig. 1b).

3.1. First Model (Constant Slip in Shallow Region)

To reproduce the first slip profile that has a constant slip in the shallow region, we keep the static and dynamic friction coefficients constant. The

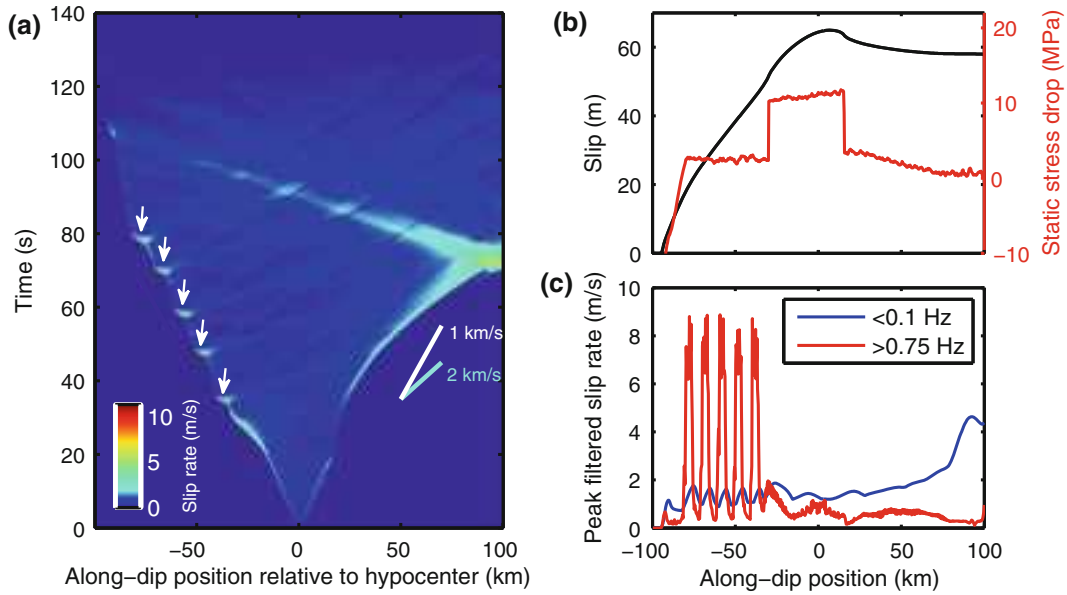

Figure 6
The spatial temporal distribution of slip rate (*left*), the along-dip distribution of final slip and static stress drop (*top right*), and the along-dip distribution of low-pass filtered (<0.1 Hz) and high-pass filtered peak slip rates (>0.75 Hz) (*bottom right*) in the first model. The *white arrows* in the left figure denote the regions of high-frequency bursts

distributions of model parameters are shown in Fig. 5. Rupture is forced to propagate bilaterally at 800 m/s inside the nucleation region (Fig. 6a). After about 20 s, the down-dip rupture starts to propagate spontaneously and accelerates until it reaches the low stress-drop region at 30 km from the hypocenter. It then propagates at a speed of about 1 km/s and generates high-frequency bursts when it propagates through the small asperities (Fig. 5). Due to the uniform frictional properties assumed eastward of the hypocenter, the up-dip rupture propagates smoothly. It reaches an average speed of about 2 km/s and produces an almost constant slip in the shallow region (Fig. 6b). To quantify the distribution of high-frequency radiation we compute at each fault location the peak value of the slip rate high-passed filtered above 0.75 Hz. The resulting high-frequency peak slip rate is much larger in the deep region than in the shallow region (Fig. 6c). In contrast, the peak values of the slip rate low-passed filtered below 0.1 Hz are more uniform. Their values are in the range of 1–2 m/s, consistent with the average slip rate from slip inversions (Lee *et al.* 2011; Wei *et al.* 2012), except in the region near the trench. To compare with the high-frequency power ratio in the back projection, we compute the power of the high-passed slip rate over a 10 s sliding window and apply a spatial Gaussian smoothing of half width 50 km, a conservative estimate of the spatial smearing in the back-projection source imaging. This leads to a deep/shallow power ratio of about 10.

3.2. *Second Model (Peak Slip in Hypocentral Region)*

In the second model, peak slip near the hypocenter indicates a larger stress drop there (Fig. 7), which can promote rupture acceleration. Thus, we reduce the initial shear stress in the deep region to keep the rupture velocity as low as 1 km/s. We found that the steep decrease of slip from the hypocenter to the trench (Fig. 1b) can only be achieved by a negative stress drop. This suggests that either the initial shear stress is lower or the dynamic friction coefficient is higher than in our first model. However, since the normal stress near the trench is very low and so is the dynamic strength, it is not possible to reduce the initial shear stress enough while keeping its sign consistent with thrust faulting. We, hence, increase the dynamic friction coefficient linearly in the

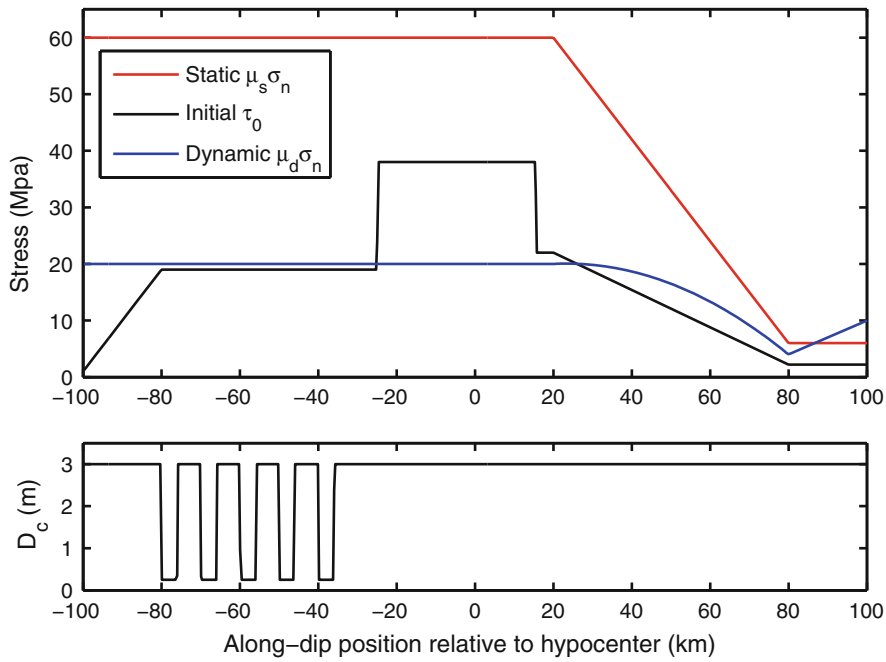

Figure 7
The along-dip distributions of initial shear stress, static strength, dynamic strength (*top*) and critical slip distance (*bottom*) in the second model

shallow region, which produces a curved profile of dynamic strength (Fig. 7). The resulting dynamic rupture (Fig. 8a) is similar to our first rupture model, except for the shorter nucleation stage. The final slip distribution (Fig. 8b) and high-frequency power ratio (Fig. 8c) are also consistent with the observations.

3.3. Third Model (Peak Slip in Shallow Region)

The third model features peak slip between the hypocenter and the trench, as suggested by many slip inversion studies. In this model, the largest stress drop is located up-dip from the hypocenter and decreases in both directions along-dip. Because of the lower stress drop in the nucleation region compared to our previous two models, the static friction coefficient and D_c are reduced there to achieve rupture nucleation (Fig. 9). Successful down-dip rupture requires the region with reduced D_c, which is as low as within the small asperities, to extend 40 km down-dip from the hypocenter. The small asperity located from 36 to 40 km down-dip from the hypocenter in the previous two models is, hence, not present in the third model. To avoid significant slowing down of the down-dip rupture, the value of D_c in between the small asperities is smaller than in the previous two cases. As large stress drop promotes high-frequency radiation, we also increase D_c in the shallow region. The details of the resulting rupture are shown in Fig. 10a. The rupture reaches a down-dip speed of about 1 km/s and an up-dip speed of about 2 km/s. Again, the down-dip rupture generates much stronger high-frequency radiation than the up-dip rupture (Fig. 10c).

4. Constraints on Static Stress Drop, Fracture Energy and Energy Partitioning

4.1. Static Stress Drop

The average static stress drop inferred from different slip inversions of the Tohoku-Oki earthquake is 4.8 MPa (Koketsu *et al.* 2011), 6 MPa (Yagi and Fukahata 2011) and 7 MPa (Lee *et al.* 2011), respectively. We compare these values to $\Delta\tau_E = \frac{\int \Delta\tau D ds}{\int D ds}$, the slip-weighted average of the static stress drop distributions obtained in our rupture models. This averaging procedure is appropriate for energy estimates (Noda and Lapusta 2012). The

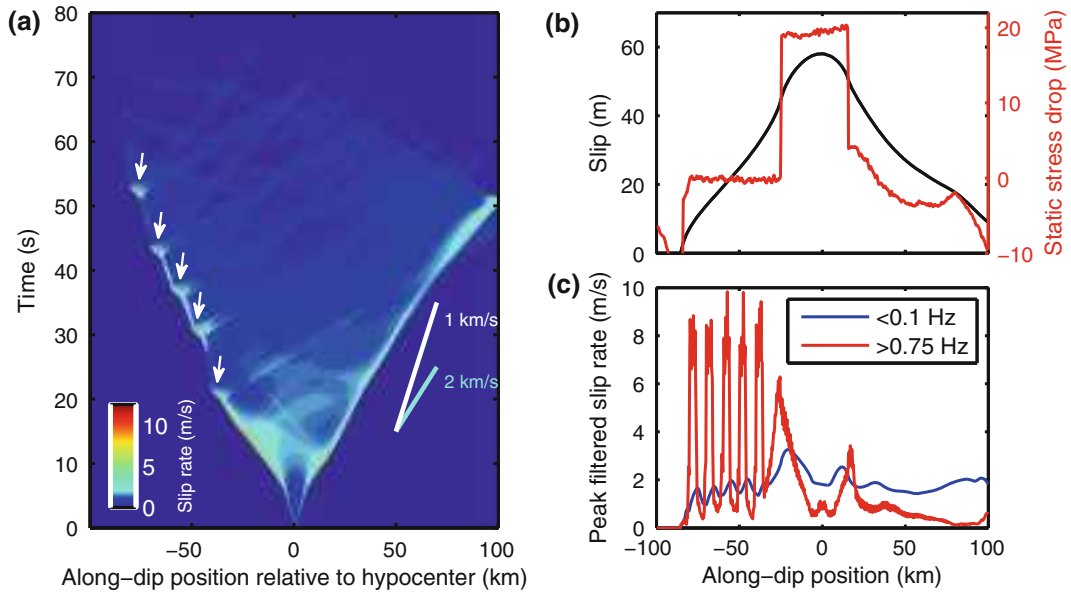

Figure 8
The spatial temporal distribution of slip rate (*left*), the along-dip distribution of final slip and static stress drop (*top right*), and the along-dip distribution of low-pass filtered (<0.1 Hz) and high-pass filtered peak slip rates (>0.75 Hz) (*bottom right*) in the second model. The white arrows in the left figure denote the regions of high-frequency bursts

values of $\Delta\tau_E$ thus calculated for the three models are 4.5, 7 and 4.6 MPa, similar to the average static stress drop inferred from slip inversions. Note that the static stress drop can vary in space by almost two orders of magnitude, e.g., from 12 MPa in the peak-slip region to 0.2 MPa near trench in the first model (Fig. 6b). In the other two models the stress drop near the trench is negative but the overall stress drop is still positive (Figs. 8b and 10b). The first and second models provide the two end members of the distributions of static stress drop in the Tohoku-Oki earthquake. In the first model, the static stress drop in the shallow region is rather small and almost zero near the trench. The large stress drop around the hypocenter pushed the whole shallow region eastwards and the resulting slip is large but almost constant. This behavior is somewhat similar to block sliding. In contrast, the second model requires a large negative stress drop in the shallow region. The large stress drop around the hypocenter still pushes the shallow region eastwards, but the final slip decreases due to the resistance caused by the larger dynamic friction prescribed there, resulting in the negative stress drop. The third model is similar except that the region with large stress drop is located eastward from the hypocenter.

The negative stress drops in the second and third models can result from velocity-strengthening materials in nature. The shallow velocity-strengthening region is usually considered as the upper limit of the seismogenic zone, defined as the zone where earthquakes can nucleate. Our numerical models show that ruptures can break through this region and result in a large slip there. Our models constrained by observed slip profiles (Fig. 1) show that the velocity-strengthening region needs to reach at least 40 km down-dip from the trench, or even more than 70 km as suggested by the slip profiles from Lee *et al.* (2011) and Simons (2011). Usually the upper limit of the seismogenic zone on subduction megathrusts is at a depth of 5–15 km (Hyndman *et al.* 1997), or at an along-dip distance of 20–60 km given the subduction geometry in our models. However, the different in situ pressures, temperatures and minerals make it hard to determine the upper limit of the seismogenic zone in specific subduction zones. Resolving this question in the Tohoku region requires a reliable identification of the interplate seismicity and determination of the coseismic slip profile of the Tohoku-Oki earthquake at shallow depth. While multiple observations point to large slip close to trench,

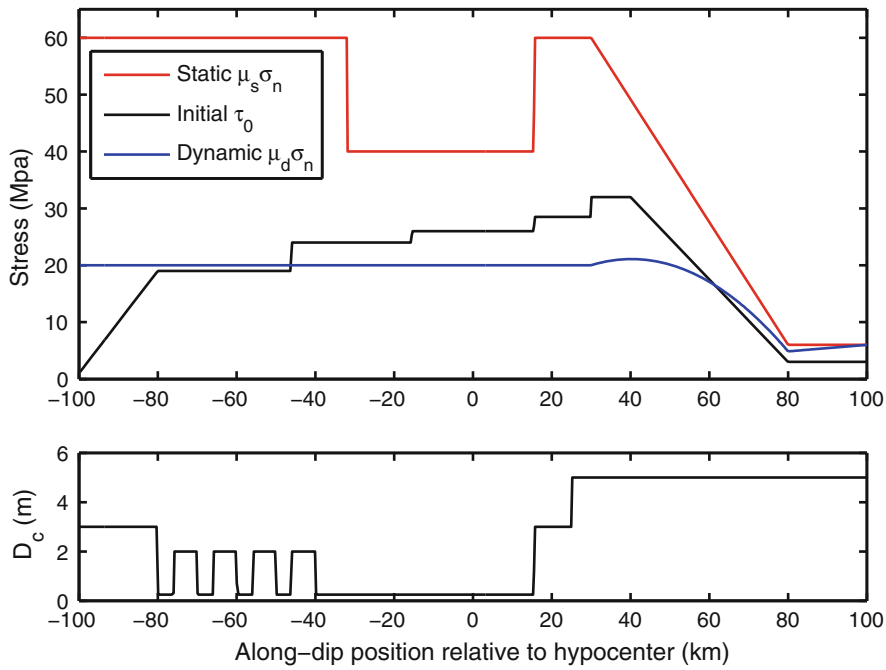

Figure 9
The along-dip distributions of initial shear stress, static strength, dynamic strength (*top*) and critical slip distance (*bottom*) in the third model

whether they involve significant postseismic deformation is still an open question. Studies of early postseismic deformation are necessary to understand this better.

4.2. Fracture Energy

A significant product of our models is the constraint on fracture energy or D_c in the shallow region. As discussed in Sect. 2, the back-projection frequency f_{bp} should be larger than the second corner frequency in the shallow region, which suggests:

$$D_c^s > \frac{(1-\nu)\Delta\tau_s^s v_R^s A(\nu_R)}{\mu f_{bp}}. \qquad (1)$$

For example, when $f_{bp} = 0.75\,\mathrm{Hz}$, $\Delta\tau_s^s = 22.5\,\mathrm{MPa}$ and $v_R^s = 2\,\mathrm{km/s}$, we find $D_c^s > 1.9\,\mathrm{m}$ in the first model. Thus, for a given D_c^d, we can find a D_c^s that satisfies the deep/shallow high-frequency power ratio ("Appendix") and the lower bound given by f_{bp} (Eq. 1). Figure 11 summarizes the deep/shallow high-frequency slip-rate power ratio (>0.75 Hz) obtained in the first model for a range of values of fracture energy and D_c^s in a 80 km wide region, 20 km eastward from the hypocenter and beyond. This result shows that if $D_c^d = 0.25\,\mathrm{m}$, D_c^s needs to be larger than ~ 2.7 m, or fracture energy larger than $\sim 60\,\mathrm{MJ/m^2}$, in order to satisfy a high-frequency power ratio of at least 10. The large fracture energy in the shallow region also prohibits the acceleration of up-dip rupture, limiting the rupture speed to about 2 km/s except in the region near the trench where supershear rupture tends to occur.

4.3. Energy Partitioning

The nature of an earthquake is controlled by partitioning of energy between the radiated energy, E_R, and the fracture energy, E_G, which is the energy used for advancing the fracture against resistance at the fault tip. Depending on whether E_R/E_G is large or small, we expect rapid or slow earthquakes, respectively. (Here, rapid earthquake is an earthquake with strong seismic radiation, and slow earthquake means an earthquake deficient in high frequency energy, like tsunami earthquakes.) We define the total available energy by $E_{T0} = E_R + E_G$, and call the ratio $\eta_R = E_R/E_{T0}$ the radiation efficiency (e.g., Kanamori and

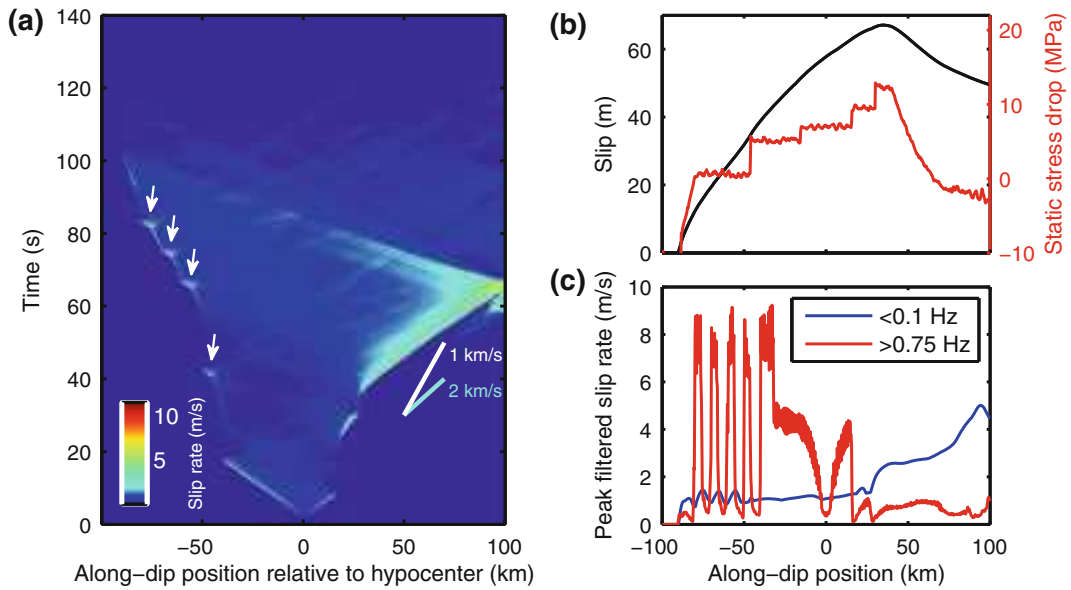

Figure 10
The spatial temporal distribution of slip rate (*left*), the along-dip distribution of final slip and static stress drop (*top right*), and the along-dip distribution of low-pass filtered (<0.1 Hz) and high-pass filtered peak slip rates (>0.75 Hz) (*bottom right*) in the third model. The *white arrows* in the left figure denote the regions of high-frequency bursts

Rivera 2006). In seismology, we can directly determine E_R from observations. We cannot estimate the total available energy directly from seismic observations, but if the friction follows the simple slip-weakening curve and if overshoot or undershoot is not very large, we can approximate E_{T0} by $\Delta\tau DS/2$, where $\Delta\tau$ is stress drop, D is the average slip and S is the fault area.

We compare η_R estimated from seismological observations with that estimated from the dynamic models studied here. Using the relation for the total available energy, the radiation efficiency can be written as $\eta_R = \left(\frac{2\mu}{\Delta\tau}\right)\left(\frac{E_R}{M_0}\right)$ which can be estimated from the shear modulus μ, the stress drop $\Delta\tau$, the radiated energy E_R, and the moment M_0. We use the CMT moment $M_0 = 5.31 \times 10^{22}$Nm, which is determined at a depth of 20 km, and $\mu = 44.1$ GPa at this depth in PREM. The estimation of radiated energy by different investigators ranges from 3 to 9×10^{17} J (Ide *et al.* 2011; Newman 2011; Lay *et al.* 2012). Then as the estimated stress drop varies from 4.8–10 MPa (Koketsu *et al.* 2011; Lay *et al.* 2011; Lee *et al.* 2011; Yagi and Fukahata 2011), the radiation efficiency η_R ranges from 0.05 to 0.31.

In the dynamic models, we can compute E_R and E_{T0} directly using the stress parameters and slip in the models:

$$E_{T0} = \frac{1}{2}\int_0^L (\tau_0(x) - \tau_1(x))D(x)\mathrm{d}x \tag{2}$$

$$E_R = E_{T0} - \int_0^L \left\{ \int_0^D \left[\tau(\tilde{D}, x) - \tau_1(x)\right]\mathrm{d}\tilde{D}(x) \right\}\mathrm{d}x \tag{3}$$

where $\tilde{D}$, D and τ_1 are the slip, final slip and final stress, respectively, at a given location x. The radiation efficiencies of the first, second and third models thus calculated are 0.33, 0.39, and 0.5, respectively. These values are higher than current seismological estimates of η_R. Including energy dissipation mechanisms such as off-fault plasticity may help reduce the radiation efficiency (Ma and Hirakawa 2013), but it can also diminish the final slip near the trench. Considering the many assumptions we made for our dynamic models (2-dimensionality and the specific dissipation mechanism) and the uncertainties in the

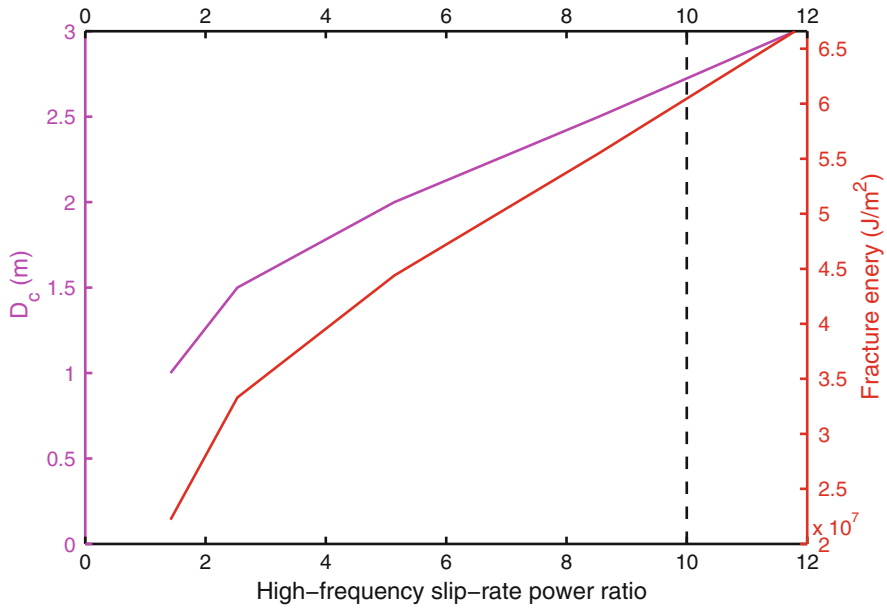

Figure 11
The high-frequency slip-rate power ratio for different values of D_c and fracture energy in an 80-km-wide region 20 km eastward from the hypocenter, when D_c in the deep region is kept at 0.25 m

seismological parameters, we consider the values of η_R to be in agreement only approximately. Our objective here is to illustrate how dynamic models can be compared with the real earthquake through energy partitioning. As seismological methodology improves, we expect the uncertainties in seismological parameters to decrease significantly. Also, incorporating more realistic 3-dimensional structure and fault zone constitutive laws in dynamic modeling may eventually enable more meaningful comparisons between the physical models and real earthquakes. What is presented here is an illustration of how to make such comparisons.

4.4. *Effects of the Subduction Wedge*

One unexpected feature of the Tohoku-Oki earthquake is its propagation to the shallow region and the resulting large slip. To find how the subduction wedge (the structure between free surface and plate interface) with shallow dip angle can affect the rupture propagation, we first compare our results to a rupture simulation on a fault with a dip angle of 90°. The hypocenter is 100 km deep, and model parameters are the same as those prescribed in the first model (Fig. 5). We find that on the vertical fault the rupture stops when it reaches the region with a small stress drop at $\sim$27.5 km upward from the hypocenter. In contrast, the up-dip rupture reaches the trench in our models of a shallow dipping fault. This indicates that without the subduction wedge the rupture is unable to propagate to the shallow region, unless stress drop is increased or fracture energy is reduced there.

We also run a rupture simulation on a horizontal fault at a depth of 25 km (the hypocentral depth in our models of the Tohoku-Oki earthquake) from the free surface. Given the same model parameters, we find that the rupture can propagate as far as where the trench would be (100 km eastward from the hypocenter). This shows that the effect of the free surface enables rupture to the trench despite the small stress drop in the shallow region. The structure of the subduction wedge is even more favorable for rupture propagation as the shallow region is closer to the free surface than is the hypocenter. Waves reflected by the free surface induce transient reduction of normal stress and increase of shear stress on the fault that lead

to large transient stress drop (KOZDON and DUNHAM 2013), which promotes the rupture propagation.

Our assumed fault geometry is simplified with a constant dip angle of 14°, while the real plate interface starts at a much smaller angle 4.6° (KIMURA *et al*. 2012) and steepens with depth. As the subduction wedge can amplify the final slip, the real stress drop in the region near the trench needs to be much smaller than in our models. The subduction wedge also leads to rupture acceleration, which produces high-frequency radiation. This effect is expected to be stronger in a subduction wedge with a smaller dipping angle. Thus, fracture energy (or D_c) may also need to be larger in order to inhibit the high-frequency radiation in the shallow region. Our models provide an upper bound for the average stress drop and a lower bound for the fracture energy in the shallow region.

5. Conclusions

We presented dynamic rupture models of the Tohoku-Oki earthquake by integrating key observational constraints. We assumed a fault governed by slip-weakening friction, with asperities of different frictional properties, and used the final slip distribution and the high-frequency radiation to constrain the stress drop and D_c. We used three models to reproduce the three typical along-dip slip profiles obtained by finite fault source inversions. Rupture properties estimated by our dynamic modeling such as rupture velocity and slip rate are consistent with the observations, though variations do exist in different models. Overall, in our models the average static stress drop of the event is in the range of 4.5–7 MPa, and fracture energy in the shallow region is in the order of 10 MJ/m^2. Stress drop reaches values of order 10 MPa in the regions of maximum slip, as also suggested by slip inversions (YAGI and FUKAHATA 2011). The coseismic slip distributions constrain the size of the shallow region of negative stress drop, which can be associated with strengthening materials that delineate the upper limit of the seismogenic zone. We find that the radiation efficiency computed for our models is larger than 0.3, somewhat larger than that inferred from seismic data. This may indicate that additional forms of energy dissipation are needed.

Acknowledgments

This work was supported by NSF grants EAR-0944288 and EAR-1015704, the Gordon and Betty Moore Foundation, the Japan Nuclear Energy Safety Organization (JNES) and SCEC (funded by NSF EAR-0106924 and USGS 02HQAG0008 cooperative agreements).

Appendix

The amplitude spectrum of slip rate in a rupture model with process zone (Fig. 4) can be expressed as a function of final slip D, the first corner frequency $f_{ris} = 1/t_{ris}$ and the second corner frequency $f_{pz} = 1/t_{pz}$. The amplitude spectrum is flat until the first corner frequency, and then decreases as a function of $f^{-1/2}$. After the second corner frequency, the amplitude spectrum decreases as a function of $f^{-3/2}$ in the case of the linear slip-weakening friction law (Fig. 5c in KANEKO *et al.* 2008). Thus, the amplitude spectrum can be expressed as:

$$v(f) = \begin{cases} D \text{ if } f < f_{ris} \\ D\left(\frac{f_{ris}}{f}\right)^{1/2} \text{if} \quad f_{ris} < f < f_{pz} \\ D\left(\frac{f_{ris}}{f_{pz}}\right)^{1/2}\left(\frac{f_{pz}}{f}\right)^{3/2} \text{if} \quad f > f_{pz} \end{cases} \qquad (A-1)$$

As can be seen from Fig. 4, the largest deep/shallow ratio of slip rate α happens when $f \geq f_{pz}$:

$$\alpha = \frac{D^d\sqrt{f_{ris}^d f_{pz}^d}}{D^s\sqrt{f_{ris}^s f_{pz}^s}}. \qquad (A-2)$$

The formula for second corner frequency f_{pz} in Mode II is:

$$f_{pz} = \frac{(1-\upsilon)\Delta\tau_s v_R}{\mu D_c} A_{II}(v_R), \qquad (A-3)$$

where ν is Poisson's ratio, μ is shear modulus, $\Delta\tau_s$ is strength drop, v_R is the rupture velocity, and A_{II} is a function of v_R (Equation (5.3.11) in FREUND 1990). By combining (A-2) and (A-3) and assuming a uniform Poisson's ratio and shear modulus, the shallow/deep D_c ratio can be expressed as a function of α:

$$\frac{D_c^s}{D_c^d} = \alpha \frac{D^s}{D^d} \left(\frac{f_{ris}^s}{f_{ris}^d} \right)^{\frac{1}{2}} \frac{\Delta\tau_s^s v_R^s}{\Delta\tau_s^d v_R^d} \frac{A_{II}^s\left(v_R^s\right)}{A_{II}^d\left(v_R^d\right)}. \qquad (A-4)$$

The final slip, rise time and rupture velocity can be inferred from slip inversions. The strength drop is our model parameter. For example in our first model, as $\left(\frac{f_{ris}^s}{f_{ris}^d}\right)^{\frac{1}{2}} \sim 1$, $\frac{\Delta\tau_s^s v_R^s}{\Delta\tau_s^d v_R^d} \sim 1$, and $\frac{A_{II}^s\left(v_R^s\right)}{A_{II}^d\left(v_R^d\right)} \sim 1$, we can simplify (A-4) to:

$$\frac{D_c^s}{D_c^d} \approx \alpha \left(\frac{D^s}{D^d} \right). \qquad (A-5)$$

As the observed high-frequency slip rate power ratio is at least 10, α has to be larger than $\sqrt{10}$. Given $\frac{D^s}{D^d} \sim 2$–3 the shallow/deep D_c ratio is larger than 6 to 9. Note that the needed D_c ratio (>10) in our model is larger than this range, as the observed power ratio involves smoothing in time and space. Thus, (A-4) and (A-5) only give a lower bound of the shallow/deep D_c ratio.

References

Ampuero, J. P. (2009), *SEM2DPACK, A spectral element method tools for 2D wave propagation and earthquake source dynamics*, User's Guide, version 2.3.6. Available online at http://www.sourceforge.net/projects/sem2d/.

Andrews, D. J. (1985), *Dynamic plane-strain shear rupture with a slip-weakening friction law calculated by a boundary integral method*, Bull. Seismol. Soc. Am., *75*, 1–21.

Aochi, H., and Ide, S. (2011), *Conceptual multi-scale dynamic rupture model for the 2011 off the Pacific coast of Tohoku Earthquake*, Earth Planets Space, *63*, 761–765.

Duan, B. (2012), *Dynamic rupture of the 2011 Mw 9.0 Tohoku-Oki earthquake: Roles of a possible subducting seamount*, J. Geophys. Res., *117*, B05311.

Freund, L. B., Dynamic fracture mechanics (Cambridge Univ. Press, Cambridge 1990).

Fujiwara, T., Kodaira, S., No, T., Kaiho, Y., Takahashi, N., and Kaneda, Y. (2011), *The 2011 Tohoku-Oki earthquake: Displacement reaching the trench axis*, Science, *334*, 1240.

Goto, H., Yamamoto, Y., and Kita, S. (2012), *Dynamic rupture simulation of the 2011 off the Pacific coast of Tohoku Earthquake: Multi-event generation within dozens of seconds*, Earth Planets Space, *64*, 1167–1175.

Huang, Y., Meng, L., and Ampuero, J.-P. (2012), *A dynamic model of the frequency-dependent rupture process of the 2011 Tohoku-Oki earthquake*, Earth Planets Space, *64*, 1061–1066.

Hyndman, R. D., Yamano, M., and Oleskevich, D. A. (1997), *The seismogenic zone of subduction thrust faults*, Island Arc, *6*, 244–260.

Ide, S., Baltay, A., and Beroza, G. C. (2011), *Shallow dynamic overshoot and energetic deep rupture in the 2011 Mw 9.0 Tohoku-Oki earthquake*, Science, *332*, 1426–1429, 2011.

Igarashi, T., Matsuzawa, T., and Hasegawa, A. (2003), *Repeating earthquakes and interplate aseismic slip in the northeastern Japan subduction zone*, J. Geophys. Res., *108*, 2249.

Iinuma, T., Hino, R., Kido, M., Inazu, D., Osada, Y., Ito, Y., Ohzono, M., Tsushima, H., Suzuki, S., Fujimoto, H., and Miura, S. (2012), *Coseismic slip distribution of the 2011 off the Pacific Coast of Tohoku Earthquake (M9.0) refined by means of seafloor geodetic data*, J. Geophys. Res., *117*, B07409.

Ito, Y., Tsuji, T., Osada, Y., Kido, M., Inazu, D., Hayashi, Y., Tsushima, H., Hino, R., and Fujimoto, H. (2011), *Frontal wedge deformation near the source region of the 2011 Tohoku-Oki earthquake*, Geophys. Res. Lett., *38*, L00G05.

Kanamori, H., and Rivera, L., Energy partitioning during an earthquake, Earthquakes: Radiated energy and the physics of faulting (AGU Monograph Series 170, Washington D. C., 2006) pp. 3–14.

Kaneko, Y., Lapusta, N., and Ampuero, J.-P. (2008), *Spectral element modeling of spontaneous earthquake rupture on rate and state faults: Effects of velocity-strengthening friction at shallow depth*, J. Geophys. Res., *113*, B09317.

Kato, N., and Yoshida, S. (2011), *A shallow strong patch model for the 2011 great Tohoku-oki earthquake: a numerical simulation*, Geophys. Res. Lett., *38*, L00G04,

Kido, M., Osada, Y., Fujimoto, H., Hino, R., and Ito, Y. (2011), *Trench-normal variation in observed seafloor displacements associated with the 2011 Tohoku-Oki earthquake*, Geophys. Res. Lett., *38*, L24303.

Kimura, G., Hina S., Hamada, Y., Kameda, J., Tsuji, T., Kinoshita, M., and Yamaguchi, A. (2012), *Runaway slip to the trench due to rupture of highly pressurized megathrust beneath the middle trench slope: The tsunamigenesis of the 2011 Tohoku earthquake off the east coast of northern Japan*, Earth Planet. Sci. Lett., *339–340*, 32–45.

Kiser, E., and Ishii, M. (2012), *The March 11, 2011 Tohoku-oki earthquake and cascading failure of the plate interface*, Geophys. Res. Lett., *39*, L00G25.

Kodaira, S., No, T., Nakamura, Y., Fujiwara, T., Kaiho, Y., Miura, S., Takahashi, N., Kaneda, Y., and Taira, A. (2012), *Coseismic fault rupture at the trench axis during the 2011 Tohoku-oki earthquake*, Nature Geosci., *5*, 646–650.

Koketsu, K., Yokota, Y., Nishimura, N., Yagi, Y., Miyazaki, S., Satake, K., Fujii, Y., Miyake, H., Sakai, S., Yamanaka, Y., and Okada, T. (2011), *A unified source model for the 2011 Tohoku earthquake*, Earth Planet. Sci. Lett., *310*, 480–487.

Kozdon, J. E., and Dunham, E. M. (2013), *Rupture to the trench: Dynamic rupture simulations of the 11 March 2011 Tohoku earthquake*, Bull. Seismic. Soc. Am., *103*, 1275–1289.

Lay, T., Ammon, C. J., Kanamori, H., Xue, L., and Kim, M. J. (2011), *Possible large near-trench slip during the 2011 Mw 9.0 off the Pacific coast of Tohoku earthquake*, Earth, Planets Space, *63*, 687–692.

Lay, T., Kanamori, H., Ammon, C. J., Koper, K. D., Hutko, A. R., Ye, L., Yue, H., and Rushing, T. M. (2012), *Depth-varying rupture properties of subduction zone megathrust faults*, J. Geophys. Res., *117*, B04311.

Lee, S.-J., Huang, B.-S., Ando, M., Chiu, H.-C., and Wang, J.-H. (2011), *Evidence of large scale repeating slip during the 2011 Tohoku-Oki earthquake*, Geophys., Res. Lett., *38*, L19306.

Ma, S., and Hirakawa, E. T. (2013), *Dynamic wedge failure reveals anomalous energy radiation of shallow subduction earthquakes*, Earth Planet. Sci. Lett., *375*, 113–122.

MADARIAGA, R. (1983), *High-frequency radiation from dynamic earthquake fault models*, Ann. Geophys., *1*, 17–23.

MENG, L., INBAL, A., and AMPUERO, J.-P. (2011), *A window into the complexity of the dynamic rupture of the 2011 Mw 9 Tohoku-Oki earthquake*, Geophys. Res. Lett., *38*, L00G07.

NEWMAN, A. (2011), Written Communication, May 3, 2011.

NODA, H., and LAPUSTA, N. (2012), *On averaging interface response during dynamic rupture and energy partitioning diagrams for earthquakes*, J. Appl. Mech., *79*, 031026.

NODA, H., and LAPUSTA, N. (2013), *Stable creeping fault segments can become destructive as a result of dynamic weakening*, Nature, *493*, 518–523.

SATO, H., ISHIKAWA, T., UJIHARA, N., YOSHIDA, S., FUJITA, M., MOCHIZUKI, M., and ASADA, A. (2011), *Displacement above the hypocenter of the 2011 Tohoku-Oki earthquake*, Science, *332*, 1395.

SIMONS, M., *et al*. (2011), *The 2011 magnitude 9.0 Tohoku-Oki earthquake: Mosaicking the megathrust from seconds to centuries*, Science, *332*, 1421–1425.

TAJIMA, F., MORI, J., and KENNETT, B. L. N. (2013), *A review of the 2011 Tohoku-Oki earthquake (Mw 9.0): Large-scale rupture across heterogeneous plate coupling*, Tectonophysics, *586*, 15–34.

TOBIN, H. J., and SAFFER, D. M. (2009), *Elevated fluid pressure and extreme mechanical weakness of a plate boundary thrust, Nankai Trough subduction zone*, Geology, *37*, 679-682.

WEI, S., GRAVES, R., HELMBERGER, D., AVOUAC, J.-P., and JIANG, J. (2012), *Sources of shaking and flooding during the Tohoku-Oki earthquake: A mixture of rupture styles*, Earth Planet. Sci. Lett., *333–334*, 91–100.

YAGI, Y., and FUKAHATA, Y. (2011), *Rupture process of the 2011 Tohoku-oki earthquake and absolute elastic strain release*, Geophys. Res. Lett., *38*, L19307.

YOSHIDA, S., and KATO, N. (2011), *Pore pressure distribution along plate interface that causes a shallow asperity of the 2011 great Tohoku-oki earthquake*, Geophys. Res. Lett., *38*, L00G13.

YUE, H., and LAY, T. (2011), *Inversion of high-rate (1sps) GPS data for rupture process of the 11 March 2011 Tohoku earthquake (Mw 9.1)*, Geophys. Res. Lett., *38*, L00G09.

(Received May 2, 2013, revised September 8, 2013, accepted September 17, 2013)

Appendix B. Dynamic earthquake rupture modeled with an unstructured 3D spectral element method applied to the 2011 M9 Tohoku earthquake (Galvez et al., 2014).

submitted to *Geophys. J. Int.*

Dynamic earthquake rupture modeled with an unstructured 3D spectral element method applied to the 2011 M9 Tohoku earthquake

P. Galvez[1], J.-P. Ampuero[2], L. A. Dalguer[1], S. N. Somala[2] and T. F. Nissen-Meyer[3]

[1]*Swiss Seismological Service, ETH Zurich, Zurich, Switzerland*

[2]*Seismological Laboratory, California Institute of Technology, Pasadena, USA*

[3]*Department of Earth Sciences, University of Oxford, England.*

Contact email: percy.galvez@sed.ethz.ch

SUMMARY

An important goal of computational seismology is to simulate dynamic earthquake rupture and strong ground motion in realistic models that include crustal heterogeneities and complex fault geometries. To accomplish this, we incorporate dynamic rupture modeling capabilities in a spectral element solver on unstructured meshes, the 3D open source code SPECFEM3D, and employ state-of-the-art software for the generation of unstructured meshes of hexahedral elements. These tools provide high flexibility in representing fault systems with complex geometries, including faults with branches and non-planar faults. The domain size is extended with progressive mesh coarsening to maintain an accurate resolution of the static field. Our implementation of dynamic rupture does not affect the parallel scalability of the code. We verify our implementation by comparing our results to those of two finite element codes on benchmark problems including branched faults. Finally, we present a preliminary dynamic rupture model of the 2011 Mw 9.0 Tohoku earthquake including a non-planar plate interface with heterogeneous frictional properties and initial stresses. Our simulation reproduces qualitatively the depth-dependent frequency content of the source and the large slip close to the trench observed for this earthquake.

Key words: Dynamic earthquake rupture. Computational seismology. Spectral element method.

1 INTRODUCTION

3-D numerical methods for earthquake rupture dynamics and ground motion simulation capable of incorporating complex non-planar fault systems, rough surface topography, non-linear rheologies and the heterogeneous structure of the Earth interior (e.g. Ma et al. 2007; Barall 2009; Ely et al. 2009, 2010; Tago et al. 2012; Pelties et al. 2012) are gaining increasing importance in the study of the physics of earthquakes. Because rupture dynamics involves small-scale processes that need to be accurately resolved (e.g. Day et al. 2005), such numerical simulations pose high demands in terms of memory and running time and need parallel computation on thousands of processors to achieve an accurate numerical solution of the dynamic rupture process. Today's supercomputer resources are allowing earthquake scientists to use such numerical models to investigate the physics of earthquakes at high resolution and large scales that were previously beyond hardware capabilities (Olsen et al. 2009). This new era of large-scale high-resolution 3D numerical calculations allows to unveil new features of the rupture propagation, contributing to a better understanding of the mechanics and physics of earthquakes, which in turn provides useful insights for improving our capability to predict ground motion for assessment of seismic hazard.

Dynamic earthquake models usually idealize the rupture process as a dynamically running shear crack on a frictional interface embedded in an elastic continuum. The spatio-temporal evolution of stress and slip during fault rupture is determined by solving the elastodynamic equation coupled to frictional sliding, leading to a highly nonlinear mixed boundary value problem (e.g. Andrews 1976, Das & Aki 1977; Day 1982). These dynamic models have been implemented in several volumetric 3-D numerical algorithms based on finite difference methods (FDM), the different classes of finite element methods (FEM) and finite volume methods (e.g. Dalguer & Day 2006, 2007; Kaneko et al. 2008; Dalguer 2012; Tago et al. 2012; Pelties et al. 2012; Kozdon & Dunham 2013; and references therein). Standard FDM, though widely used for wave propagation, are limited to planar faults and

face serious difficulties to be extended to complex fault geometries. A notable exception in 3D is the FDM of Ely et al. (2009, 2010) that uses different operators with irregular geometries. FEM overcomes this difficulty naturally owing to its capability to mesh general geometries. However, traditional, low-order FEM with mass lumping produces dispersion and nonphysical oscillations that need to be damped. High-order FEMs, such as spectral element methods (SEM) (e.g Festa & Vilotte, 2005; Kaneko et al. 2008), and discontinuous Galerkin methods (DGM) (e.g. Tago et al. 2012; Pelties et al. 2012), with diagonal mass matrices by construction, are very accurate and maintain the geometrical flexibility. Here we build upon the unstructured 3D open source spectral element code SPECFEM3D (http://www.geodynamics.org/cig/software/specfem3d). It is a Fortran 90 code parallelized using Message Passing Interface (MPI) for large-scale simulations and it is highly scalable. It was introduced in seismology as a solver for the elastic wave equation by Komatitsch & Vilotte 1998 and Komatitsch & Tromp (1999, 2002). The main characteristic of SEM, compared to the standard FEM, is that it uses high-order basis functions that make the method accurate enough to solve the wave equations only with 4 to 5 nodes per wavelength in most practical situations (Komatitsch & Tromp 1999). The mass matrix is naturally diagonalized by using the Gauss-Lobatto-Legendre (GLL) nodes inside the elements for both quadrature an interpolation, while preserving the accuracy (De Basabe & Sen 2010). Complex geometries are handled with unstructured hexahedral elements using a mesh generation tool such as CUBIT (http://cubit.sandia.gov/), which is interfaced to the unstructured version of SPECFEM3D (Peter et al. 2011).

Here we present the implementation of the boundary conditions for spontaneous dynamic rupture into SPECFEM3D. Our implementation follows the principles introduced by Kaneko et al. (2008) and involves encapsulated modules plugged into the SPECFEM3D code. It provides the capability to model dynamic rupture for multiple, non-planar faults governed by slip-weakening friction and rate-and-state friction. We verify the efficiency and accuracy of our implementation. We show that the

parallel computation is scalable to thousands of processors, enabling high-performance execution for large-scale dynamic rupture calculations. The accuracy of the code is successfully verified through benchmark problems developed by the SCEC/USGS dynamic rupture code validation project (Harris et al. 2009), including 3D problems with branched faults. We finally apply our new tool to develop a preliminary dynamic model of the rupture process of the 2011 Mw 9.0 Tohoku earthquake incorporating a 3-D non-planar geometry of the megathrust interface.

2 MODELING 3D RUPTURE DYNAMICS

2.1 Statement of the problem

We consider the problem of spontaneous earthquake rupture propagation on a pre-existing fault surface Γ embedded in an elastic medium Ω enclosed by a surface $\partial\Omega$. The evolution of slip is controlled by a friction law and the initial stresses on the fault, see Figure 1. The problem is governed by the linear elastodynamic equations:

$$\rho\ddot{u} = \nabla \cdot \sigma \tag{1}$$

where ρ is the density of the medium, σ stress tensor and u the incremental displacement field. We assume linear elasticity and small displacements (Hooke's law):

$$\sigma = c : \varepsilon, \tag{2}$$

where c is the elastic tensor and ε the strain defined as $(\nabla u + \nabla u^T)/2$. We also assume zero initial conditions on displacements and velocities and free stress boundary conditions at the surface of the Earth ($\sigma \cdot n = 0$, where n is the vector normal to the free surface). In practice, the model domain is truncated to a finite size and approximate absorbing boundary conditions are applied on the artificial

exterior boundaries (Komatitsch & Tromp 1999). However, to simplify this presentation we will ignore the absorbing boundary conditions. We treat the fault as a surface of displacement discontinuity. We represent the fault as a 2D interface composed of two matching surfaces in contact, $\Gamma = \Gamma_+ \bigcup \Gamma_-$ (Figure 1). The slip is defined as the displacement discontinuity across the fault,

$$s = u_+ - u_- \tag{3}$$

where u_+ and u_- denote the displacements on Γ_+ and Γ_-, respectively. The traction on the fault surface Γ_- is denoted by:

$$T = \sigma \cdot n \tag{4}$$

where n is the normal vector of Γ_-, pointing towards Γ_+ (see Figure 1). To simplify this presentation, we ignore the possibility of fault opening: $s \cdot n = 0$. We denote by T^T and T^N the tangential and normal tractions on Γ_-. The normal traction is negative in compression. The friction boundary conditions on the fault interface are:

$$|T^T| - \mu |T^N| \leq 0 \tag{5}$$

$$|\dot{s}|(|T^T| - \mu |T^N|) = 0 \tag{6}$$

$$\dot{s}|T^T| - |\dot{s}|T^T = 0 \tag{7}$$

where $\dot{s}$ is the slip velocity vector and μ is the friction coefficient, which can depend on slip, slip rate and other fault state variables. Here we adopt the linear slip weakening friction law (e.g. Palmer & Rice 1973; Ida 1973; Andrews 1976):

$$\mu = \mu_s - (\mu_s - \mu_d) \min \left(\frac{\delta}{D_c}, 1 \right) \tag{8}$$

$$\dot{\delta} = |\dot{s}| \tag{9}$$

where μ_s and μ_d are the static and dynamic friction coefficients respectively, D_c the critical slip distance, δ and $\dot{\delta}$ are the magnitude of the slip and slip rate respectively. Despite its simplicity, this friction law represents key features of fault strength: a finite friction coefficient μ, progressive weakening $(\mu_s - \mu_d)$, and finite fracture energy

$$G_c = \frac{1}{2}(\mu_s - \mu_d)D_c. \tag{10}$$

In order to reduce spurious high frequency oscillations due to the discrete nature of the numerical method, we introduce Kelvin-Voigt damping (Day & Ely 2002) in a narrow layer of elements surrounding the fault. This amounts to replace the strain ε in equation (2) by $\varepsilon + \eta\dot{\varepsilon}$. This introduces a frequency dependent quality factor $Q^{-1} = \omega\eta$, where ω is frequency.

2.2 Variational formulation

Like in the finite element method, the SEM discretizes the weak (variational) form of the governing equation (1) by doting it with an arbitrary test vector w and integrating over a finite volume Ω. After integrating by parts and applying the free surface boundary condition on $\partial\Omega$, we get :

$$\int_\Omega \rho w \cdot \ddot{u} + \int_\Omega \nabla w : \sigma = \int_\Gamma w \cdot T. \tag{11}$$

The fault is viewed as an infinitely thin closed hole, a slit, whose surface Γ is naturally portioned into two surfaces in contact, $\Gamma = \Gamma_+ \bigcup \Gamma_-$. The solution and test functions are described by smooth fields inside the domain Ω with a slit Γ. This naturally allows for a displacement discontinuity across the fault Γ. The left hand side of equation (11) can be decomposed over the two faces in contact,

$$\int_{\Gamma} w \cdot T = \int_{\Gamma_-} w_- \cdot T_- + \int_{\Gamma_+} w_+ \cdot T_+, \tag{12}$$

where the traction in each surface satisfies $T_- = -T_+$. Taking as a reference the Γ_- fault side, we define $T = T_-$ and obtain:

$$\int_{\Gamma} w \cdot T = \int_{\Gamma_+} \Delta w \cdot T, \tag{13}$$

where $\Delta w = w_+ - w_-$ is the difference of the test function across the fault. Finally, replacing (13) in (11) we get the elastodynamic equation with the fault term included:

$$\int_{\Omega} \rho w \cdot \ddot{u} + \int_{\Omega} \nabla w : \sigma = \int_{\Gamma_+} \Delta w \cdot T. \tag{14}$$

The problem is to find u that satisfies (14) for all w together with Hooke's law (2), the friction conditions (5)-(7), the friction law (8)-(9) and the given initial conditions.

2.3 Discrete formulation

The discretization of the weak form of the elastodynamic equation (14) by the spectral element method leads to the matrix equation:

$$M\ddot{u} + Ku = B\tau \tag{15}$$

where M and K are the mass and stiffness matrix, respectively, given by Komatitsch & Tromp (2002) and B is the fault boundary matrix given by Kaneko et al. (2008). The relative fault traction is $\tau = T - T_o$ where T_o is the initial stress on the fault. The time discretization is done with a central explicit

Newmark algorithm:

$$u_{n+1} = u_n + \Delta t \dot{u}_n + \frac{\Delta t^2}{2} \ddot{u}_n, \tag{16}$$

$$M\ddot{u}_{n+1} = -Ku_{n+1} + B\tau_{n+1}, \tag{17}$$

$$\dot{u}_{n+1} = \dot{u}_n + \frac{\Delta t}{2}(\ddot{u}_n + \ddot{u}_{n+1}). \tag{18}$$

where $u_n, \dot{u}_n$, and $\ddot{u}_n$ represent the particle displacement, velocity and acceleration at the n^{th} time step, respectively, and Δt is the time step size. To update the values of fault traction, we manipulate equations (17) and (18) on the fault split nodes to obtain the following expression:

$$T_{n+1} = \tilde{T}_{n+1} - Z\Delta\dot{u}_{n+1}, \tag{19}$$

where

$$Z = \frac{2}{\Delta t}(M_+^{-1}B_+ + M_-^{-1}B_-)^{-1} \tag{20}$$

is the fault impedance matrix,

$$\tilde{T}_{n+1} = Z\Delta\dot{\tilde{u}}_{n+1} + T_o \tag{21}$$

is the "stick traction" that would prevail if the fault node suddenly arrested and

$$\dot{\tilde{u}}_{n+1} = u_n + \frac{\Delta t}{2}(\ddot{u}_n - M^{-1}Ku_{n+1}), \tag{22}$$

Subscripts $\pm$ denote values on the nodes lying on one of the two sides of the fault, $\Gamma_\pm$. Here we do not allow for fault opening, hence the slip velocity normal to the fault vanishes, $\Delta\dot{u}_{n+1}^N = 0$, and the

normal fault traction remains as:

$$T^N_{n+1} = \tilde{T}^N_{n+1}. \tag{23}$$

The explicit Newmark algorithm (16) readily provides an update of displacement and slip, with which we update the friction coefficient according to (8)-(9). To update the shear fault traction T^T we solve (19) together with the friction conditions (5)-(7). This can be efficiently done on a node-by-node basis, because the matrix Z is diagonal. The solution is:

$$T^T = \min\left(-\mu T^N, \|\tilde{T}^T\|\right) \frac{\tilde{T}^T}{\|\tilde{T}^T\|}. \tag{24}$$

We then compute the relative stress on the fault, $\tau = T - T_o$, reinsert it in equation (17) to update accelerations, and finally update velocities (18).

3 PARALLELIZATION AND SCALABILITY

In dynamic rupture simulations the computational mesh needs to be dense enough to resolve the breakdown zone at the rupture front, whose size is controlled by the rupture speed, frictional strength drop and slip-weakening distance (Day et al. 2005). The simulation of large earthquakes typically requires a node spacing less than a few hundred meters (Harris et al. 2009). For a total domain size of a few hundred km, the total number of spectral elements (e.g. with NGLL=5) needed is of the order of tens of millions. The elements carrying the fault interface need to be treated differently than the rest of the bulk, in order to satisfy the contact and friction conditions. One approach is to assign during domain decomposition all the spectral elements that are in contact with fault surfaces to a single processor. We initially adopted this strategy (as did Kaneko et al. 2008) for the simplicity of its implementation. However, for large simulations this approach leads to a major load imbalance, with a bottleneck waiting for the processor that contains the faults.

To achieve load balancing, we parallelized the fault solver as well. During domain decomposition, we assigned matching pairs of elements on both sides of the fault to the same processor, the one with lowest rank of the pair. This simplifies the implementation and avoids solver communications across the fault. The fault normal vector (n) and fault boundary matrix (B) were pre-assembled across MPI interfaces along the fault, and internal forces are globally assembled before passing them to the fault solver. Hence, no additional assembly operation (no additional inter-processor communication) is performed by the fault solver. This strategy is expected to generate a minimal impact on the overall cost of computations, which should remain dominated by the bulk wave propagation solver. The original SPECFEM3D code has been shown to have good scaling properties for wave propagation problems (Komatitsch et al. 2009). We demonstrate here that our implementation of fault dynamics does not affect its parallel scalability.

We illustrate the strong scaling of the code in the community-based SCEC dynamic rupture benchmark problem TPV5. The problem comprises a fault 30 km long and 15 km deep. We placed absorbing boundaries 15 km away along strike from the fault tips, 25 km below the bottom edge of the fault and 30 km away in the fault-normal direction. We adopted a spectral element size of 400 m with 5 GLL nodes per element edge, corresponding to the maximum recommended average grid size of 100 m (Harris et al. 2009). This resulted in 2,265,000 spectral elements. We ran the simulation at the Swiss National Supercomputing Center (CSCS) on Monte Rosa, a Cray XE6 system with 1496 compute nodes consisting of two 16-core AMD Opteron 6272 2.1 GHz CPUs and 32 GB of memory, and with high performance networking through a Gemini 3D torus interconnect. The theoretical peak performance of Rosa is 402 Tflops. We choose numbers of processors in powers of 2 ranging from 64 to 8192. We suppressed intermediate outputs, as our focus was on verifying the scaling of the combined bulk-fault solver. Figure 2(a) shows the total wall clock time taken by the solver (bulk and fault) to complete one TPV5 simulation. The code scales well within the range of number of processors we

tested. We also tested the scaling of the original SPECFEM3D code without fault implementation. For this purpose, we considered the same domain size and element size as that of our TPV5 simulations, but without the split-node fault surface, and we prescribed an explosion point source at the center of the domain. We repeated the scalability test in the same system and for the same set of processors as those previously used. The results, shown in Figure 2, demonstrate that the fault solver does not cause any significant load imbalance and does not affect the overall performance of the code.

While TPV5 was used to analyze strong scaling, for weak scaling we consider a different version of the same benchmark, TPV205. Essentially, a TPV5 (100 m grid size) run on 256 processors is compared with the same benchmark problem solved with 200 m grid size on 16 processors and 50 m grid size on 4096 processors. These three sets of simulations have, in principle, the same load per processor: the total number of operations for fixed domain size and duration scales as $1/(\text{grid size})^4$. Figure 2(b) shows the weak scalability results for SPECFEM3D with our fault implementation. Wall clock time is normalized with respect to that of the 50 m grid size simulation. The weak scalability is overall satisfactory. The minor (2%) deviation in weak scaling could be attributed to the fact that the number of spectral elements are not exactly 4 times those at lower resolution on the fault plane, as the dimensions of fault are fixed.

4 NUMERICAL TESTS: ASSESSMENT OF NUMERICAL SOLUTIONS

To verify our implementation of the dynamic rupture boundary conditions in SPECFEM3D, we have reproduced several 3-D test problems from the SCEC dynamic rupture code validation project (e.g. Harris et al. 2009; Harris et al. 2011) and compared our results to those of other published methods. Here we report only our verification results for the test problems TPV24 and TPV25 which are representative of the non-planar fault geometries that our method can handle. We first summarize the setting of these test problems, then we present our results and qualitative comparisons to other methods.

4.1 Description of the rupture problem on a branched fault

The SCEC test problems TPV24 and TPV25 consist of spontaneous rupture propagation on a branched fault system comprising two segments, a main fault and a branch fault, embedded in a uniform elastic isotropic halfspace (Figure 3). The two fault segments are vertical, planar, strike-slip faults that reach the Earth's surface. In TPV24 the faults are right-lateral, while in TPV25 they are left-lateral. The main fault is 28 km long and 15 km deep, and the branch fault is 12 km long and 15 km deep. The branch fault splays off the main fault at an angle of 30 degrees, at 12 km from the right edge of the main fault. It is assumed that the slip on the branch fault tapers smoothly to zero at the junction with the main fault. The S wave velocity is 3463 m/s, the P wave velocity is 6000 m/s and the density is 2670 m/s. The hypocenter is located on the main fault at 8 km to the left of the junction point and at 10 km depth. Rupture nucleation is achieved by prescribing time-weakening over a region that grows with smoothly variable rupture speed.

We employ a semi-spherical mesh with gradual increase of the element size as a function of radial distance (Figure 3b). Coarsening is an efficient approach to increase the domain size, which improves the accuracy of the static field. The spherical shape of the outer boundary allows the angle of incidence of waves on the absorbing boundaries to be closer to normal, which reduces spurious reflections. A smooth mesh coarsening is needed in the region surrounding the fault to avoid artificial wave reflections.

The time step in our simulations is $\Delta t = 0.5$ ms. To attenuate the spurious high frequency oscillations, we set the Kelvin-Voigt viscosity as $\eta = 0.3\Delta t_{fault}$ on the main fault and $\eta = 0.2\Delta t_{fault}$ on the branch, where $\Delta t_{fault} = 5.7$ ms is the elastic critical time step corresponding to the element size on the fault.

4.2 Results and comparison to other numerical methods

The complexity of rupture path selection in branched fault systems has been previously studied by Bhat et al. (2004) and DeDontney et al. (2012). The rupture propagates on the main fault passing through the junction point and, depending on the initial stress conditions, it may jump onto the branch fault. This is illustrated in Figure 4, which shows a series of snapshots of slip velocity for the TPV24 and TPV25 test problems. The rupture propagation paths obtained in these two cases are remarkably different. In the right-lateral case the rupture abandons the main fault and continues into the fault branch. The rupture successfully continues in the branch fault because it is located in the extensional side, where the dominantly tensile normal stress changes tend to reduce the frictional strength. In the left-lateral case, the rupture mainly propagates into the main fault and continues only a short distance into the branch fault. In both scenarios, rupture on one fault segment past the junction casts a stress shadow on the other segment that inhibits its activation (e.g. Harris & Simpson 1998).

We compare our results to two independent methods, the MAFE code by Ma & Liu (2006) and FaultMod code by Barall (2009). Both are finite element codes with split nodes. We consider solutions on a grid with size 100 m (this is the average GLL node spacing). Figure 5 shows the comparison of rupture times. The evolution of the rupture front from the three methods is in very good agreement on both fault segments and at all distances and directions from the hypocenter. A small discrepancy is observed at shallow depth on the branch fault in TPV24 when the rupture reaches the free surface. The time histories of slip rate produced by the three methods at selected fault locations, shown in Figure 6, are also in qualitatively good agreement.

We found general agreement between the three methods, including the details of rupture initiation, propagation and arrest. These and other SCEC test results not shown here (but available through the SCEC repository) verify our implementation of dynamic rupture in the SPECFEM3D-SESAME code. The software is now suitable to solve complex problems of dynamic rupture with irregular fault

geometry, while retaining the existing capabilities of the code for problems of wave propagation with complex media and irregular surface topography.

5 A CONCEPTUAL MODEL OF THE 2011 MW 9.0 TOHOKU EARTHQUAKE

5.1 Background and modeling scope

On March 11th 2011, a Mw 9.0 earthquake stroke Japan and triggered a devastating tsunami, causing severe damage in cities and nuclear facilities along the Japanese coast. A combination of seismological, geodetic, bathymetric and tsunami observations revealed a remarkable depth dependency of the frequency content of the source. We define two frequency bands: a LF band from 0.01 to 0.125 Hz and a HF band from 0.5 to 1 Hz. Large slip ($\sim$ 50 m) close to the trench was inferred by kinematic source inversions of seismic data in the LF band (e.g Suzuki et al. 2011; Koketsu et al. 2011; Lee et al. 2011) and from differential multi-beam bathymetry surveys (Fujiwara et al. 2011). Radiation in the HF band was identified in the deep areas of the plate interface by back-projection of teleseismic data (Meng et al. 2011). Downdip of the hypocenter the HF radiation was interspersed within a relatively slow rupture process.

Few dynamic rupture models have been proposed to investigate the physical features of this event. Duan (2012) presented a 3-D dynamic rupture simulation on a planar fault to demonstrate the possible role of a large subducted seamount on the rupture dynamics and on the generation of large slip. Mitsui (2013) also developed 3D dynamic models and concluded that the rupture around the hypocenter was enhanced by the stress accumulation due to the preceding M7-class earthquakes and triggered thermal pressurization of pore fluids in the near-trench area causing large slip, which promoted propagation of the rupture over a wide region. Ide et al. (2011) considered that an additional push to the earthquake rupture (slip reactivation) comes from the rupture front back propagating from the free-surface after rupturing the trench, a phenomena usually observed in dynamic rupture simulations of dipping faults

(Dalguer et al. 2001). Goto (2013) used a 2D inplane rupture model and showed that slip reactivation can result from heterogeneous stress distribution. Kozdon & Dunham (2013) proposed a 2D model that accounts for depth-dependent material properties, cruved fault geometry and seafloor geometry, and showed that despite velocity-strengthening properties at shallow depth, rupture can reach the trench. Huang et al. (2013a, 2013b) also use 2D inplane dynamic rupture models to provide a physical interpretation of the depth-dependent frequency content of seismic radiation, the variations of rupture speed and the large shallow slip.

Here we propose a minimalistic 3D dynamic rupture model consistent with this depth dependent frequency content of slip, where the shallow part radiates coherent energy at low frequency and the deep part at high frequency. The deep HF radiation is interpreted as the rupture of asperities in the bottom part of the seismogenic zone of the megathrust (e.g. Huang et al. 2013b; Lay et al. 2012). We set the model parameters by trial and error, taking as a starting point the 2D dynamic rupture models developed by Huang et al. (2013b). The model presented here should be considered as preliminary; a refined model quantitatively constrained by geophysical observations will be presented elsewhere.

Our simulation also serves to illustrate the capability of the spectral element method to handle non-planar fault geometries and narrow subduction wedges. The model accounts for the free surface, the slope of the outer wedge and the curved geometry of the subduction interface and the trench (Figure 7). The latter is based on a fault geometry adapted from Simons et al. (2011), which includes constraint from bathymetry, seismic reflection surveys and the Wadati-Benioff Zone delineated by seismicity (e.g Iwasaki et al. 2002; Miura et al. 2003). The software CUBIT generates high quality hexahedral meshes even in regions with small dipping angles close to the trench.

5.2 Model setup

We consider a homogeneous elastic medium with S wave velocity 3470 m/s, P wave velocity 5800 m/s and density 2700 kg/m^3. We assume the linear slip-weakening friction law and a distribution of asperities defined by heterogeneities of initial stress and critical slip distance D_c (Figure 8). We set an elliptical patch in the region of large slip and a collection of small circular asperities in deeper regions, mainly from 25 km to 55 km depth. The number, size and separation distance of the small asperities are set by trial and error to achieve a moderate average rupture speed of 2 km/s downdip of the hypocenter.

On the main asperity the stress drop is set to 9 MPa and on the small asperities to 12 MPa. Null stress drop and a high strength excess (24 MPa) are prescribed in the background. In dynamic rupture models constrained by statistical observations, surface-rupturing earthquakes are characterized by a large area of negative stress drop that enhances energy absorption close to the free surface (e.g. Dalguer et al. 2008; Pitarka et al. 2009). Subduction zones with large accretionary wedges exhibit an upper stable sliding region due to the presence of unconsolidated gouge and clays (Marone & Scholz 1988). Therefore we imposed a negative stress drop (average -2.5 MPa) in the shallow part of the fault interface (Figure 9(a)). Inspired by the hierarchical patch model developed by Ide & Aochi (2005) and Aochi & Ide (2009) where D_c varies with the asperity size, we prescribe $D_c = 3$ m on the large asperities, $D_c = 1$ m on the small ones and $D_c = 6$ m in the rest of the fault (Figure 9(b)). The distributions of static (μ_s) and dynamic (μ_d) friction coefficients and normal stress over the fault are shown in Figure 10. Rupture initiates by reducing the static friction coefficient in the nucleation area of radius 15km (green circle in Figure 10(a)), so that the initial static yielding stress ($\mu_s \sigma_n$) is slightly below the initial stress. This procedure does not alter the stress drop distribution shown in the Figure 9(a), i.e. no overstress has been applied on the nucleation patch.

5.3 Results and analysis

An overview of the rupture history produced by our model is given by Figures 11 to 13, which show the spatial distributions of slip velocity at selected times, rupture time and rupture speed, respectively. In the initial 40 seconds the rupture propagates mainly up-dip, starting slowly (about 1 km/s) and gradually accelerating, while the down-dip rupture front remains slow and weak.

At $t \approx 40$ s the updip rupture front reaches the shallow region of negative stress drop and its peak HF slip velocity decreases, while the downdip rupture starts breaking the deep asperities and generating intermittent HF radiation. At $t = 55.2$ s the rupture has reached the trench and has bounced back down-dip. As shown in Figure 13(b), near $t = 48.8$ s a secondary downdip rupture front emerges at the trench, disconnected from the main updip front, and at $t = 55.2$ s both fronts have coalesced. Supershear rupture appears close to the trench, likely caused by free surface effects (e.g. Day et al. 2008; Kaneko & Lapusta 2010). At $t = 65$ s rupture of the deep asperities continues down-dip of the hypocenter, with rupture speed of 3 km/s within the small asperities, 1 km/s in their surroundings and an average of about 2 km/s.

By $t = 81.2$ s the rupture has started propagating southwards, at speeds of 2.8-3.3 km/s. At $t = 107.2$ s the rupture has broken the southern large asperity and has started propagating up to the trench. Figure 12 shows general agreement between the rupture time in our simulation and the timing of the HF radiation spots determined by back-projection by Meng et al. (2011).

Figures 11, 14, 15 and 16 show aspects of our dynamic rupture model in three frequency bands: LF 0-0.125 Hz, IF 0.125 - 0.5 Hz and HF 0.5 - 1 Hz. Figures 14(a-b) compare our simulated peak slip velocity in the IF and HF bands, respectively, to the seismic energy release estimated by hybrid back-projection by Yagi et al. (2012) in the same frequency bands. Figure 14(c) compares our HF peak slip velocity to the back-projection results of Meng et al. (2011).

The static aspects of our model are also in general agreement with observations. Our dynamic

model generates a shallow region of large slip (∼50 m) coincident with large LF peak slip velocity. This region overlaps with the region of large slip inferred by kinematic source inversion by Yagi & Fukahata (2011) at frequencies lower than 0.2 Hz (Figure 15).

Figure 16 summarizes the spatial distribution of LF and HF peak slip rate. The simulation reproduces the general pattern of the observations: LF and IF radiation occurs mainly in the shallow part of the plate interface, from 0 to 25 km depth, where slip is larger than 40 m, whereas HF radiation occurs essentially in the deep small asperities, below 30 km depth, and extends over 300 km along strike. This distinct behavior is further illustrated in Figure 17, which shows the slip-weakening curve, slip rate, slip and slip rate spectrum at two locations inside a shallow and a deep asperity, respectively. The deep asperity has a sharp slip rate peak of 10 m/s and relatively small slip. The shallow asperity has smoother slip rate with peak of 5.5 m/s but larger slip reaching 55 m. The slip rate spectra confirm the different frequency content of slip in these two asperities. We also find that the HF slip rate is localized near the rupture front whereas the LF slip rate lags behind it.

Figure 18 shows sea floor displacements from our simulation and from ocean bottom geodetic measurements at five locations (Sato et al. 2011). The agreement is fair on the vertical components close to the hypocenter and good in the horizontal components at all stations. Close to the trench the sea floor displacements reach 8 m vertically, consistent with the generation of a large tsunami, and 30-40 m horizontally.

6 CONCLUSIONS

We added the capability to model spontaneous earthquake rupture dynamics in the unstructured version of the spectral element code SPECFEM3D. We compared our results of 3-D test problems of the SCEC/USGS dynamic rupture code validation project to other finite element methods, MAFE by Ma & Liu (2006) and FaultMod by Barall (2009), and found that rupture times and time histories of

slip rate are in good agreement. To asses the efficiency of our implementation we performed a strong scaling analysis. The results demonstrate that the dynamic rupture implementation does not cause any significant load imbalance and does not affect the overall performance of the code. A weak scalability also gave satisfactory results. The unstructured spectral element method coupled with our dynamic rupture implementation makes use of a versatile mesh generation tool (CUBIT) that enables dynamic rupture simulations on complex fault systems, for instance a non-planar faults with branches. We presented a dynamic rupture simulation of the 2011 Mw 9.0 Tohoku earthquake, a complex megathrust event in a non-planar fault with small dip angle close to the trench, which illustrates the versatility and stability of the method. Our dynamic model includes fault heterogeneity and reproduces two important observed features of the Tohoku earthquake: high frequency radiation in the deep areas of the plate interface and low frequency radiation and large slip ($\sim$50 m) at shallow depth close to the trench. Overall, our dynamic rupture implementation offers a great potential to simulate more realistic earthquakes in complex fault systems.

ACKNOWLEDGMENTS

This study was supported by the QUEST project (Quantitative Estimation of Earth's Seismic Sources and Structure) funded by the 7th Framework Programm of the European Commission, the ASCETE Project (Advanced Simulation of Coupled Earthquake and Tsunami Events) funded by the Volkswagen Foundation within the program "New Conceptual Approaches to Modeling and Simulation of Complex Systems", by the National Science Foundation (CAREER award EAR-1151926) and by the Southern California Earthquake Center (based on NSF Cooperative Agreement EAR-0529922 and USGS Cooperative Agreement 07HQAC0026). Simulations were done at the Swiss National Supercomputing Center (CSCS), under the production projects "Development of Dynamic Rupture Models to Study the Physics of Earthquakes and Near-Source Ground Motion" and "Development of a Database of Physics-Based Synthetic Earthquakes for Ground Motion Prediction".

REFERENCES

Andrews, D. J., 1976. Rupture Propagation With Finite Stress in Antiplane Strain, *Journal of Geophysical Research*, **81**(20).

Aochi, H. & Ide, S., 2009. Complexity in earthquake sequences controlled by multiscale heterogeneity in fault fracture energy, *Journal of Geophysical Research*, **114**(B3), B03305.

Barall, M., 2009. A grid-doubling finite-element technique for calculating dynamic three-dimensional spontaneous rupture on an earthquake fault, *Geophysical Journal International*, **178**(2), 845–859.

Bhat, H. S., Dmowska, R., Rice, J. R., & Nobuki, K., 2004. Dynamic Slip Transfer from the Denali to Totschunda Faults, Alaska: Testing Theory for Fault Branching, *Bulletin of the Seismological Society of America*, **94**, 212–213.

Dalguer, L. A., 2012. *Numerical Algorithms for Earthquake Rupture Dynamic Modeling. In "The mechanics of faulting: From Laboratory to Real Earthquakes"*, Rearch Signpost.

Dalguer, L. A. & Day, S. M., 2006. Comparison of Fault Representation Methods in Finite Difference Simulations of Dynamic Rupture, *Bulletin of the Seismological Society of America*, **96**(5), 1764–1778.

Dalguer, L. A. & Day, S. M., 2007. Staggered-grid split-node method for spontaneous rupture simulation, *Journal of Geophysical Research*, **112**(B2), B02302.

Dalguer, L. A., Irikura, K., Riera, J. D., & Chiu, H. C., 2001. The Importance of the Dynamic Source Effects on Strong Ground Motion during the 1999 Chi-Chi, Taiwan, Earthquake: Brief Interpretationof the Damage Distribution on Buildings, *Bulletin of the Seismological Society of America*, pp. 1112–1127.

Dalguer, L. A., Miyake, H., Day, S. M., & Irikura, K., 2008. Surface Rupturing and Buried Dynamic-Rupture Models Calibrated with Statistical Observations of Past Earthquakes, *Bulletin of the Seismological Society of America*, **98**(3), 1147–1161.

Das, D. & Aki, K., 1977. A numerical study of two-dimensional spontaneous rupture propagation, *Journal of Geophysical Research*, **50**, 643–668.

Day, S. M., 1982. Three-dimensional finite difference simulation of fault dynamics: Rectangular faults with fixed rupture velocity, *Bulletin of the Seismological Society of America*, **72**(3), 705–727.

Day, S. M. & Ely, G. P., 2002. Effect of a Shallow Weak Zone on Fault Rupture: Numerical Simulation of Scale-Model Experiments, *Bulletin of the Seismological Society of America*, **92**, 3022–3041.

Day, S. M., Dalguer, L. A., Lapusta, N., & Liu, Y., 2005. Comparison of finite difference and boundary integral solutions to three-dimensional spontaneous rupture, *Journal of Geophysical Research*, **110**(B12), B12307.

Day, S. M., Gonzalez, S. H., Anooshehpoor, R., & Brune, J. N., 2008. Scale-Model and Numerical Simulations of Near-Fault Seismic Directivity, *Bulletin of the Seismological Society of America*, **98**(3), 1186–1206.

De Basabe, J. D. & Sen, M. K., 2010. Stability of the high-order finite elements for acoustic or elastic wave propagation with high-order time stepping, *Geophysical Journal International*, **181**(1), 577–590.

DeDontney, N., Rice, J. R., & Dmowska, R., 2012. Finite Element Modeling of Branched Ruptures Including Off-Fault Plasticity, *Bulletin of the Seismological Society of America*, **102**(2), 541–562.

Duan, B., 2012. Dynamic rupture of the 2011 Mw 9.0 Tohoku-Oki earthquake: Roles of a possible subducting seamount, *Journal of Geophysical Research*, **117**(B5), B05311.

Ely, G. P., Day, S. M., & Minster, J.-B., 2009. A support-operator method for 3-D rupture dynamics, *Geophysical Journal International*, **177**(3), 1140–1150.

Ely, G. P., Day, S. M., & Minster, J. B., 2010. Dynamic Rupture Models for the Southern San Andreas Fault, *Bulletin of the Seismological Society of America*, **100**(1), 131–150.

Festa, G. & Vilotte, J.-P., 2005. The Newmark scheme as velocity-stress time-staggering: an efficient PML implementation for spectral element simulations of elastodynamics, *Geophysical Journal International*, **161**(3), 789–812.

Fujiwara, T., Kodaira, S., No, T., Kaiho, Y., Takahashi, N., & Kaneda, Y., 2011. The 2011 Tohoku-Oki Earthquake: Displacement Reaching the Trench Axis, *Science*, **334**.

Goto, 2013. Dynamic rupture simulation of the 2011 off the Pacific coast of Tohoku Earthquake: Multi-event generation within dozens of seconds, *Earth, Planets and Space*, **64**(12), 1167–1175.

Harris, R. A. & Simpson, W. R., 1998. Suppression of large earthquakes by stress shadows: A comparison of Coulumb and rate-and-state failure, *Journal of Geophysical Research*, **103**, 24.439–24.451.

Harris, R. A., Barall, M., Archuleta, R., Dunham, E., Aagaard, B., Ampuero, J. P., Bhat, H., Cruz-Atienza,

V., Dalguer, L., Dawson, P., Day, S., Duan, B., Ely, G., Kaneko, Y., Kase, Y., Lapusta, N., Liu, Y., Ma, S., Oglesby, D., Olsen, K., Pitarka, A., Song, S., & Templeton, E., 2009. The SCEC/USGS Dynamic Earthquake Rupture Code Verification Exercise, *Seismological Research Letters*, **80**(1), 119–126.

Harris, R. A., Barall, M., Andrews, D. J., Duan, B., Ma, S., Dunham, E. M., Gabriel, A. A., Kaneko, Y., Kase, Y., Aagaard, B. T., Oglesby, D. D., Ampuero, J. P., Hanks, T. C., & Abrahamson, N., 2011. Verifying a Computational Method for Predicting Extreme Ground Motion, *Seismological Research Letters*, **82**(5), 638–644.

Huang, Y., Ampuero, J.-P., & Kanamori, H., 2013a. Slip-Weakening Models of the 2011 Tohoku-Oki Earthquake and Constraints on Stress Drop and Fracture Energy, *Pure and Applied Geophysics*.

Huang, Y., Meng, L., & Ampuero, J. P., 2013b. A dynamic model of the frequency-dependent rupture process of the 2011 Tohoku-Oki earthquake, *Earth, Planets and Space*, **64**(12), 1061–1066.

Ida, Y., 1973. Stress Concentration and Unsteady Propagation of Longitudinal Shear Cracks, *Journal of Geophysical Research*, **78**.

Ide, S. & Aochi, H., 2005. Earthquakes as multiscale dynamic ruptures with heterogeneous fracture surface energy, *Journal of Geophysical Research*, **110**(B11), B11303.

Ide, S., Baltay, A., & Beroza, G. C., 2011. Shallow Dynamic Overshoot and Energetic Deep Rupture in the 2011 Mw 9.0 Tohoku-Oki Earthquake, *Science*, **332**(6036), 1426–1429.

Iwasaki, T., Yoshii, T., Ito, T., Sato, H., & Hirata, N., 2002. Seismological features of island arc crust as inferred from recent seismic expeditions in Japan, *Tectonophysics*, **335**, 53–66.

Kaneko, Y. & Lapusta, N., 2010. Tectonophysics, *Tectonophysics*, **493**(3-4), 272–284.

Kaneko, Y., Lapusta, N., & Ampuero, J. P., 2008. Spectral element modeling of spontaneous earthquake rupture on rate and state faults: Effect of velocity-strengthening friction at shallow depths, *Journal of Geophysical Research*, **113**(B9), B09317.

Koketsu, K., Yokota, Y., Nishimura, N., Yagi, Y., Miyazaki, S., Satake, K., Fujii, Y., Miyake, H., Sakai, S., Yamanaka, Y., & Okada, T., 2011. A unified source model for the 2011 Tohoku earthquake, *Earth and Planetary Science Letters*, **310**(3-4), 480–487.

Komatitsch, D. & Tromp, J., 1999. Introduction to the spectral element method for three-dimensional seismic wave propagation, **139**, 806–822.

Komatitsch, D. & Tromp, J., 2002. Spectral-element simulations of global seismic wave propagation—I. Validation, *Geophysical Journal International*, **149**, 390–412.

Komatitsch, D. & Vilotte, J.-P., 1998. The Spectral Element Method: An Efficient Tool to Simulate the Seismic Response of 2D and 3D Geological Structures, *Bulletin of the Seismological Society of America*, **88**(2), 368–392.

Komatitsch, D., Michéa, D., & Erlebacher, G., 2009. J. Parallel Distrib. Comput., *J. Parallel Distrib. Comput.*, **69**(5), 451–460.

Kozdon, J. E. & Dunham, E. M., 2013. Rupture to the Trench: Dynamic Rupture Simulations of the 11 March 2011 Tohoku Earthquake, *Bulletin of the Seismological Society of America*, **103**(2B), 1275–1289.

Lay, T., Kanamori, H., Ammon, C. J., Koper, K. D., Hutko, A. R., Ye, L., Yue, H., & Rushing, T. M., 2012. Depth-varying rupture properties of subduction zone megathrust faults, *Journal of Geophysical Research*, **117**(B4), B04311.

Lee, S.-J., Huang, B.-S., Ando, M., Chiu, H.-C., & Wang, J.-H., 2011. Evidence of large scale repeating slip during the 2011 Tohoku-Oki earthquake, *Geophysical Research Letters*, **38**(19).

Ma, S. & Liu, P., 2006. Modeling of the Perfectly Matched Layer Absorbing Boundaries and Intrinsic Attenuation in Explicit Finite-Element Methods, *Bulletin of the Seismological Society of America*, **96**(5), 1779–1794.

Ma, S., Archuleta, R. J., & Page, M. T., 2007. Effects of Large-Scale Surface Topography on Ground Motions, as Demonstrated by a Study of the San Gabriel Mountains, Los Angeles, California, *Bulletin of the Seismological Society of America*, **97**(6), 2066–2079.

Marone, C. & Scholz, C. H., 1988. The depth of seismic faulting and the upper transition from stable to unstable slip regimes, *Geophysical Research Letters*, **15**, 621–624.

Meng, L., Inbal, A., & Ampuero, J.-P., 2011. A window into the complexity of the dynamic rupture of the 2011 Mw 9 Tohoku-Oki earthquake, *Geophysical Research Letters*, **38**(7).

Mitsui, 2013. A scenario for the generation process of the 2011 Tohoku earthquake based on dynamic rupture

simulation: Role of stress concentration and thermal fluid pressurization, *Earth, Planets and Space*, **64**(12), 1177–1187.

Miura, S., Kodaira, S., Nakanishi, A., Tsuru, T., Takahashi, N., Hirata, N., & Kaneda, Y., 2003. Structural characteristics controlling the seismicity crustal structure of southern Japan Trench fore-arc region, revealed by ocean bottom seismographic data, *Tectonophysics*, **363**(1-2), 79–102.

Olsen, K. B., Day, S. M., Dalguer, L. A., Mayhew, J., Cui, Y., Zhu, J., Cruz-Atienza, V. M., Roten, D., Maechling, P., Jordan, T. H., Okaya, D., & Chourasia, A., 2009. ShakeOut-D: Ground motion estimates using an ensemble of large earthquakes on the southern San Andreas fault with spontaneous rupture propagation, *Geophysical Research Letters*, **36**(4), L04303.

Palmer, A. C. & Rice, J. R., 1973. The growth of slip surfaces in the progressive failure of over-consolidated clay, *Proceedings of the Royal Society of London*, **A 332**, 527–548.

Pelties, C., de la Puente, J., Ampuero, J.-P., Brietzke, G. B., & Käser, M., 2012. Three-dimensional dynamic rupture simulation with a high-order discontinuous Galerkin method on unstructured tetrahedral meshes, *Journal of Geophysical Research*, **117**(B2), B02309.

Peter, D., Komatitsch, D., Luo, Y., Martin, R., Le Goff, N., Casarotti, E., Le Loher, P., Magnoni, F., Liu, Q., Blitz, C., Nissen-Meyer, T., Basini, P., & Tromp, J., 2011. Forward and adjoint simulations of seismic wave propagation on fully unstructured hexahedral meshes, *Geophysical Journal International*, **186**(2), 721–739.

Pitarka, A., Dalguer, L. A., Day, S. M., Somerville, P. G., & Dan, K., 2009. Numerical Study of Ground-Motion Differences between Buried-Rupturing and Surface-Rupturing Earthquakes, *Bulletin of the Seismological Society of America*, **99**(3), 1521–1537.

Sato, M., Ishikawa, T., Ujihara, N., Yoshida, S., Fujita, M., Mochizuki, M., & Asada, A., 2011. Displacement Above the Hypocenter of the 2011 Tohoku-Oki Earthquake, *Science*, **332**(6036), 1395–1395.

Simons, M., Minson, S. E., Sladen, A., Ortega, F., Jiang, J., Owen, S. E., Meng, L., Ampuero, J. P., Wei, S., Chu, R., Helmberger, D. V., Kanamori, H., Hetland, E., Moore, A. W., & Webb, F. H., 2011. The 2011 Magnitude 9.0 Tohoku-Oki Earthquake: Mosaicking the Megathrust from Seconds to Centuries, *Science*, **332**(6036), 1421–1425.

Suzuki, W., Aoi, S., Sekiguchi, H., & Kunugi, T., 2011. Rupture process of the 2011 Tohoku-Oki mega-thrust earthquake (M9.0) inverted from strong-motion data, *Geophysical Research Letters*, **38**(7).

Tago, J., Cruz-Atienza, V. M., Virieux, J., Etienne, V., & Sánchez-Sesma, F. J., 2012. A 3D hp-adaptive discontinuous Galerkin method for modeling earthquake dynamics, *Journal of Geophysical Research*, **117**(B9), B09312.

Yagi, Y. & Fukahata, Y., 2011. Rupture process of the 2011 Tohoku-oki earthquake and absolute elastic strain release, *Geophysical Research Letters*, **38**(19).

Yagi, Y., Nakao, A., & Kasahara, A., 2012. Smooth and rapid slip near the Japan Trench during the 2011 Tohoku-oki earthquake revealed by a hybrid back-projection method, *Earth and Planetary Science Letters*, **355-356**(c), 94–101.

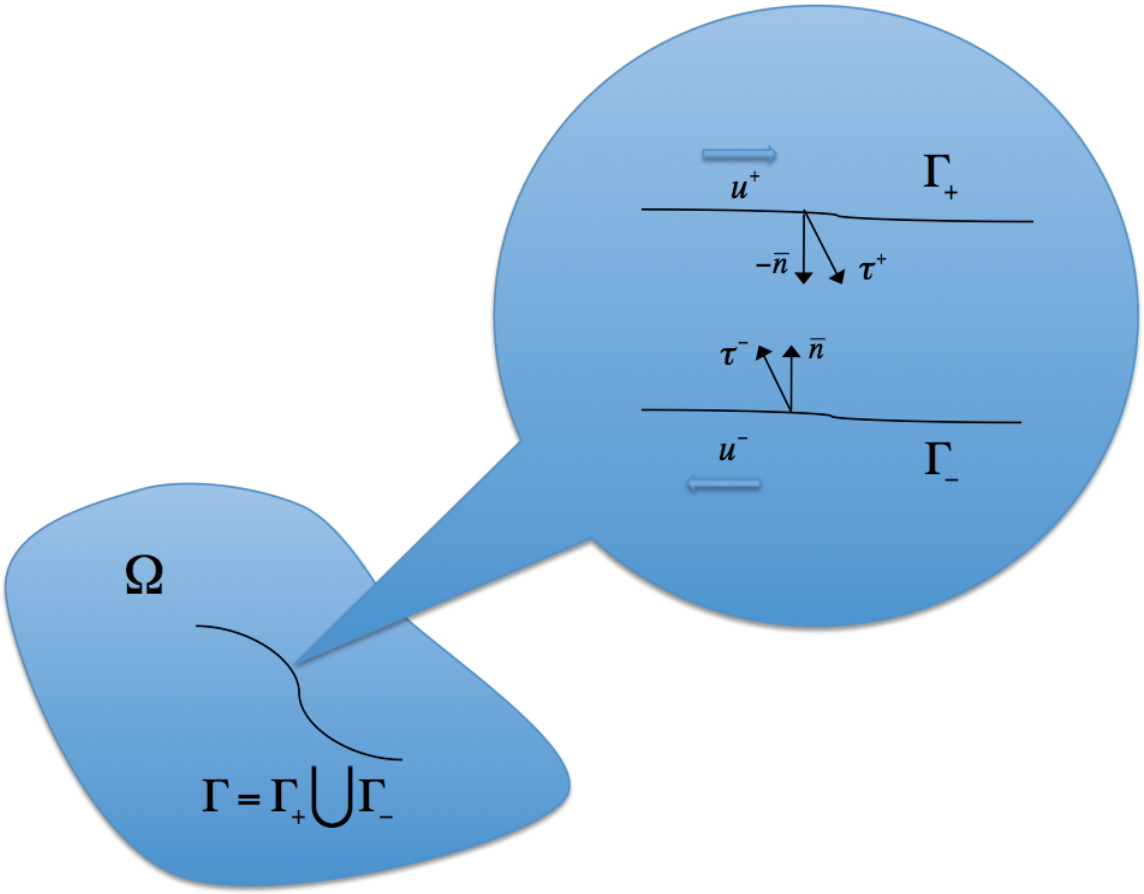

Figure 1. Representation of a fault as two split surfaces. The fault interface, Γ, is embedded in an elastic medium, Ω, and is composed by two matching surfaces, $\Gamma_\pm$, that can deform independently. For clarity, the two surfaces are plotted as separated in the zommed in view, although they are most tipically considered to be in frictional contact. The vector normal to the surface Γ_-, pointing towards Γ_+, is denoted by $\bar{n}$. On each side of the fault tractions are denoted by $\tau^\pm$ and displacements by $u^\pm$.

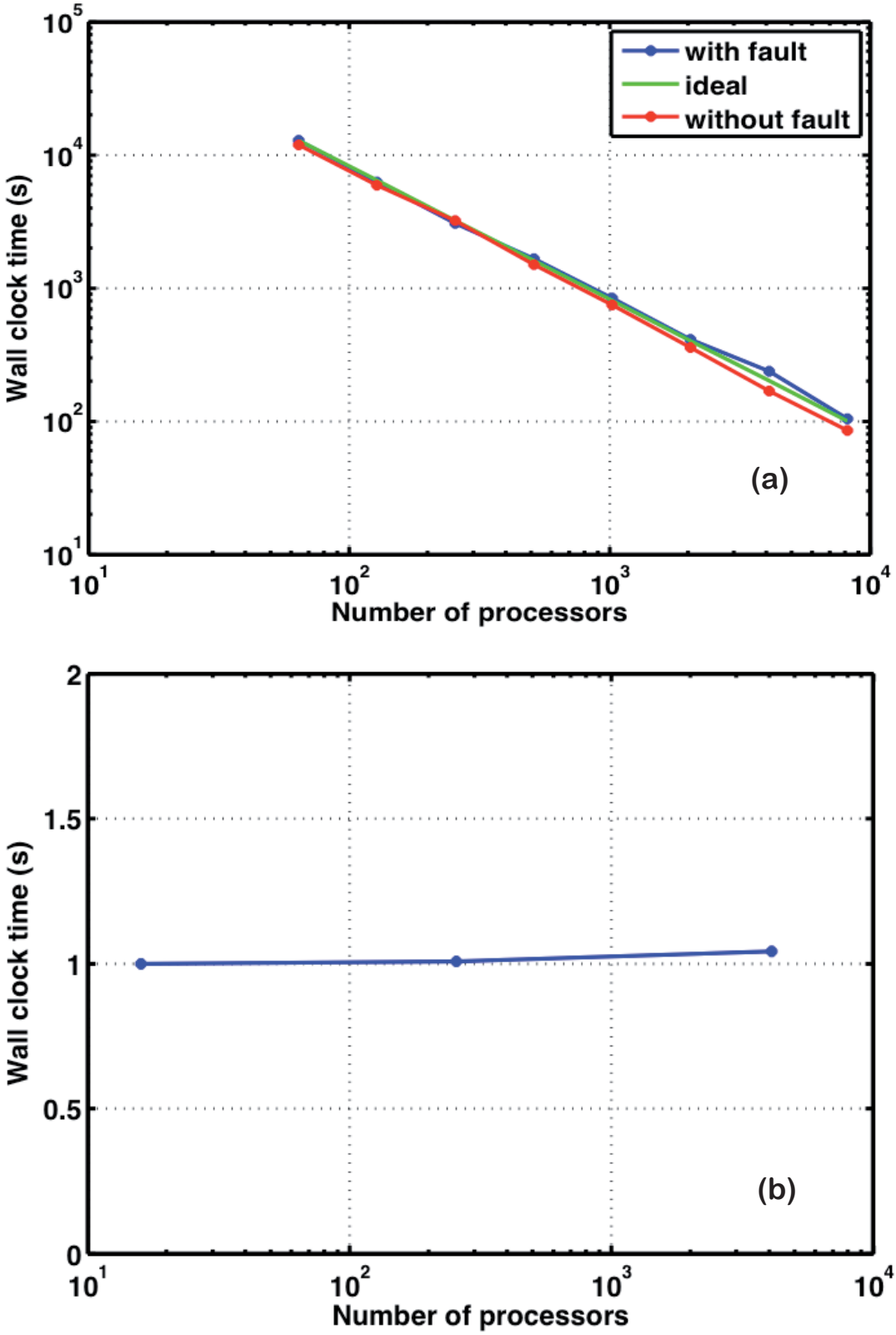

Figure 2. (a) Results of strong scalability of SPECFEM3D with and without our fault implementation on CSCS's Cray XE6 system (Rosa), up to 8192 processors. The tests are based on the SCEC TPV5 benchmark problem. (b) Weak scalability of SPECFEM3D with our fault implementation on CSCS's Cray XE6 system (Rosa). The tests are based on the TPV205 benchmark with 50, 100 and 200 m average grid spacing.

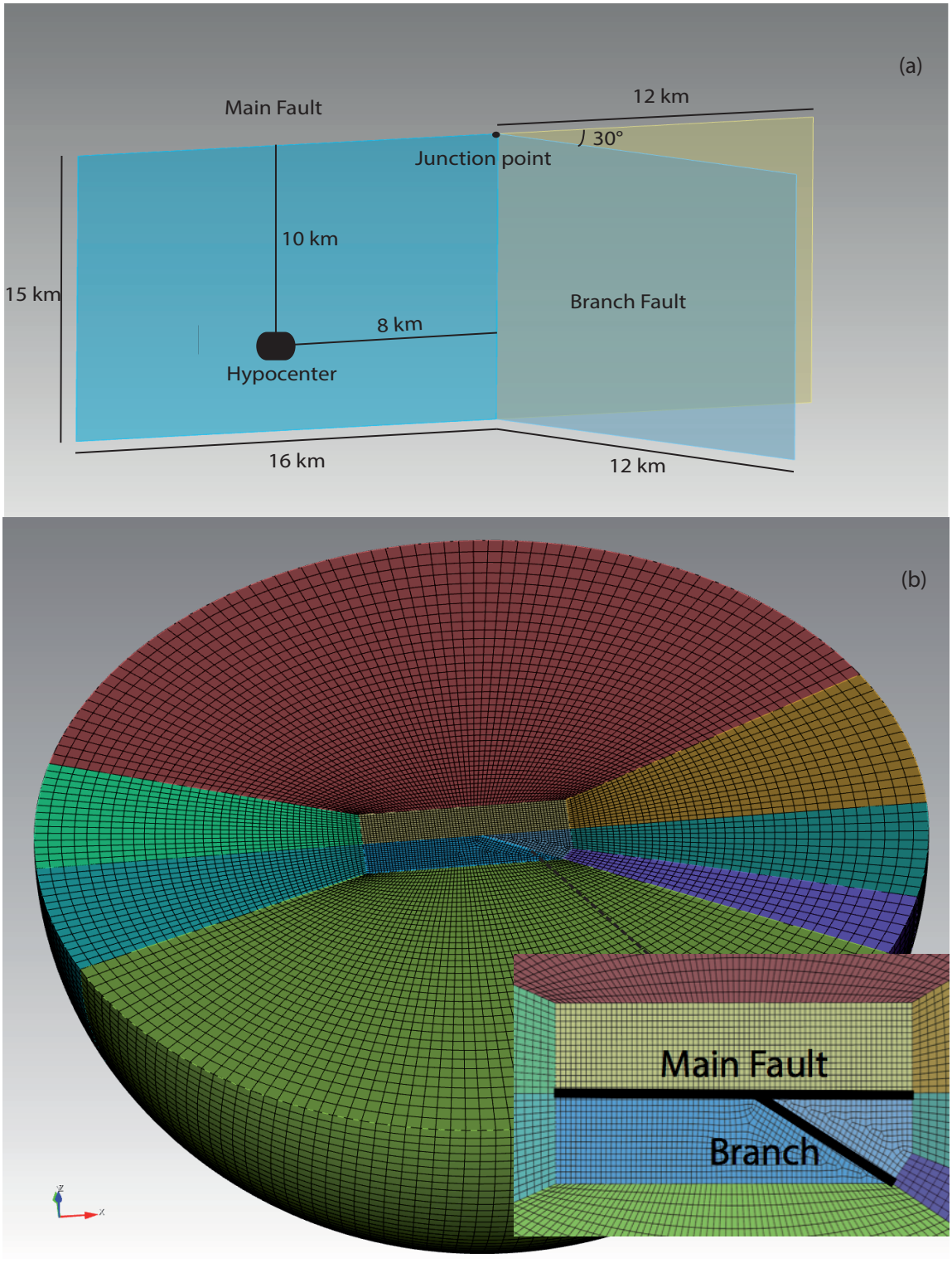

Figure 3. (a) Sketch of the fault branching benchmark problems TPV24 and TPV25 of the SCEC/USGS dynamic rupture code verification exercise. The main fault and its branch are vertical-planar strike-slip faults that reach the surface. The nucleation zone is located on the main fault (thick black symbol). (b) A semi-spherical unstructured spectral element mesh for the TPV24 and TPV25 problems, with progressive mesh coarsening away from the fault zone. The inset shows a detailed map view on the fault domain.

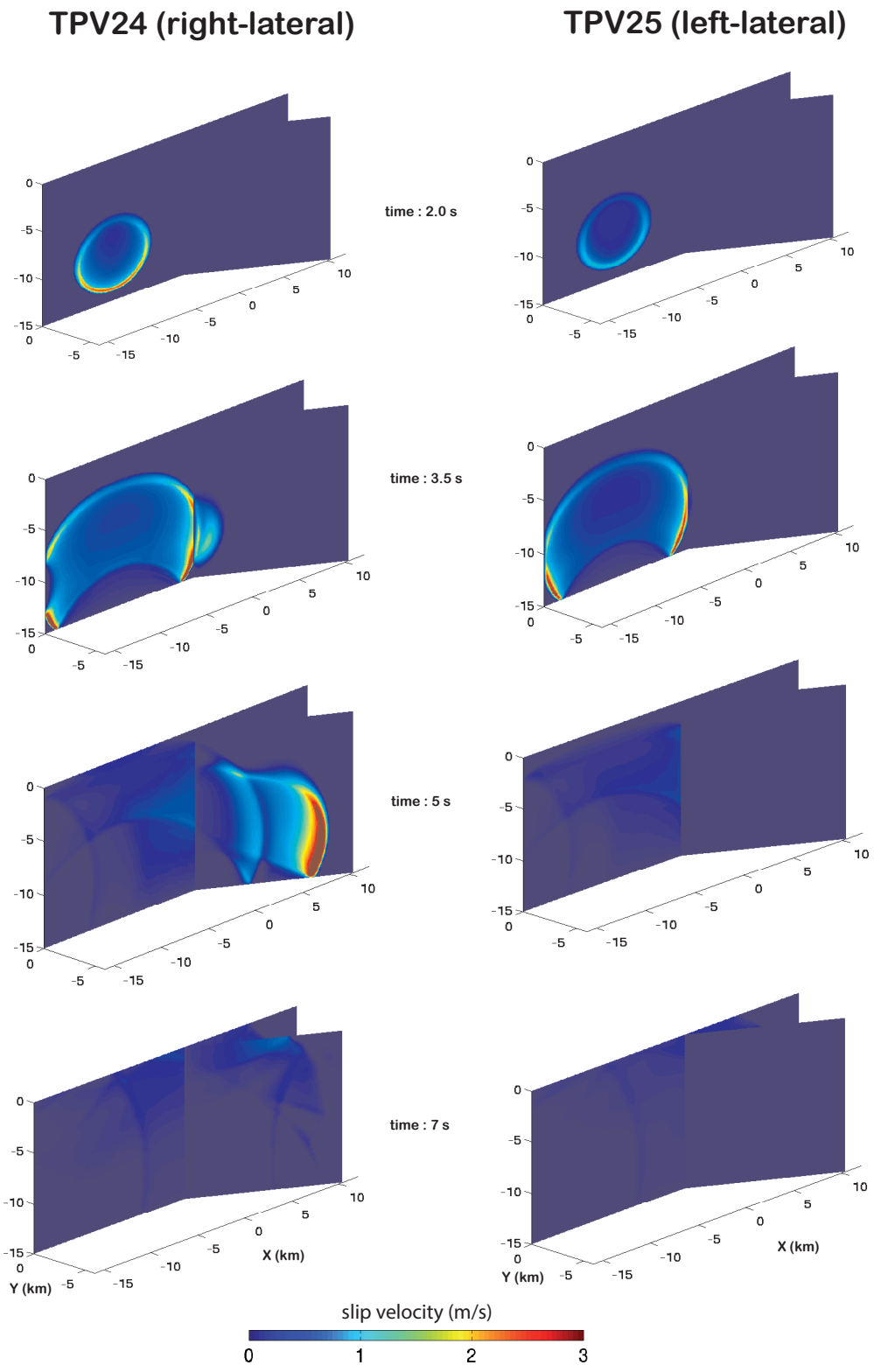

Figure 4. Snapshots of slip velocity in the benchmark problems TPV24 (a) and TPV25 (b), computed with the spectral element code SPECFEM3D on an unstructured mesh. Significant rupture on the fault branch occurs only in the righ-lateral case (TPV24).

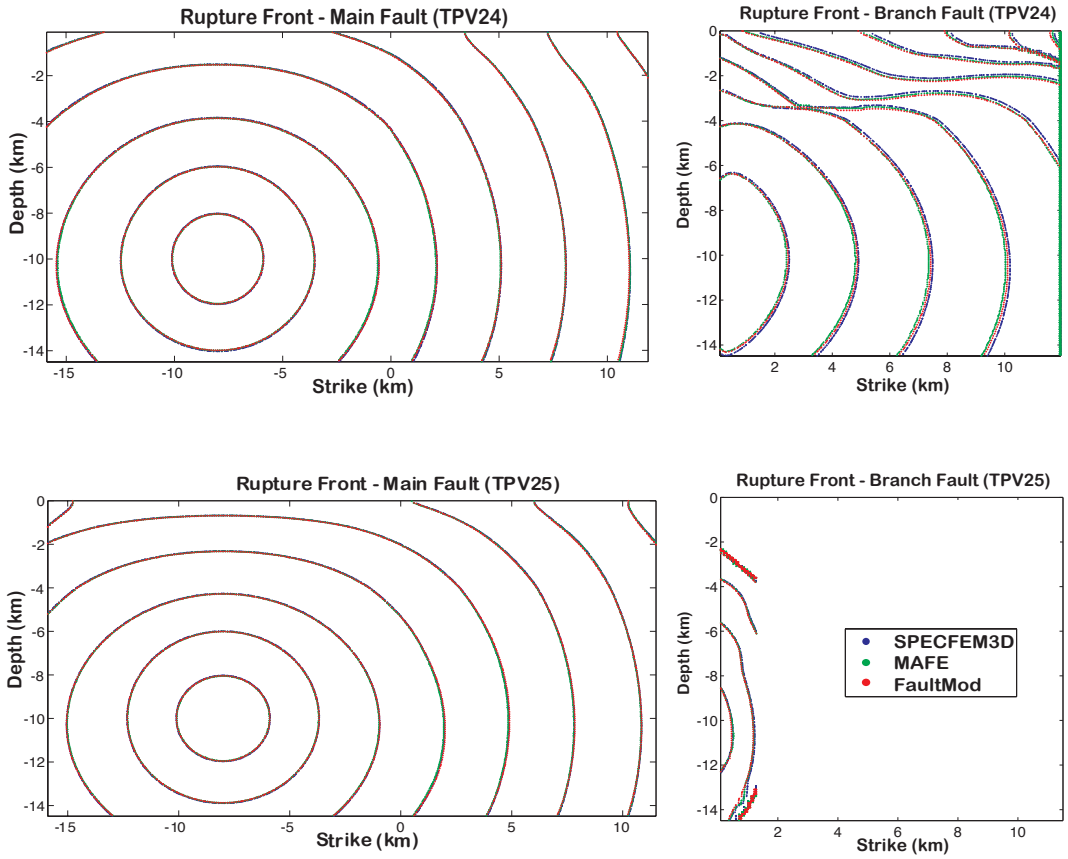

Figure 5. Comparison of rupture times in the benchmark problems TPV24 and TPV25 obtained by the unstructured spectral element code SPECFEM3D and the finite element codes MAFE Ma & Liu (2006) and FaultMod Barall (2009).

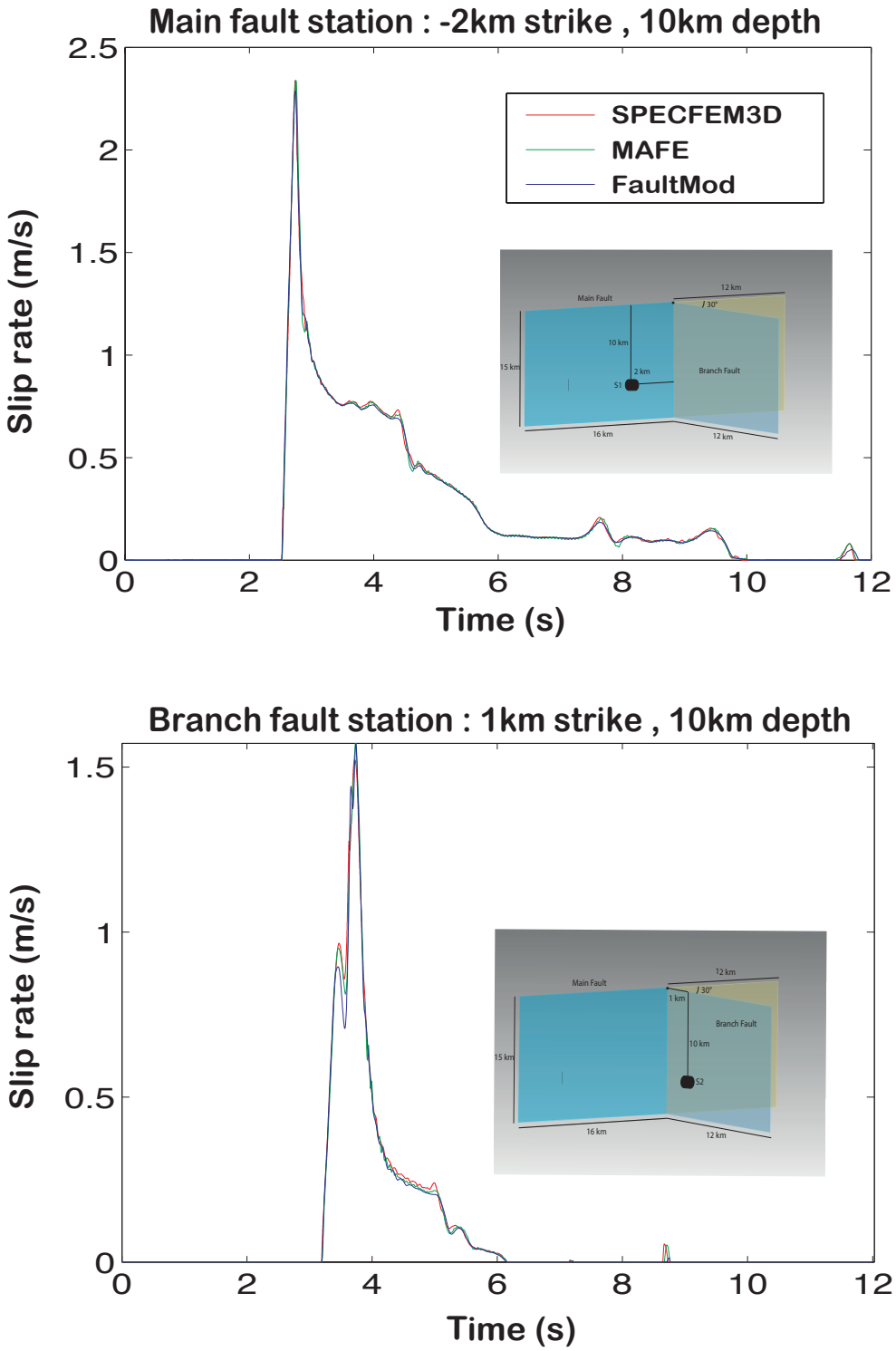

Figure 6. Comparison of slip rate time series in the benchmark problem TPV24 computed by SPECFEM3D, MAFE and FaultMod at two locations, on the main fault and on the fault branch, respectively (see locations in the insets).

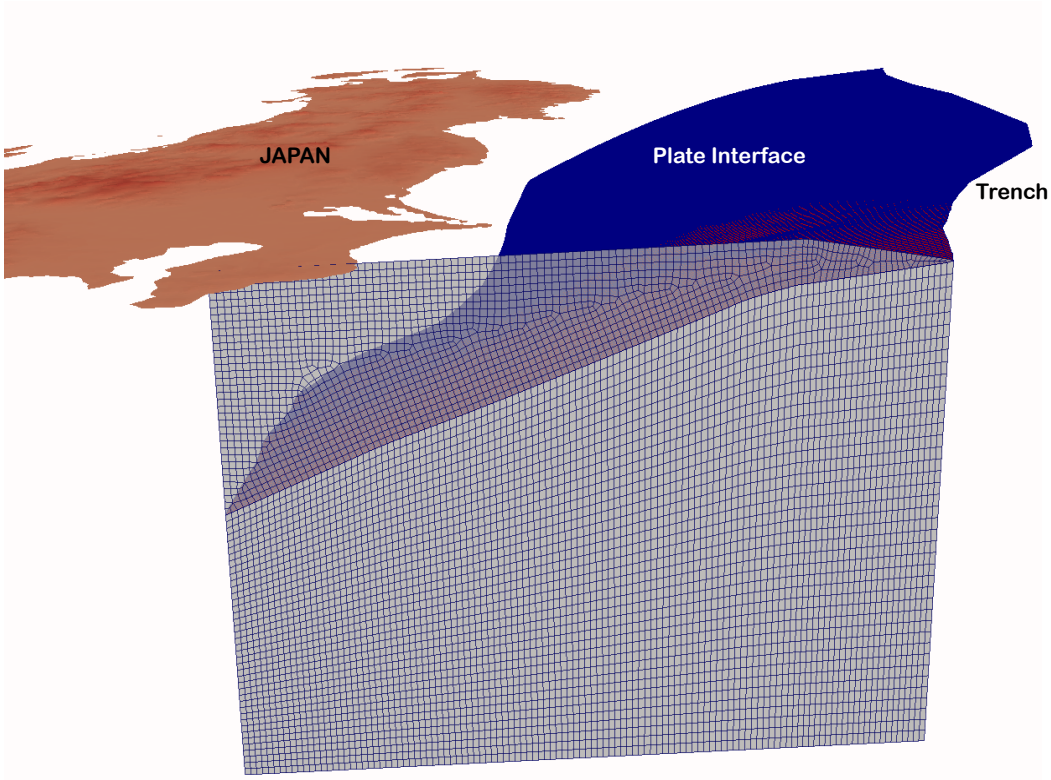

Figure 7. Non-planar geometry of the Japanese subduction megathrust in the Tohoku region (blue surface) and a cross-section of the unstructured spectral element mesh.

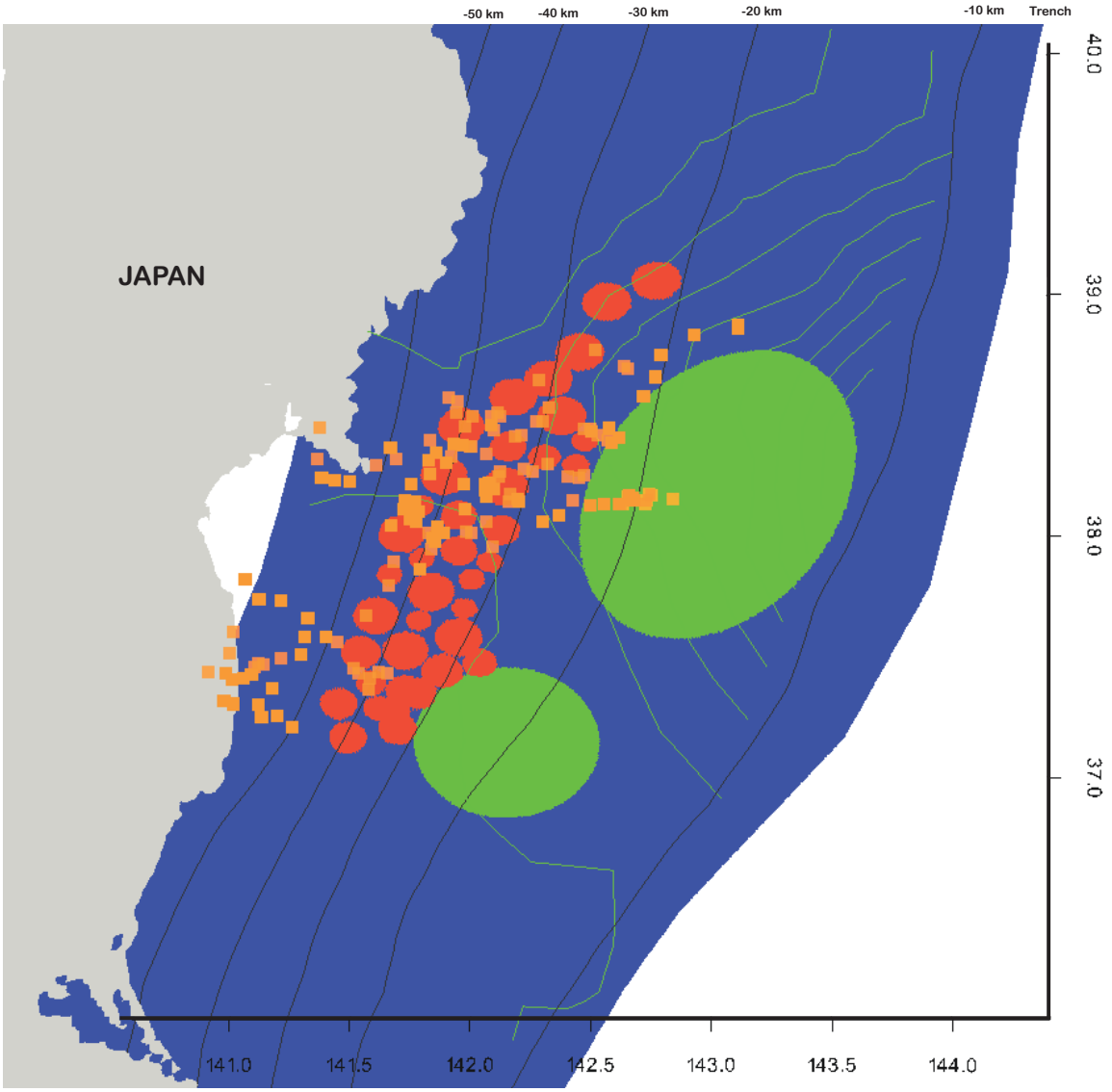

Figure 8. Distribution of asperities in our dynamic model of the Tohoku earthquake (green ellipse and red circles). Also shown are depth contours of the megathrust interface (black curves), contours of coseismic slip obtained by Suzuki et al. (2011) through kinematic source inversion (green curves) and locations of high frequency radiation obtained by Meng et al. (2011) through teleseismic back-projection (orange squares).

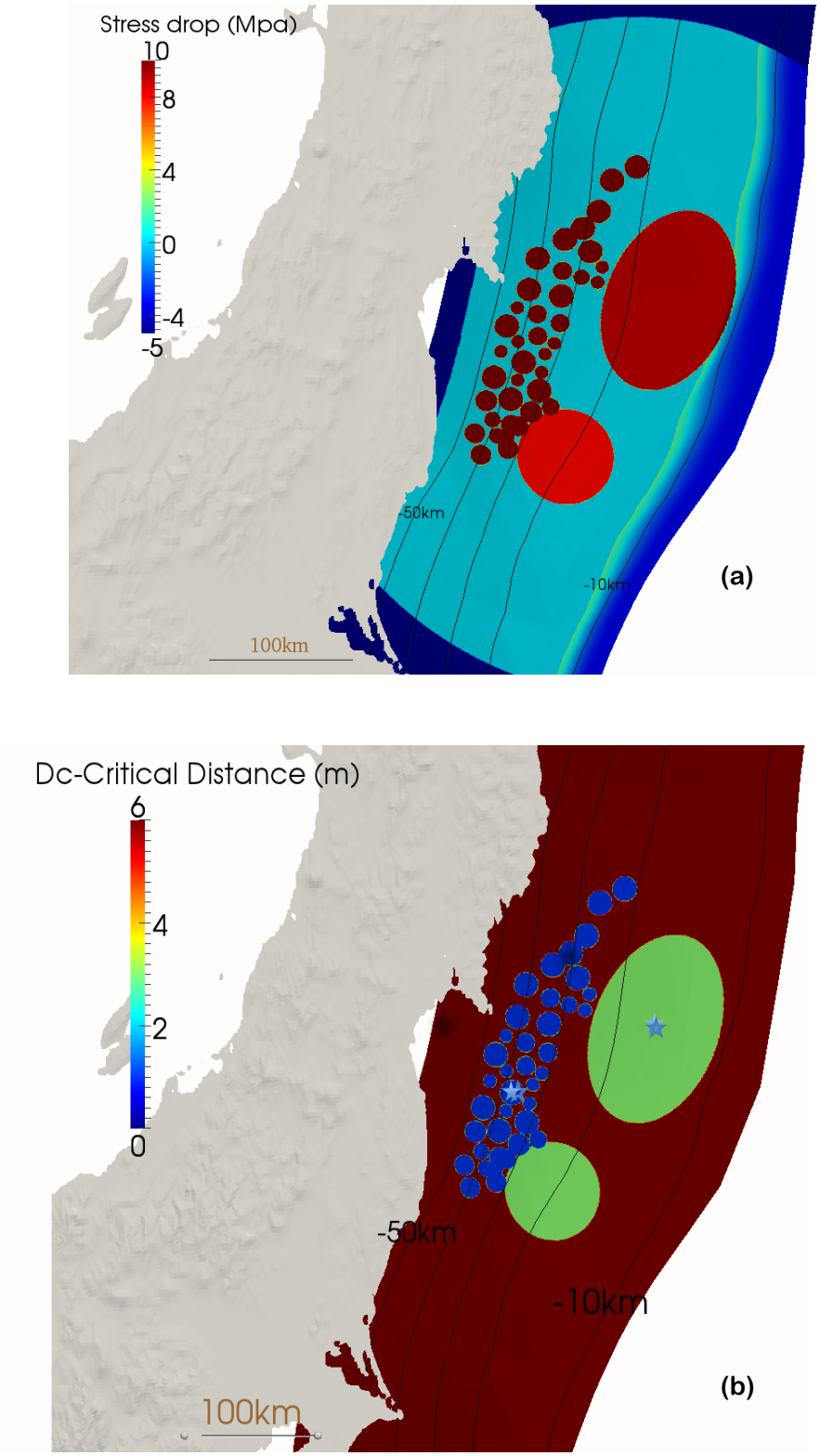

Figure 9. Distribution of (a) stress drop along the fault and (b) slip-weakening distance D_c on the plate interface.

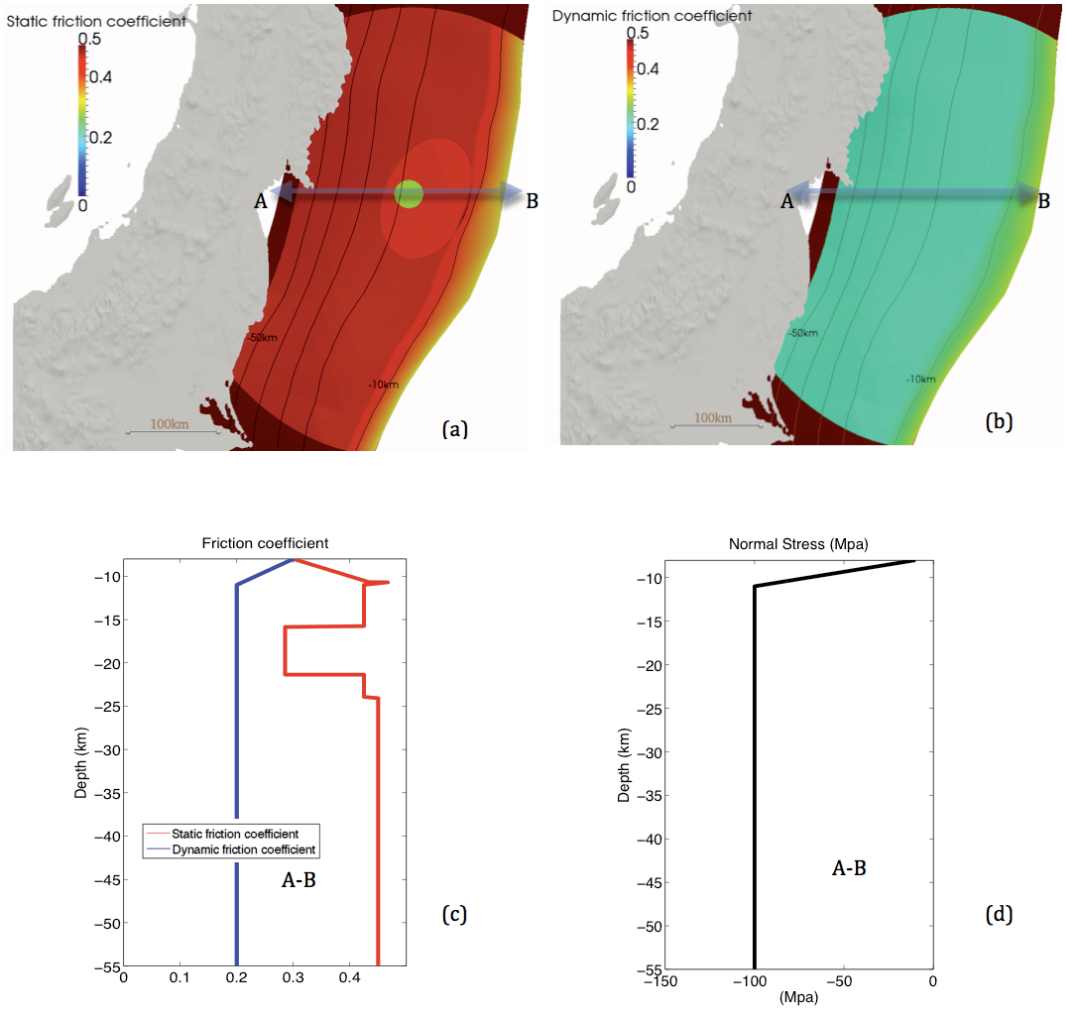

Figure 10. Distribution of friction and normal stress in our dynamic model of the Tohoku earthquake. (a) Static and (b) dynamic friction coefficients on the fault surface. (c) Friction coefficients and (d) normal stress as a function of depth along a profile A-B passing through the hypocenter (shown in a-b).

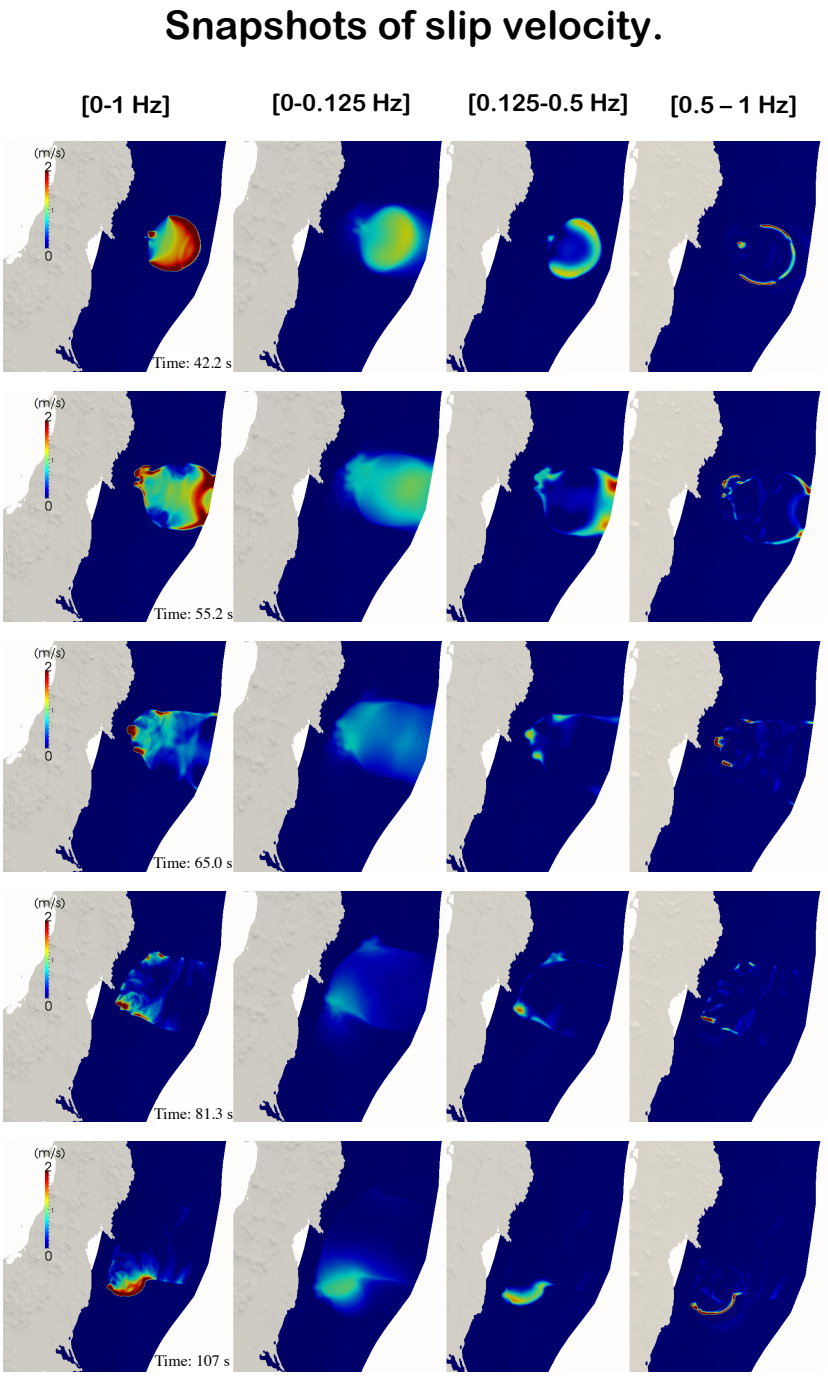

Figure 11. Evolution of slip velocity in our dynamic model of the Tohoku earthquake. Each line corresponds to a time indicated on the left column. Each column corresponds to a different frequency band: 0-1 Hz, 0-0.125 Hz, 0.125-0.5 Hz and 0.5-1 Hz.

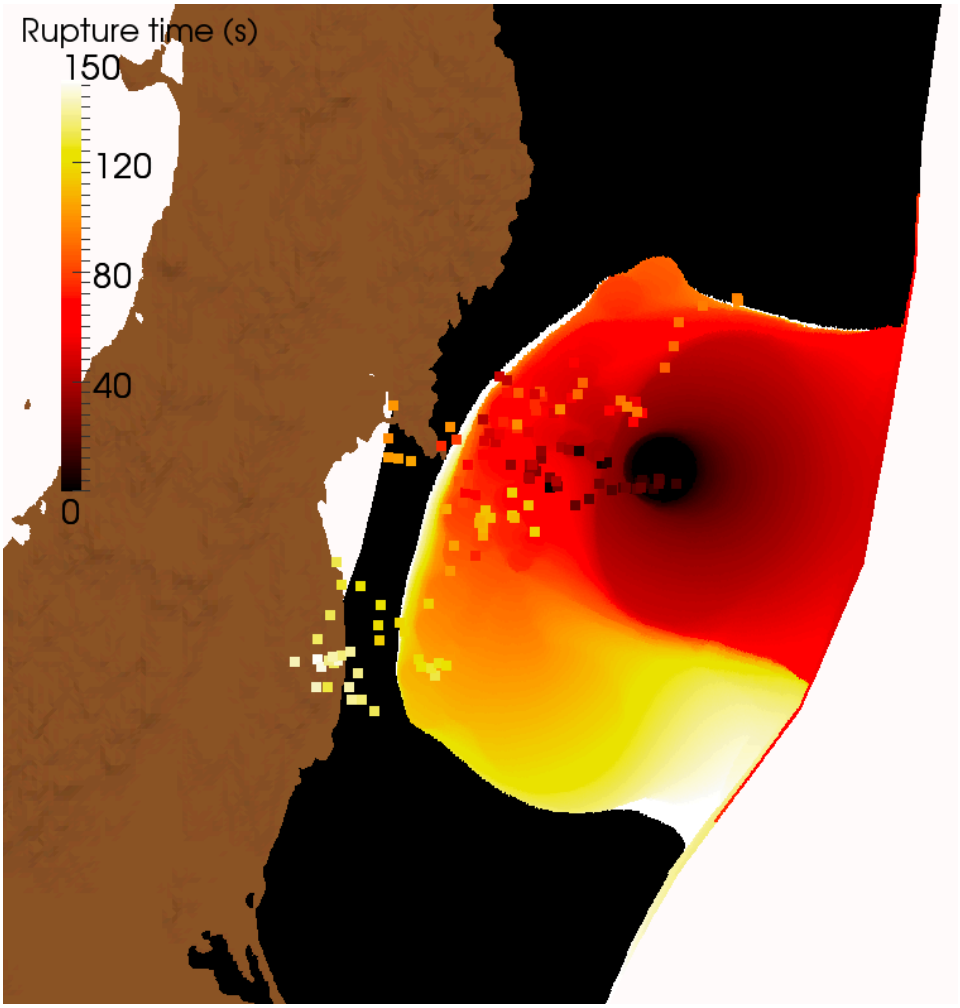

Figure 12. Distribution of rupture times in our dynamic rupture model of the Tohoku earthquake. The squares are the locations of high frequency radiation (1 Hz) imaged by teleseismic back-projection by Meng et al. (2011), color-coded by their timing (see color bar).

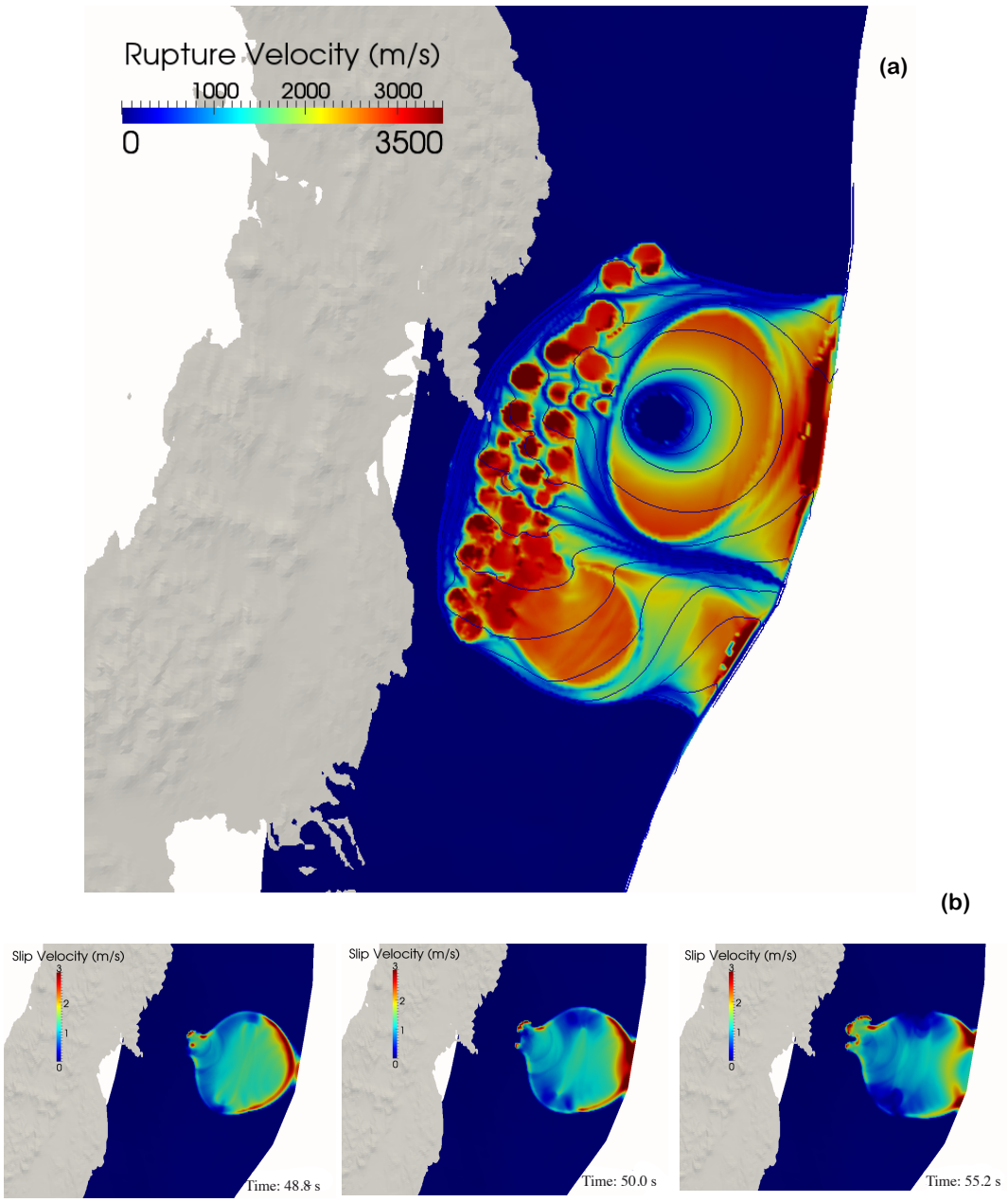

Figure 13. (a) Distribution of rupture velocity and contours of rupture time in our dynamic rupture model of the Tohoku earthquake. (b) Snapshots of slip rate showing the emergence of a secondary front at the trench, its coalescence with the main rupture front, and the emergence of supershear rupture near the trench.

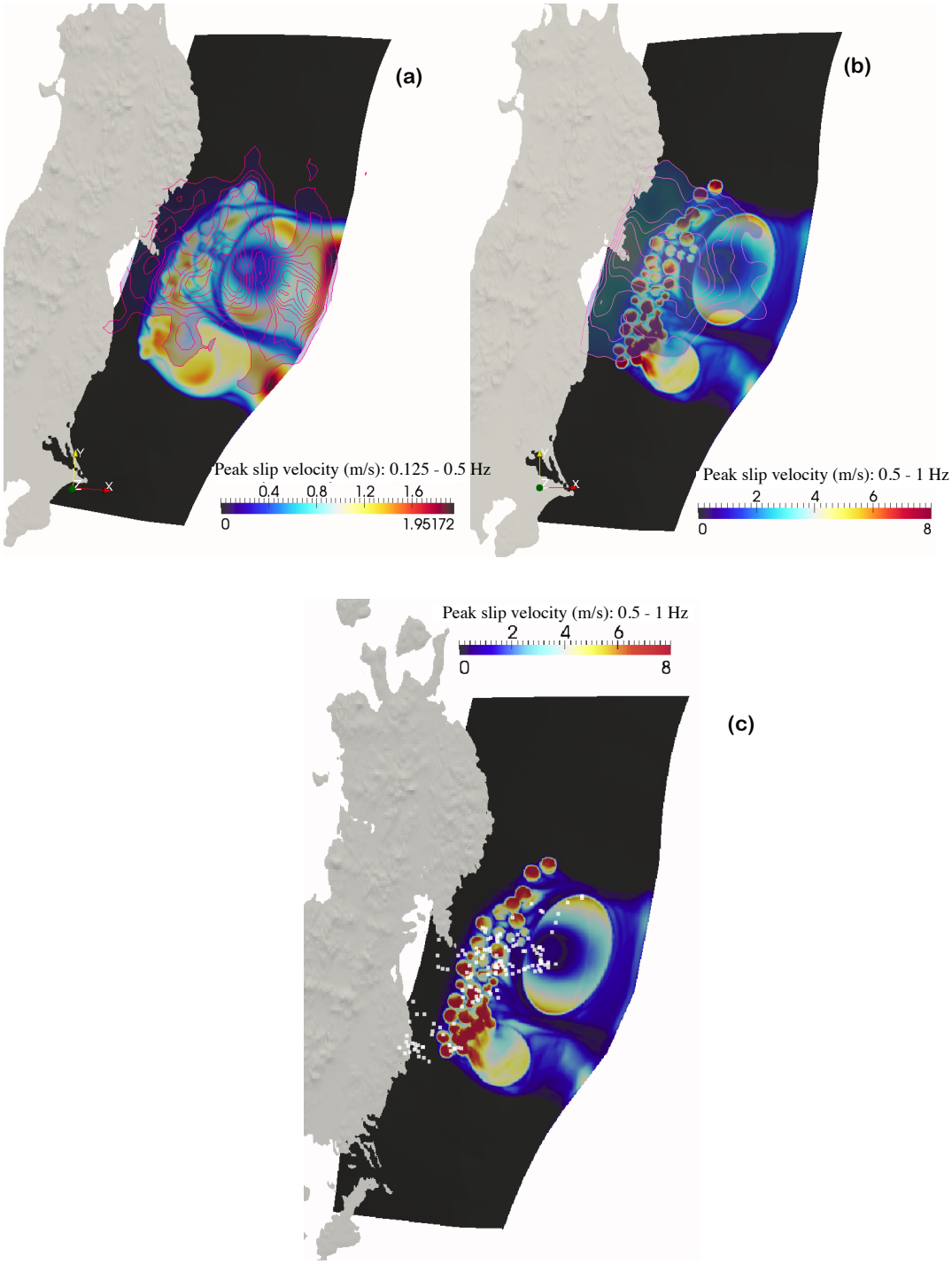

Figure 14. Distribution of peak slip velocity of our dynamic rupture model of the Tohoku earthquake in two frequency bands, (a) 0.125-0.5 Hz and (b) 0.5-1 Hz, compared to energy release in these bands (blue contours) estimated by hybrid back-projection by Yagi et al. (2012). (c) Locations of high frequency radiation (white dots) imaged by back-projection by Meng et al. (2011) overlain on our peak slip velocity in the 0.5-1 Hz band.

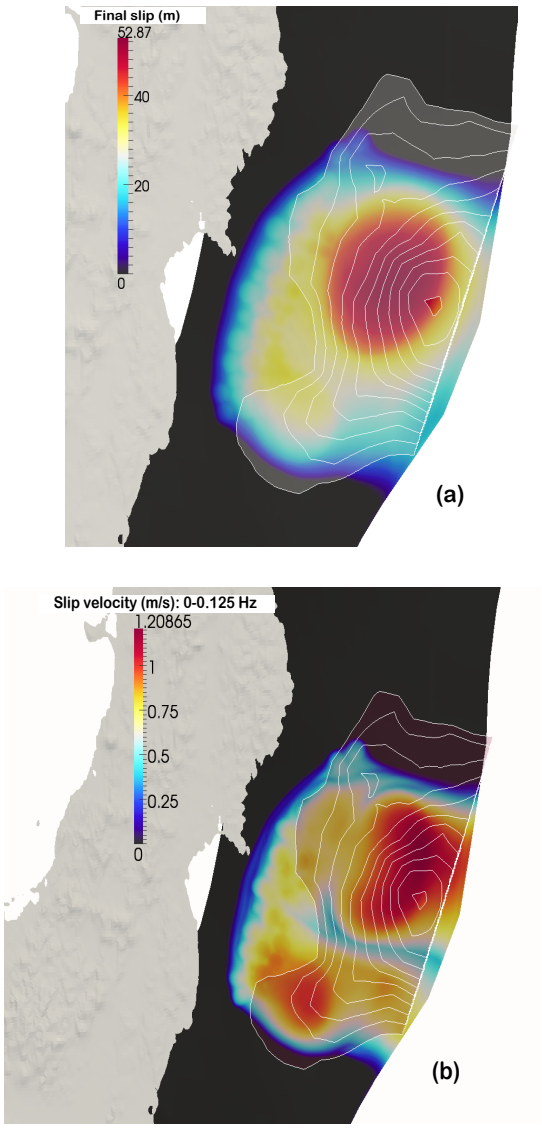

Figure 15. (a) Final slip and (b) peak slip rate in the 0-0.125 Hz band of our dynamic rupture model of the Tohoku earthquake, and slip in the kinematic source model of Yagi & Fukahata (2011) (white contours).

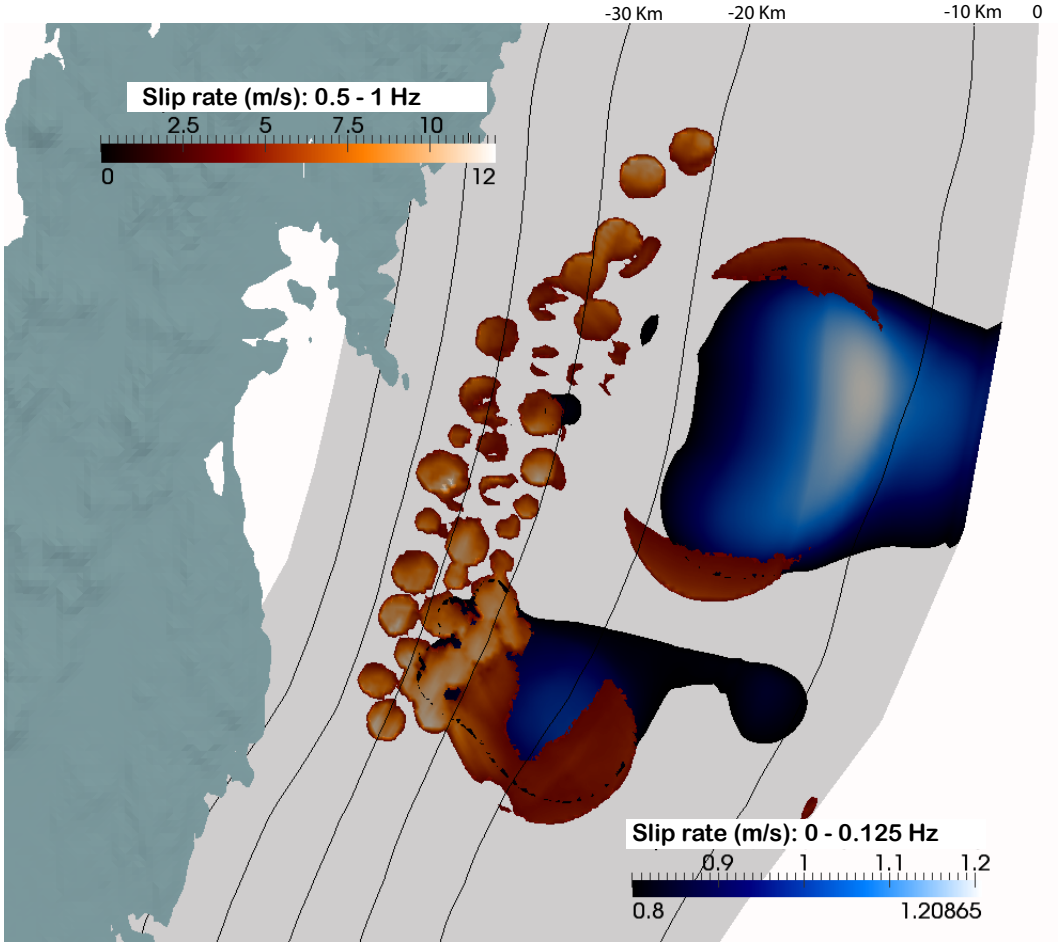

Figure 16. Peak slip rate in the 0-0.125 Hz and 0.5-1 Hz bands in our dynamic rupture model of the Tohoku earthquake.

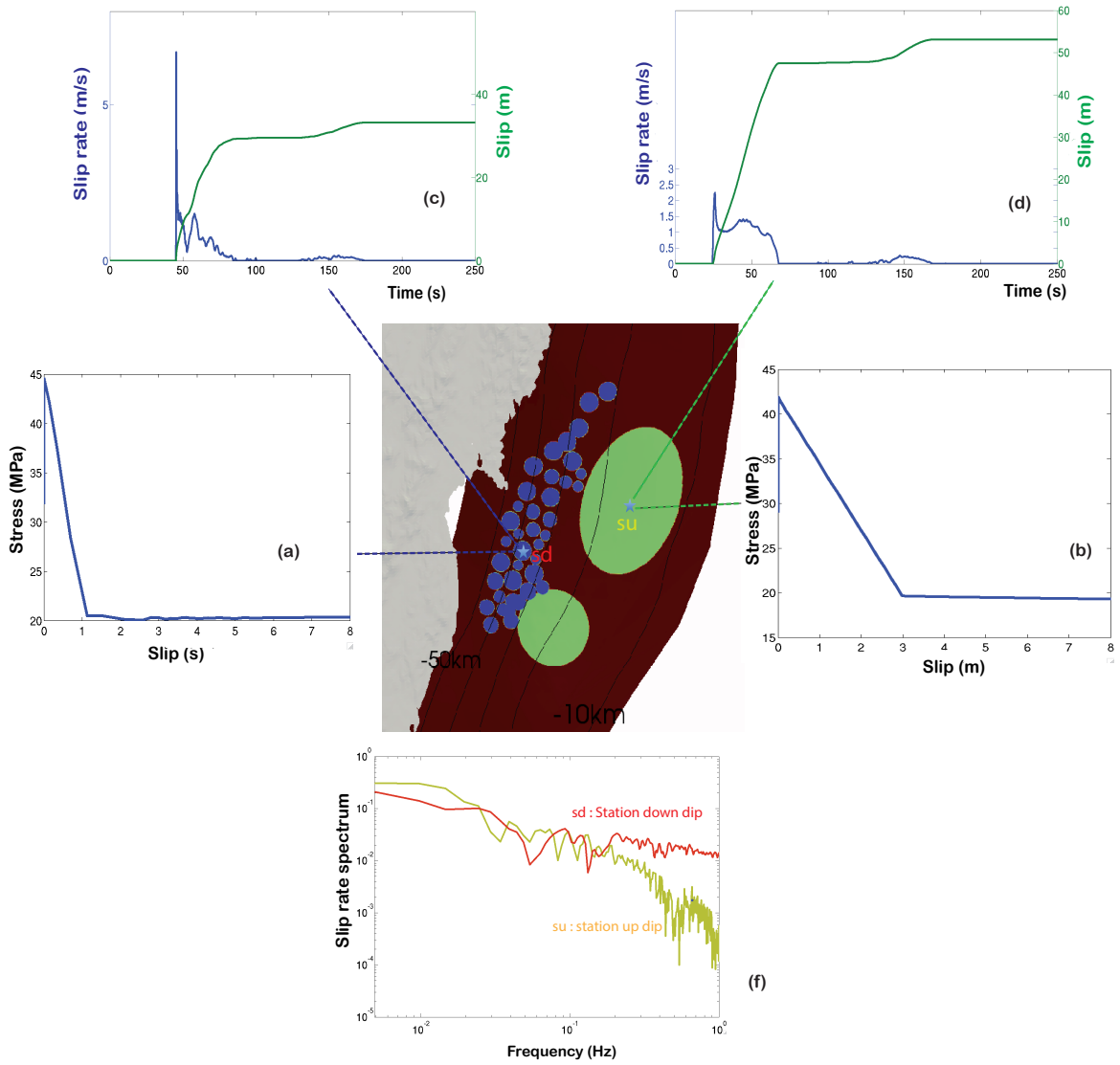

Figure 17. (a) y (b) Stress versus slip, (c) y (d) time series of slip rate and slip and (e) spectra of slip rate at two fault locations (blue stars): inside a deep asperity (sd) and in the middle of the largest asperity (su).

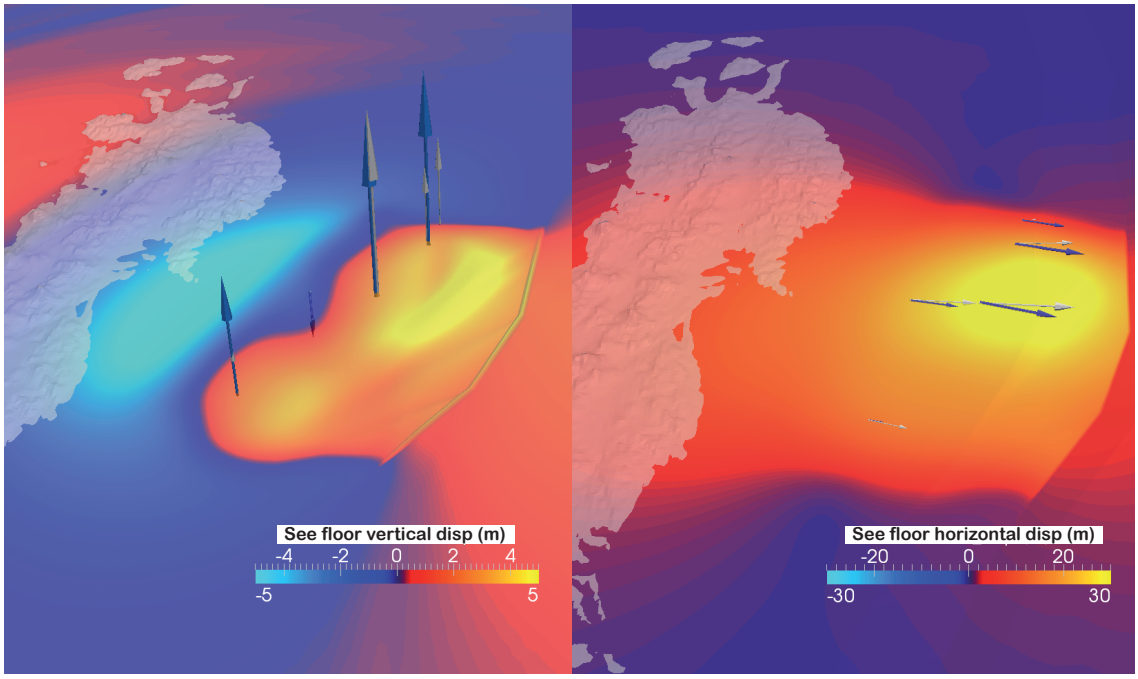

Figure 18. (a) Vertical and (b) horizontal seafloor displacement in our dynamic rupture model of the Tohoku earthquake (colors and white arrows) and from ocean bottom geodetic observations (blue arrows).

Appendix C. Spatial distribution of final slip and peak slip velocity of simulated earthquakes computed with the dynamic code SPECFEM3D based on initial conditions obtained with the quasi-dynamic code QDYN.

File_ID Magnitude Duration
19 8.32 155

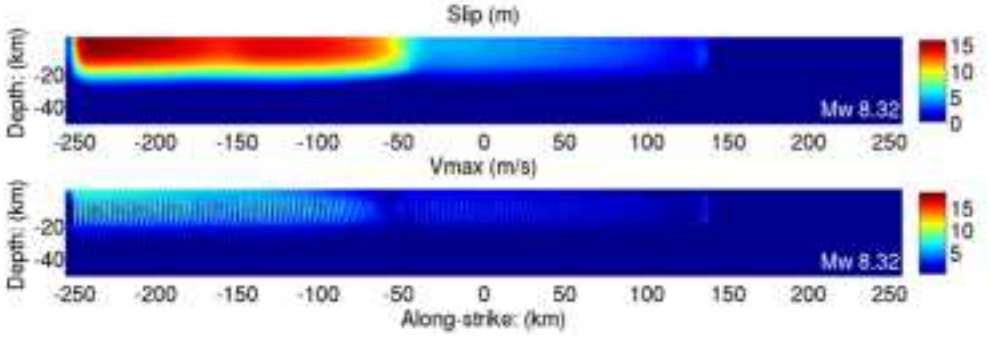

File_ID Magnitude Duration
8 8.26 161

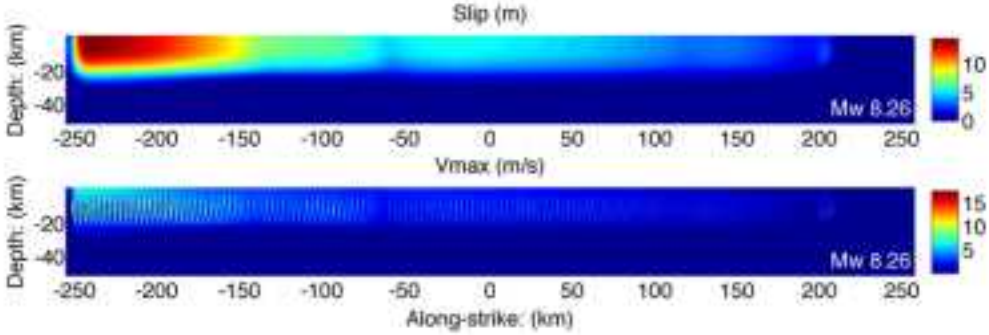

File_ID Magnitude Duration
7 8.26 159

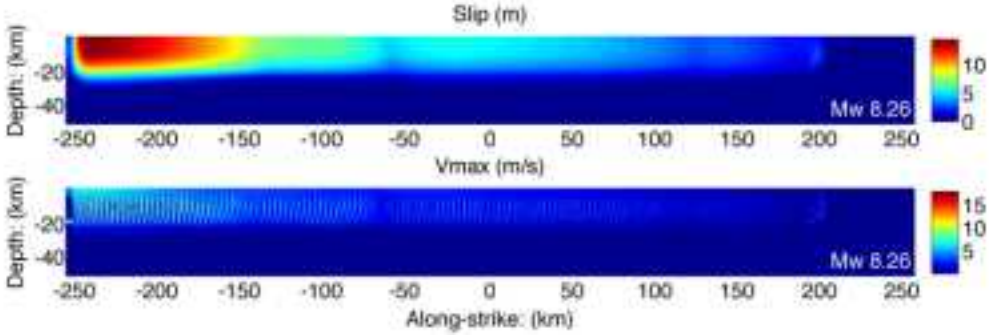

File_ID Magnitude Duration
6 8.26 160

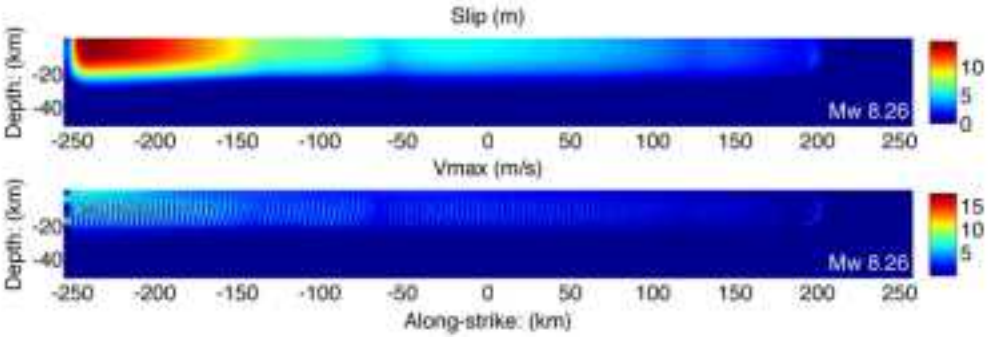

File_ID Magnitude Duration
5 8.25 150

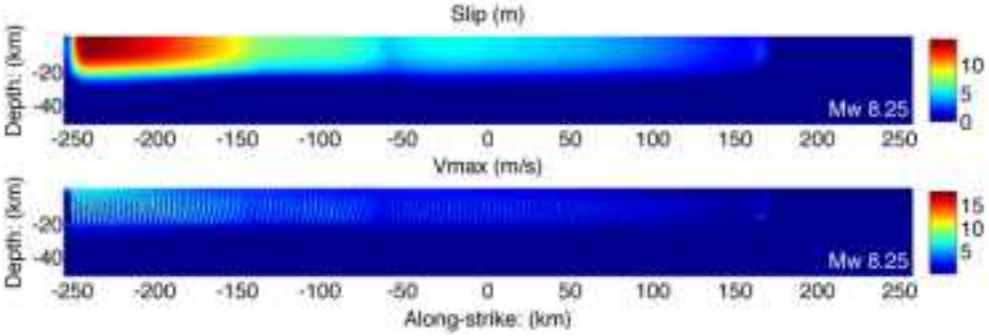

File_ID Magnitude Duration
4 8.24 149

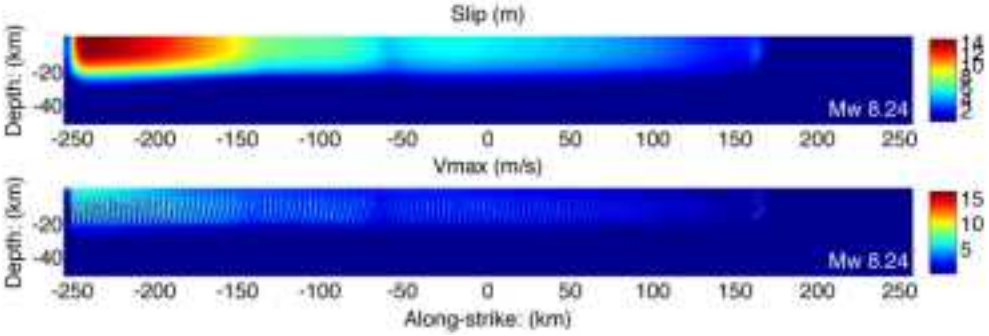

File_ID Magnitude Duration
2 8.24 148

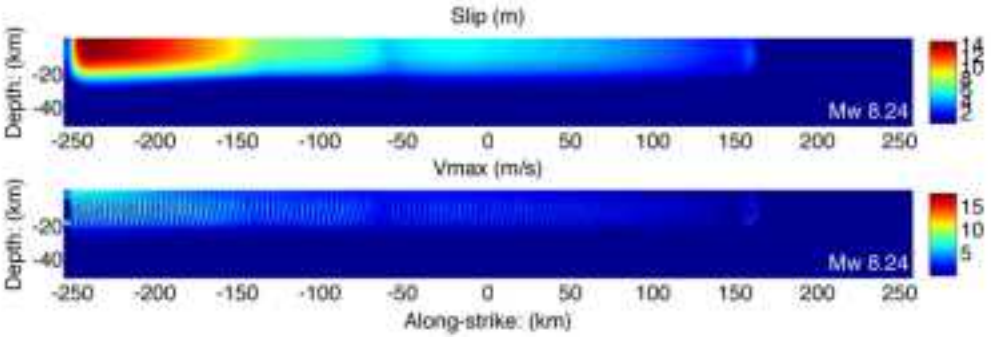

File_ID Magnitude Duration
3 8.24 149

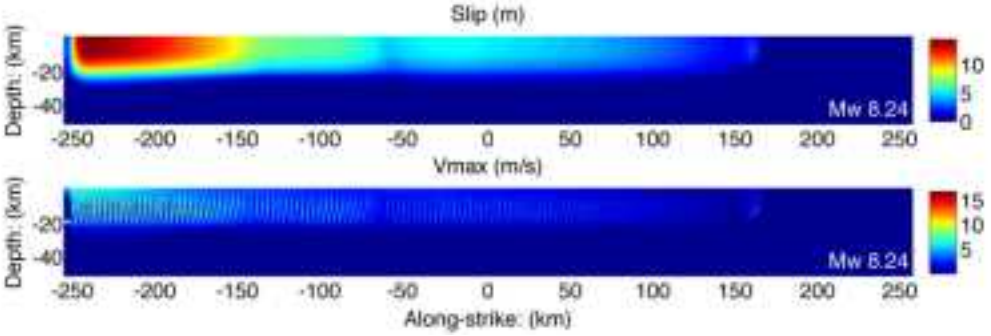

File_ID Magnitude Duration
1 8.24 147

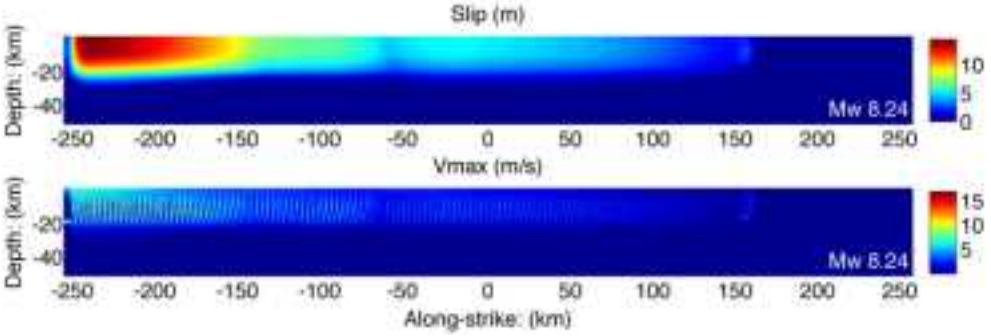

File_ID Magnitude Duration
20 8.04 99

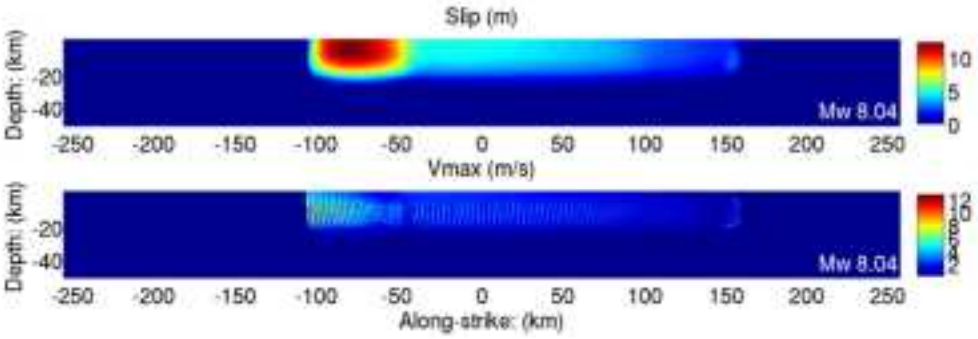

File_ID Magnitude Duration
18 7.82 74

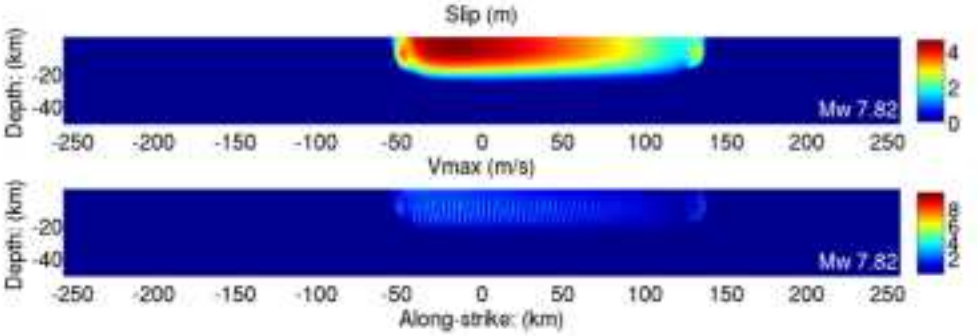

File_ID Magnitude Duration
27 7.80 69

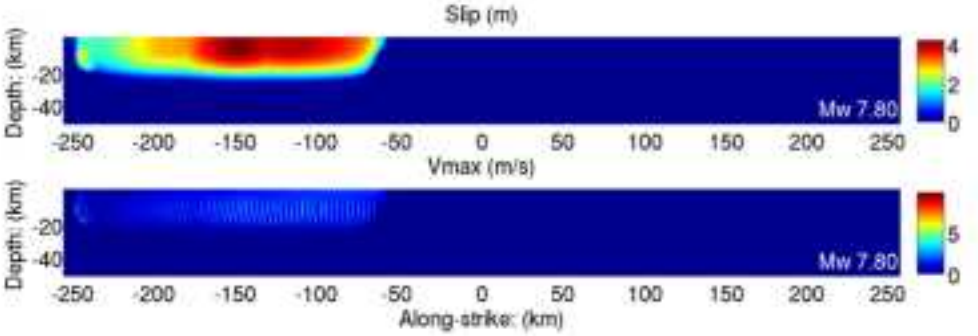

File_ID Magnitude Duration
26 7.79 69

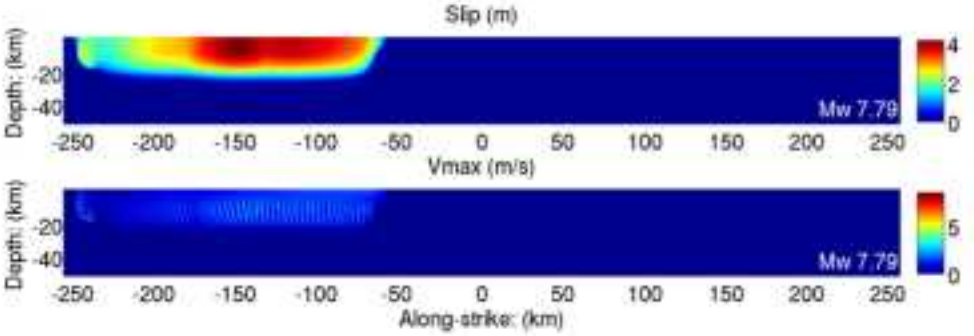

File_ID Magnitude Duration
46 7.75 63

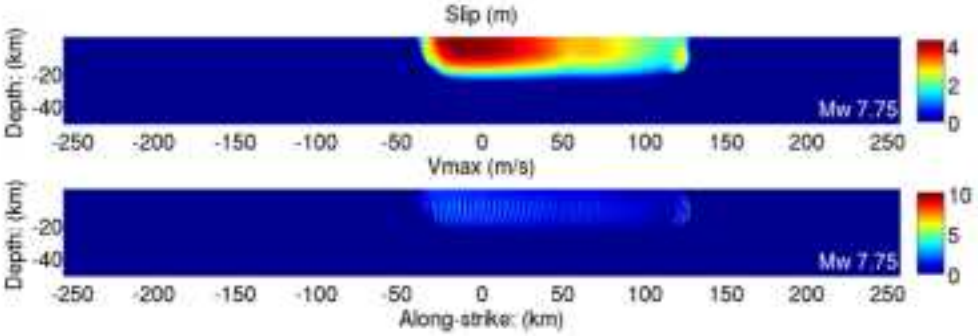

File_ID Magnitude Duration
68 7.68 52

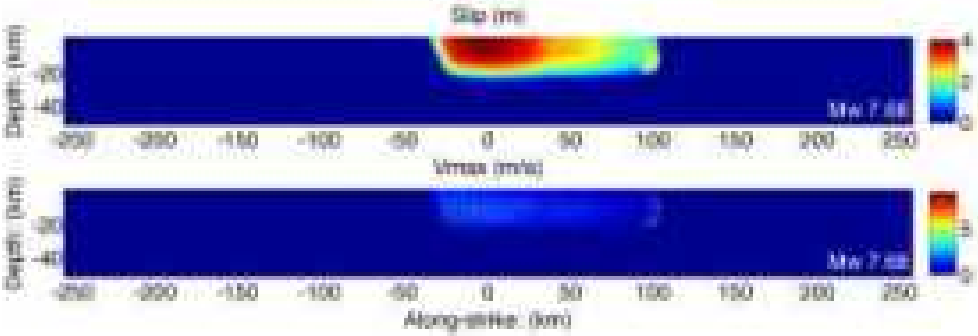

File_ID Magnitude Duration
88 7.68 52

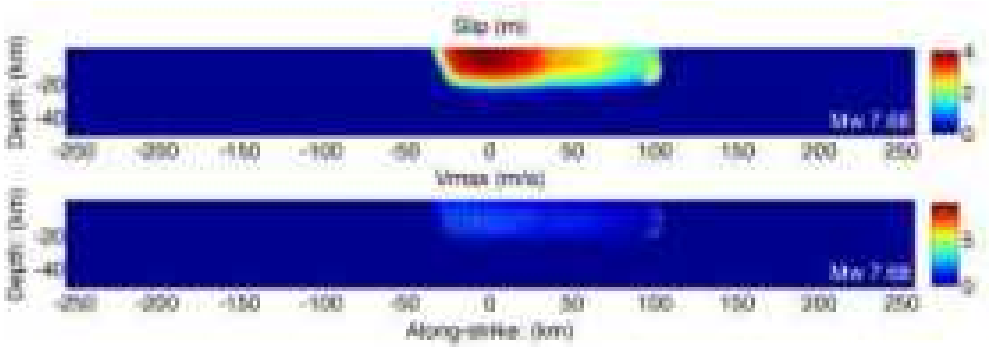

File_ID Magnitude Duration
81 7.67 53

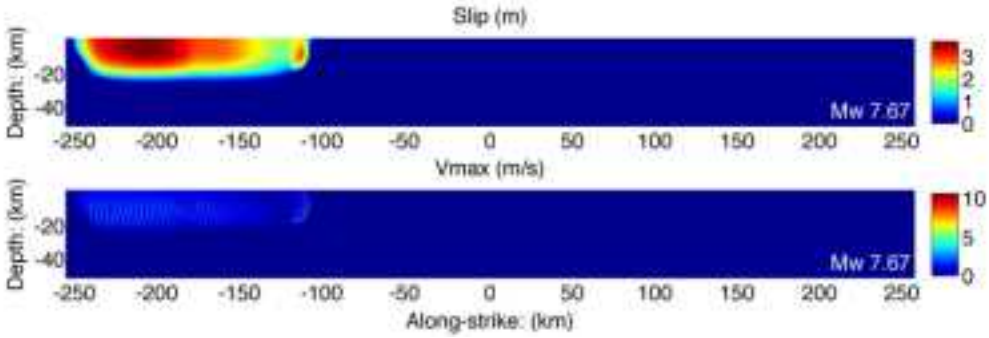

File_ID Magnitude Duration
80 7.66 53

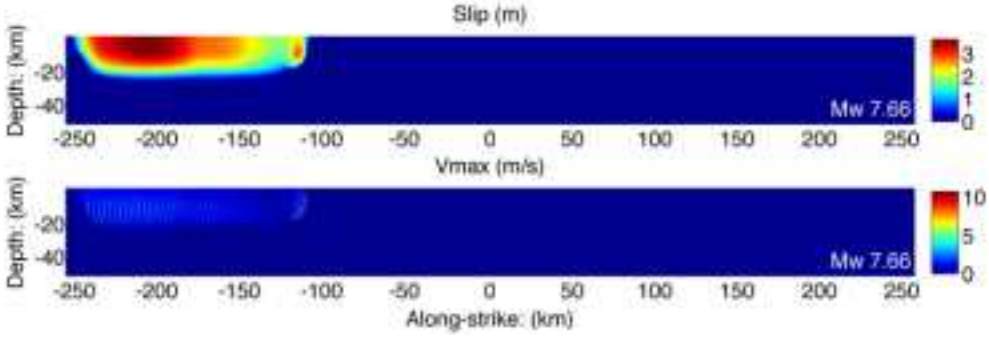

File_ID Magnitude Duration
25 7.64 48

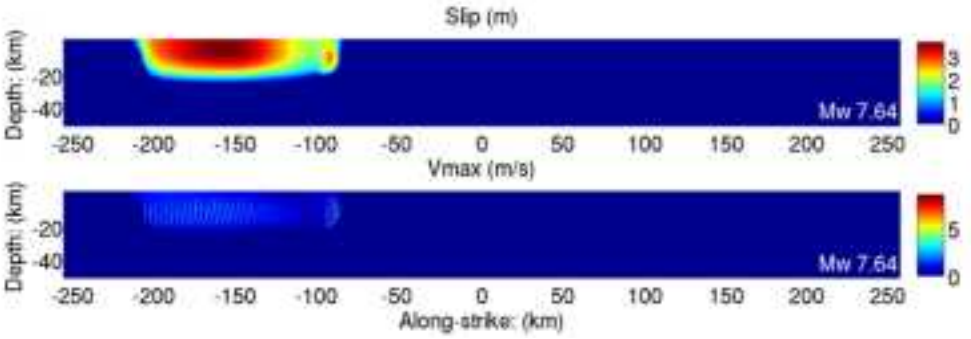

File_ID Magnitude Duration
45 7.63 48

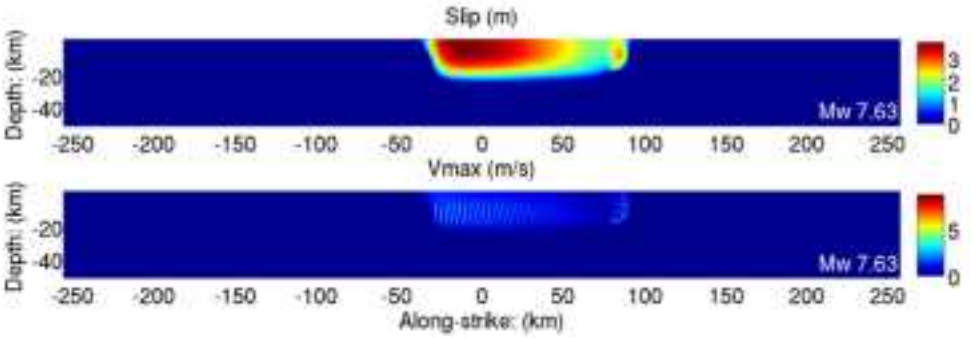

File_ID Magnitude Duration
44 7.62 47

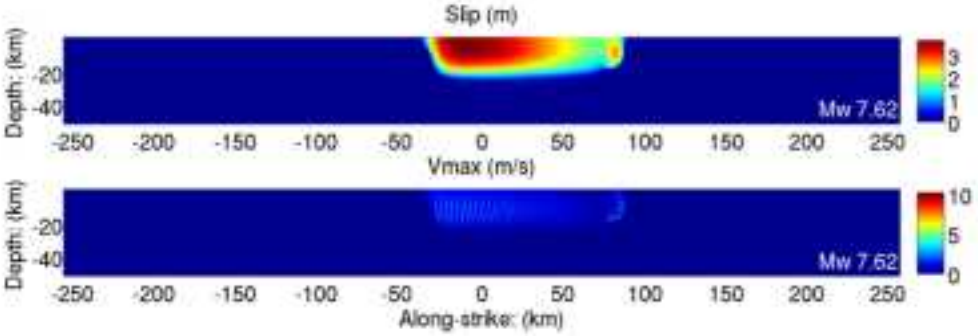

File_ID Magnitude Duration
43 7.62 47

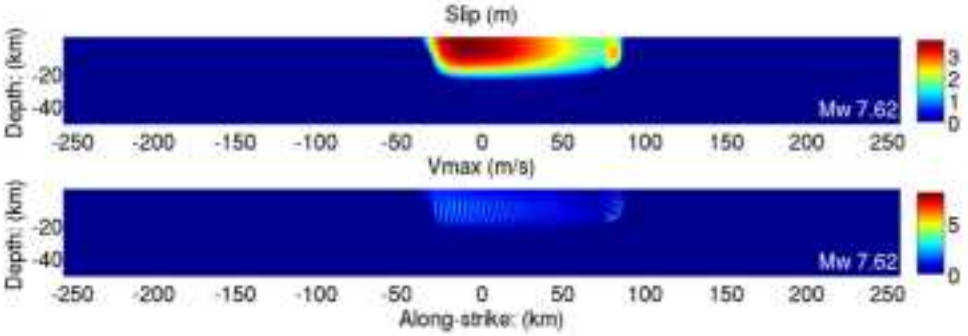

File_ID Magnitude Duration
50 7.61 47

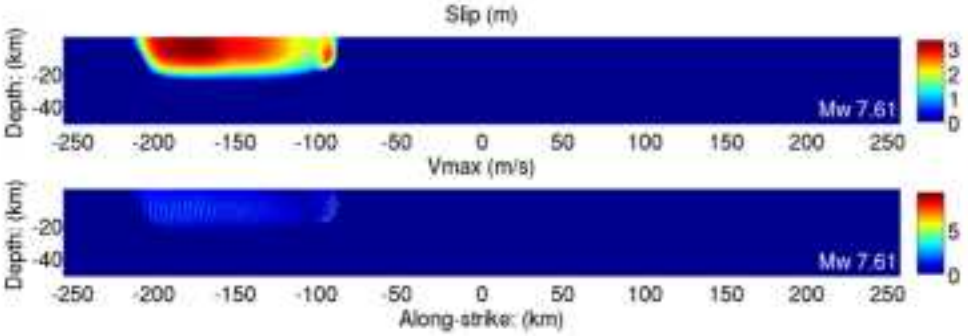

File_ID Magnitude Duration
67 7.60 44

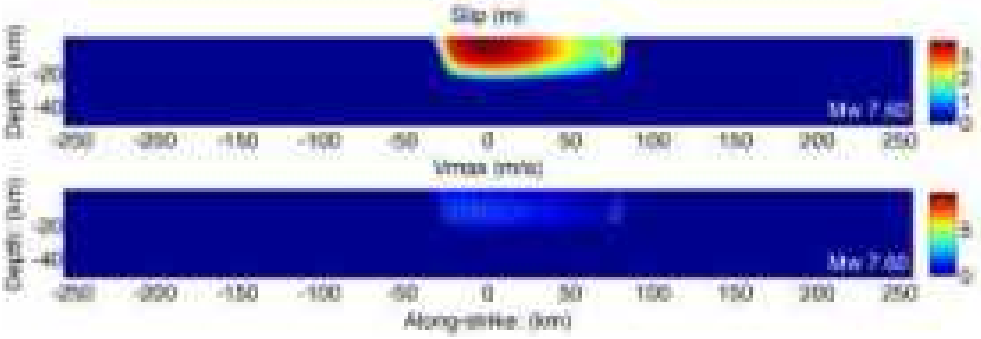

File_ID Magnitude Duration
87 7.60 44

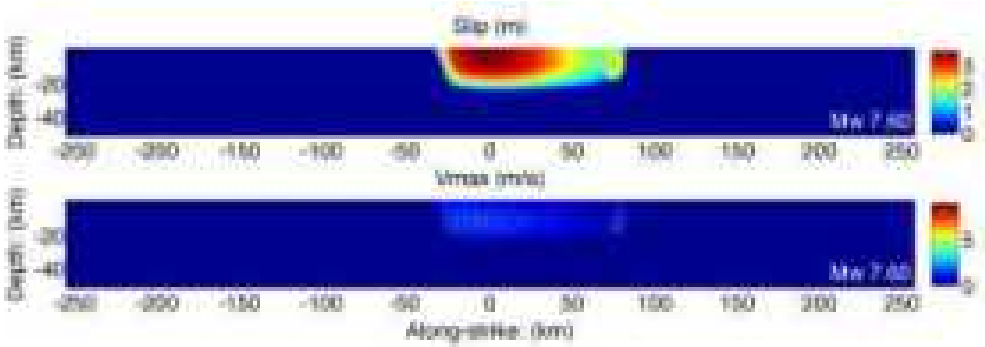

File_ID Magnitude Duration
42 7.59 44

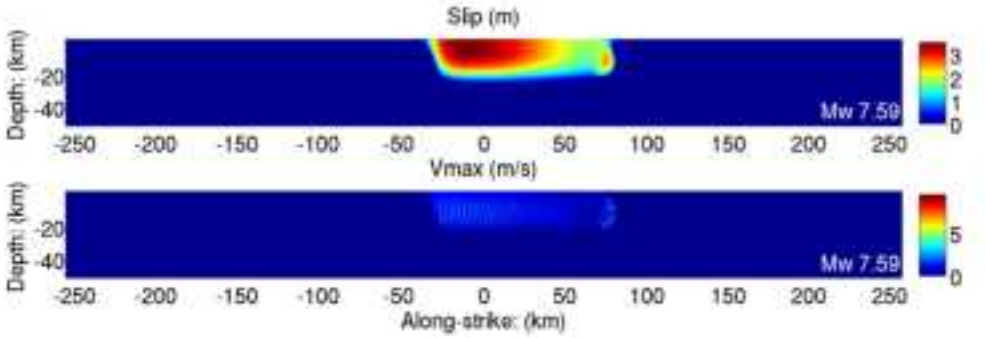

File_ID Magnitude Duration
66 7.59 43

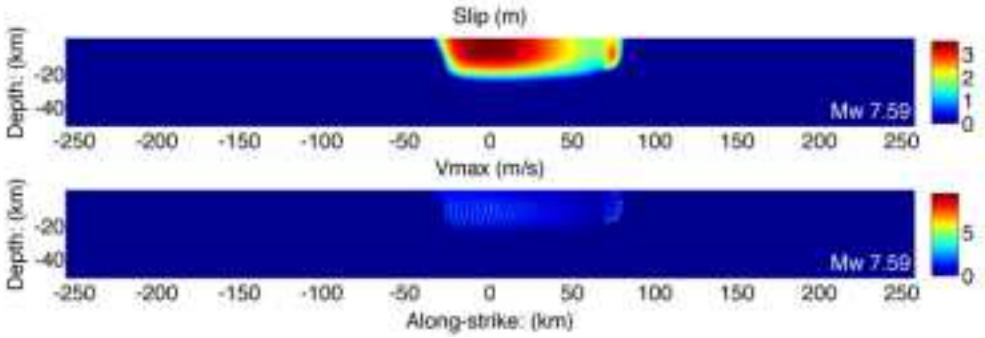

File_ID Magnitude Duration
24 7.58 43

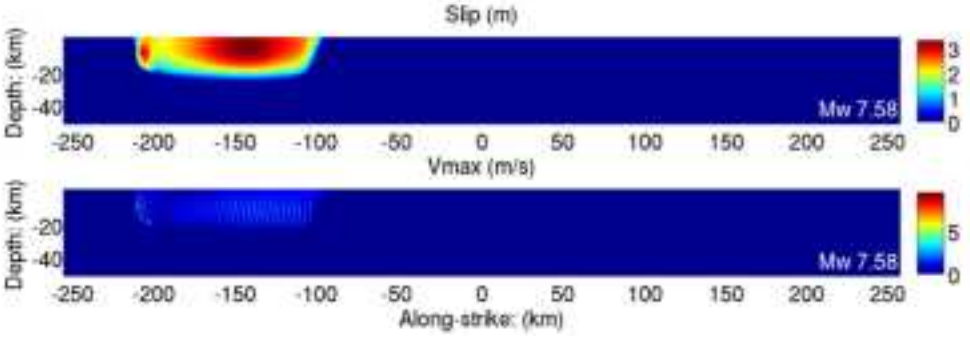

File_ID Magnitude Duration
49 7.58 46

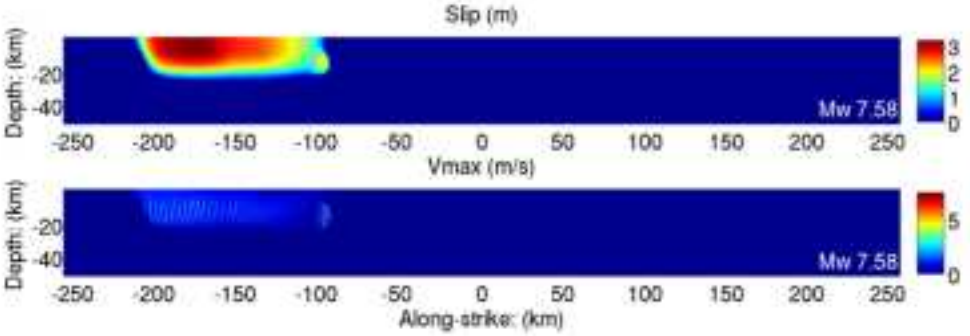

File_ID Magnitude Duration
79 7.56 44

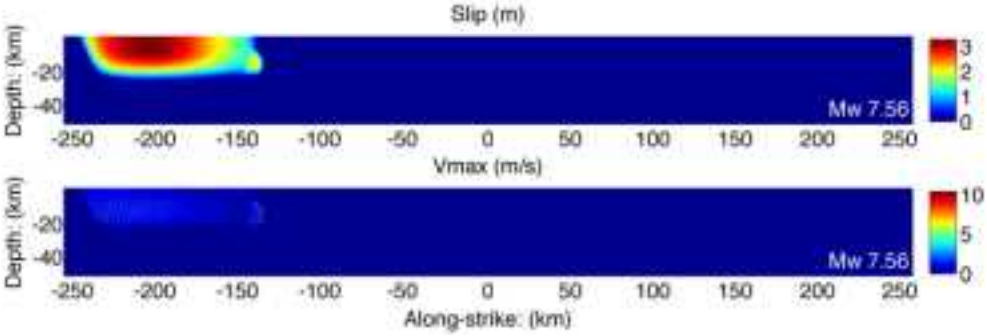

File_ID Magnitude Duration
78 7.55 41

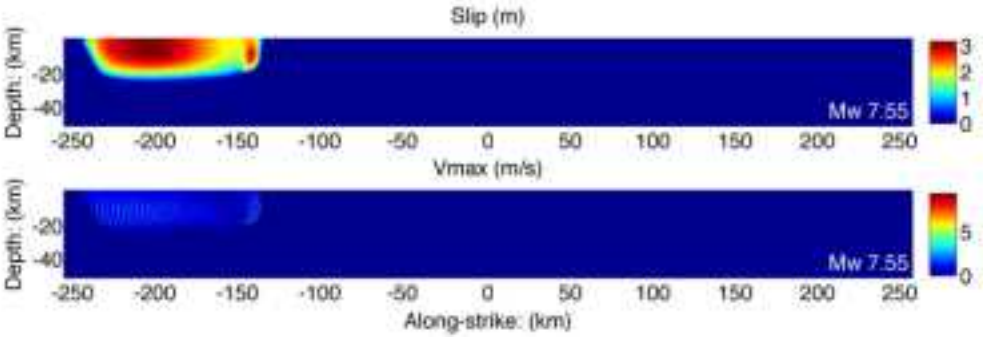

File_ID Magnitude Duration
12 7.55 40

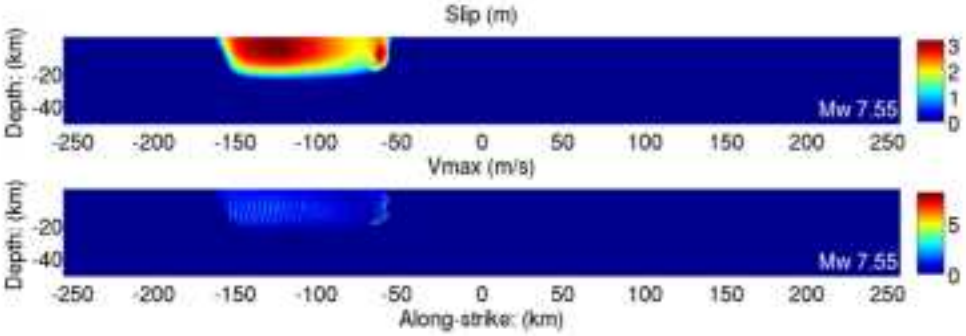

File_ID Magnitude Duration
23 7.55 41

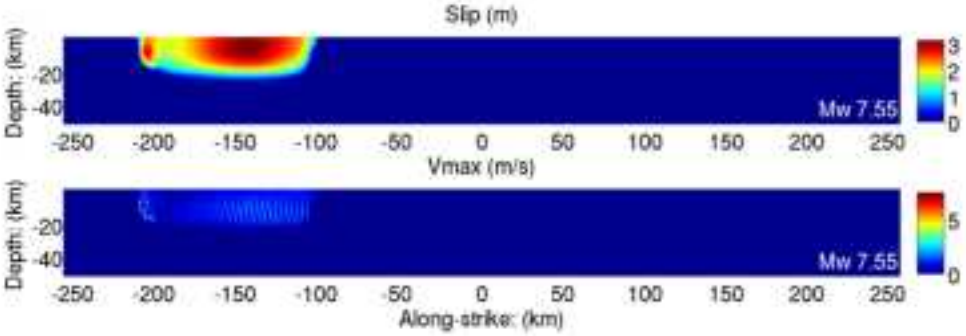

File_ID Magnitude Duration
22 7.55 41

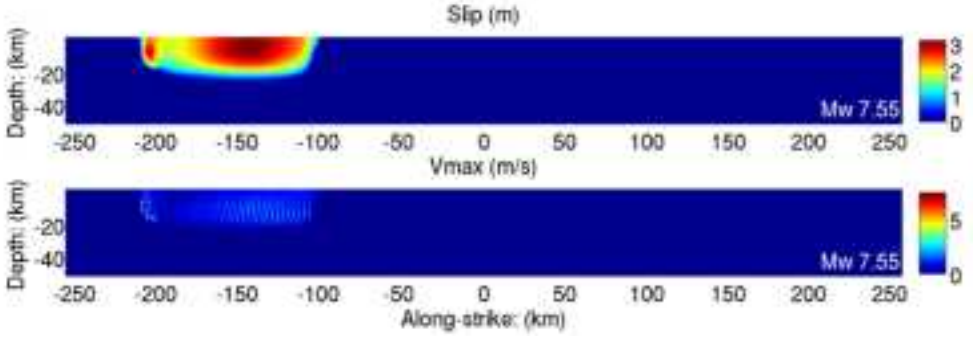

File_ID Magnitude Duration
65 7.55 39

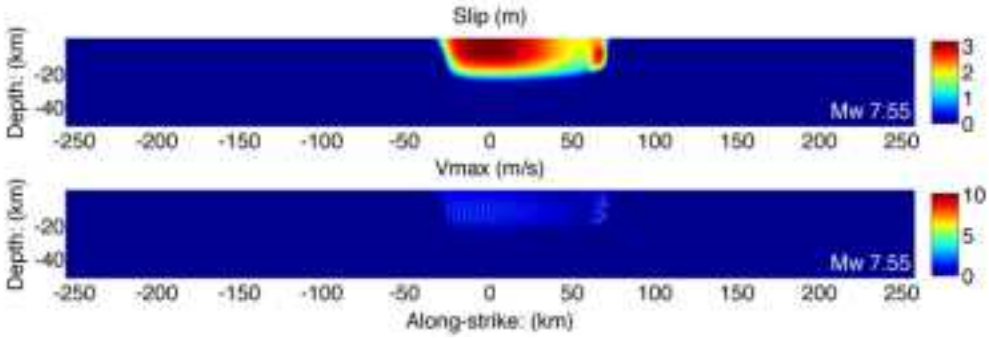

File_ID Magnitude Duration
82 7.54 50

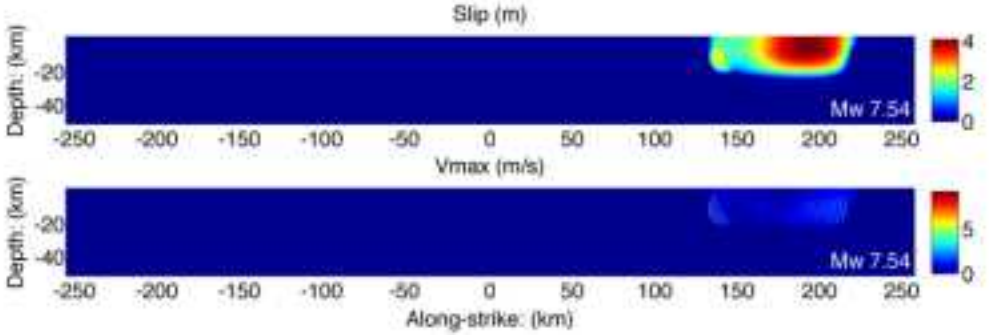

File_ID Magnitude Duration
64 7.53 39

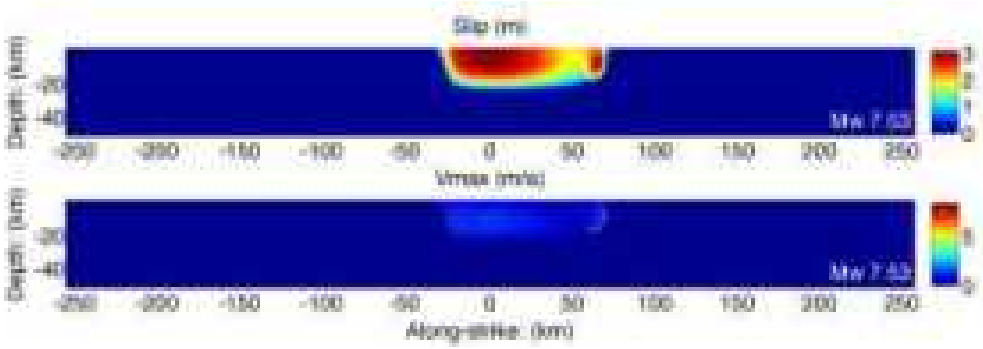

File_ID Magnitude Duration
84 7.53 39

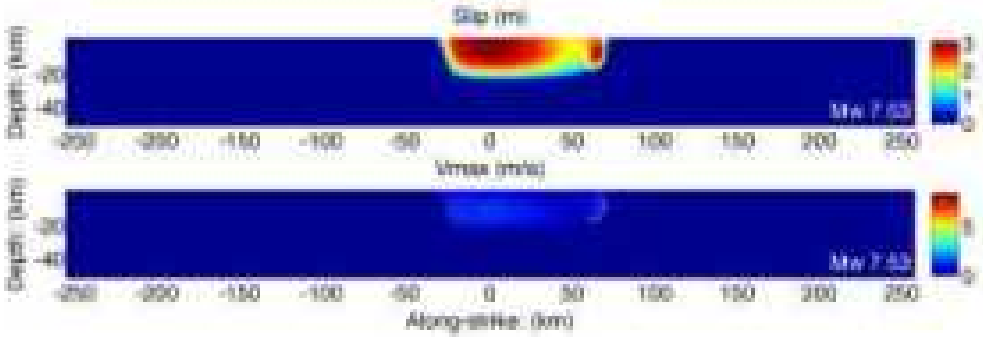

File_ID Magnitude Duration
77 7.51 38

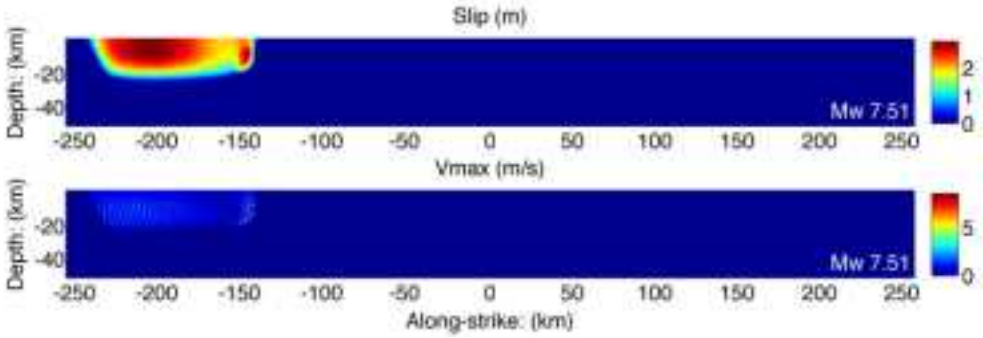

File_ID Magnitude Duration
41 7.51 39

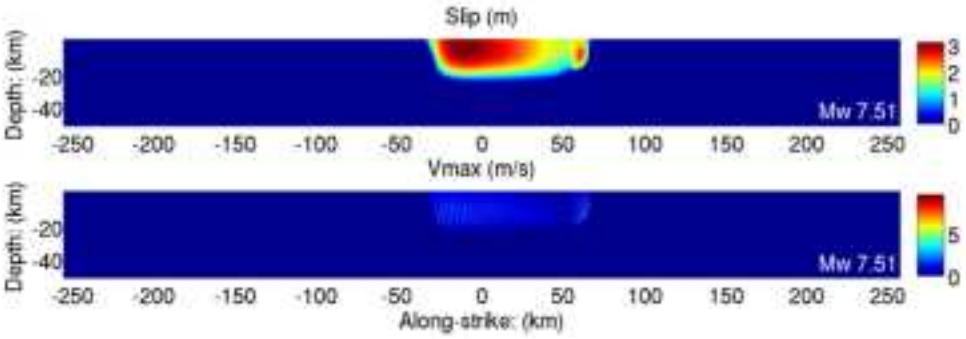

File_ID Magnitude Duration
56 7.50 39

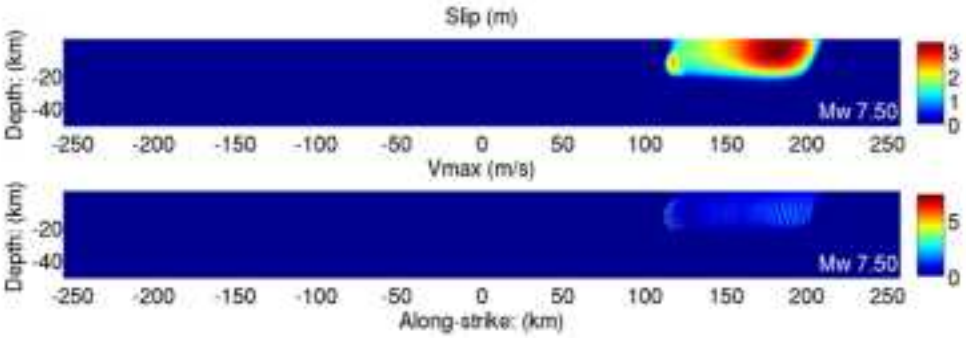

File_ID Magnitude Duration
40 7.50 38

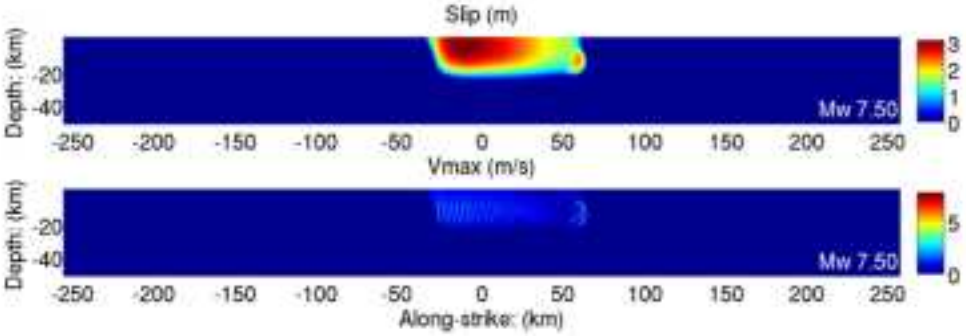

File_ID Magnitude Duration
63 7.50 37

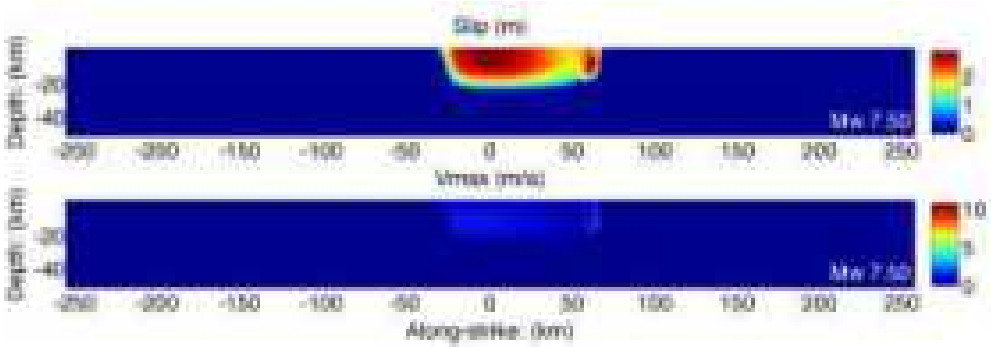

File_ID Magnitude Duration
83 7.50 37

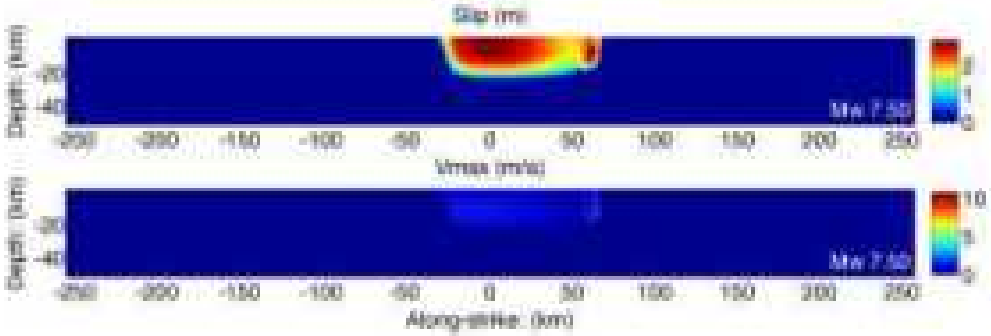

File_ID Magnitude Duration
54 7.49 36

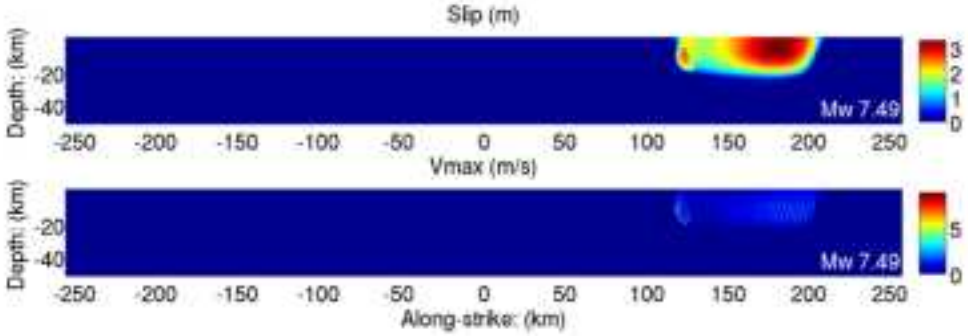

File_ID Magnitude Duration
55 7.49 37

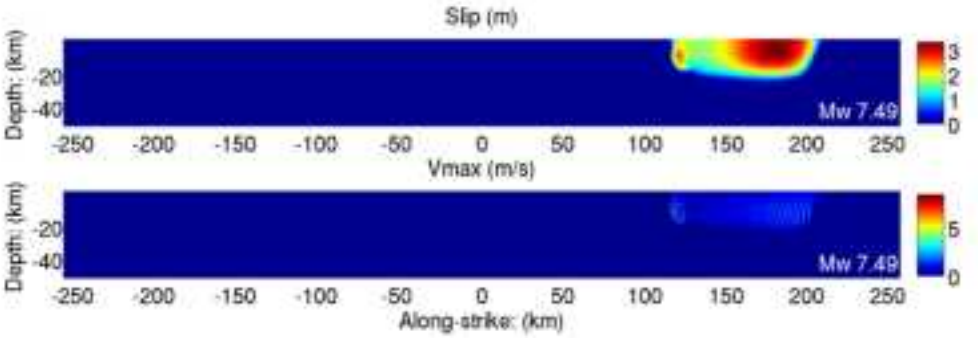

File_ID Magnitude Duration
85 7.49 37

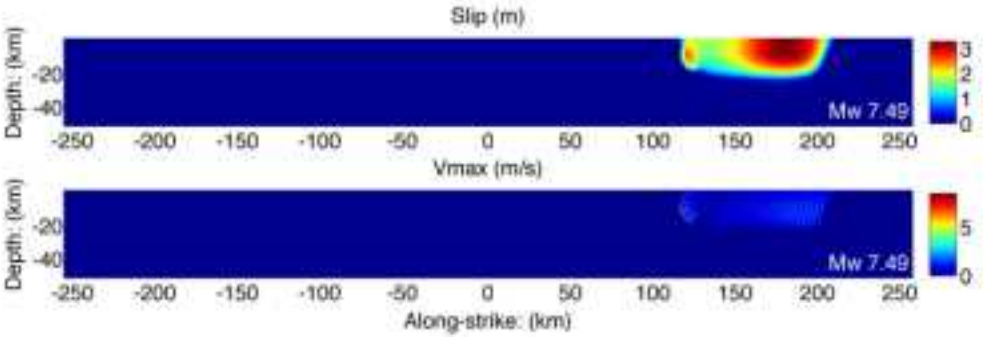

File_ID Magnitude Duration
53 7.48 37

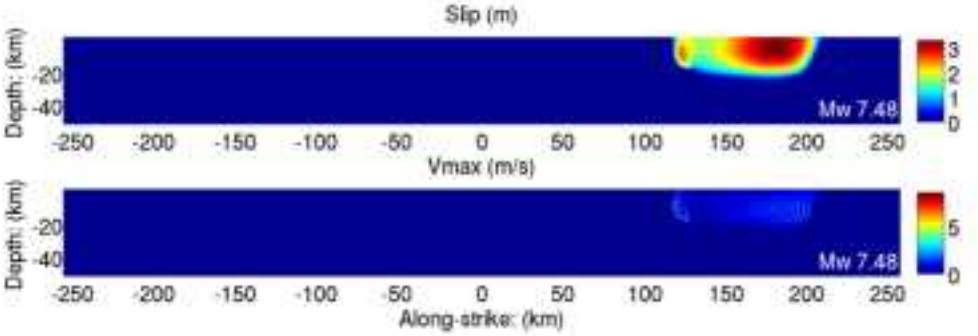

File_ID Magnitude Duration
51 7.48 36

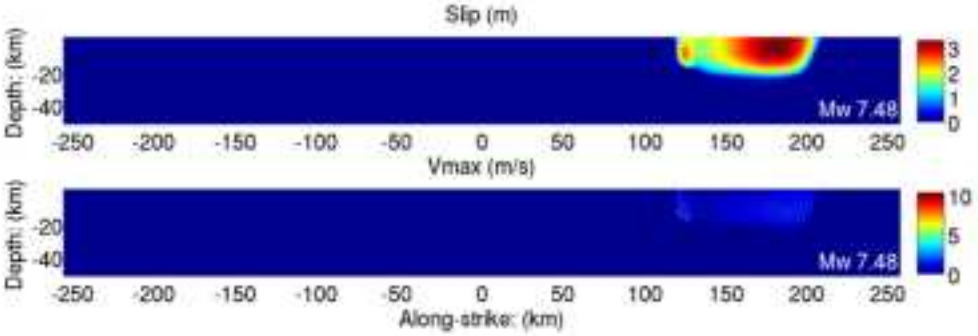

File_ID Magnitude Duration
76 7.48 36

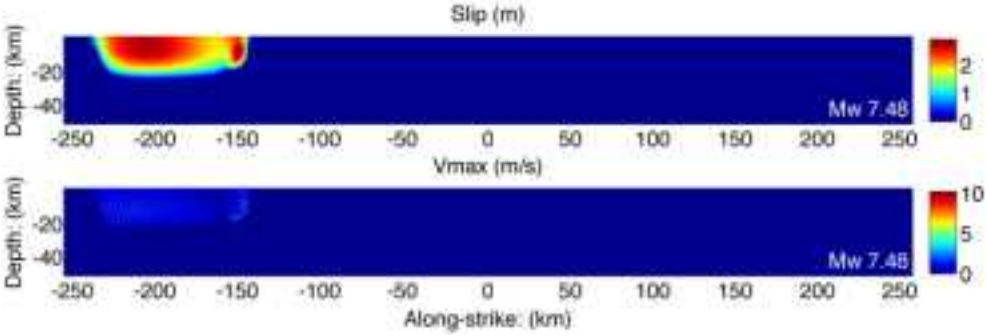

File_ID Magnitude Duration
75 7.47 36

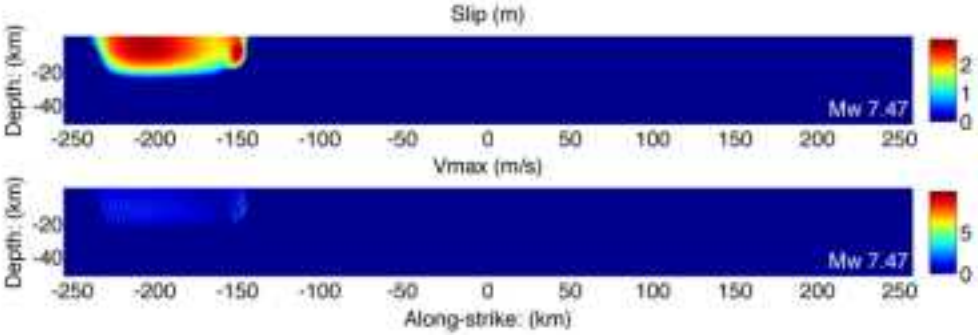

File_ID Magnitude Duration
52 7.47 37

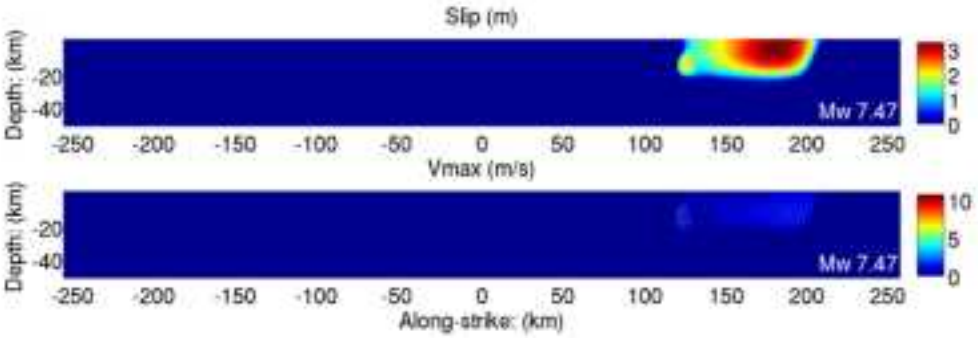

File_ID Magnitude Duration
74 7.44 34

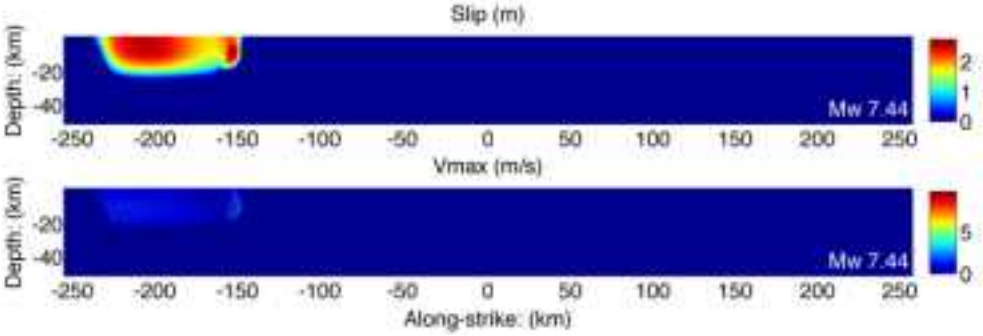

File_ID Magnitude Duration
39 7.43 33

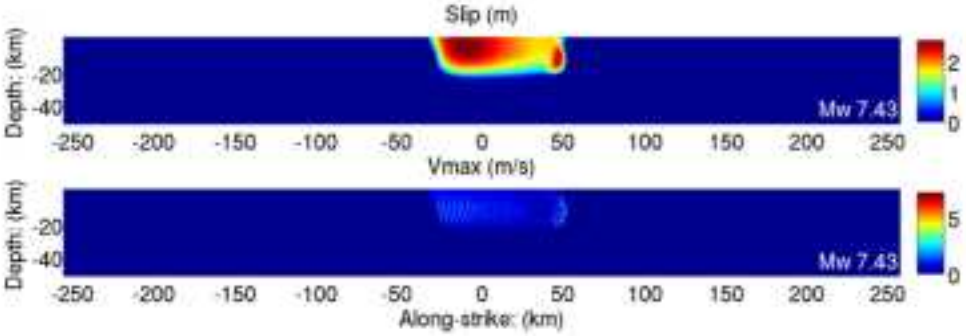

File_ID Magnitude Duration
15 7.38 30

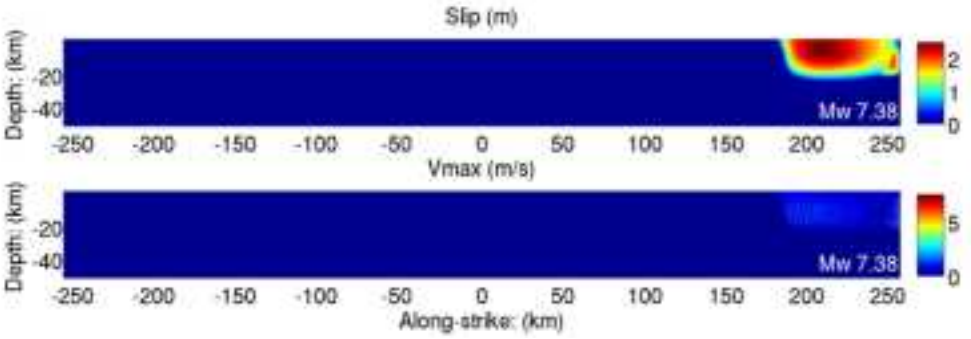

File_ID Magnitude Duration
31 7.37 30

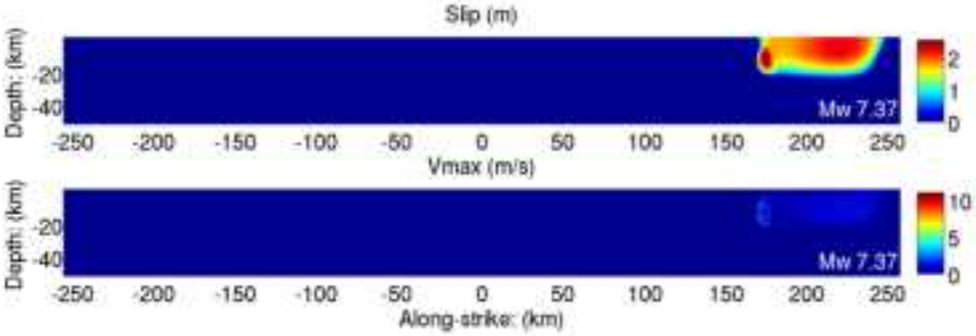

File_ID Magnitude Duration
38 7.37 30

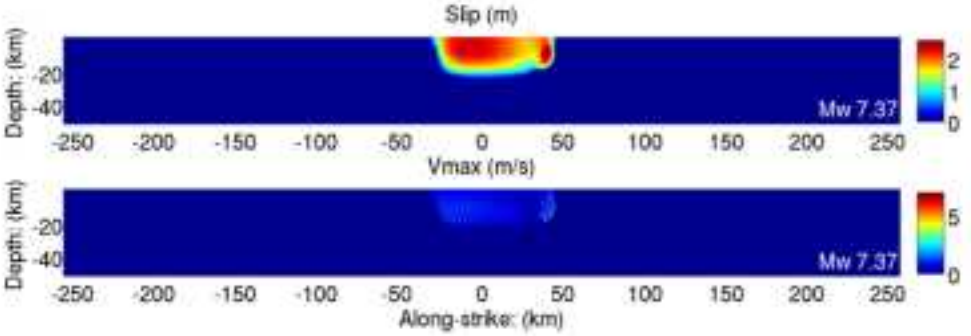

File_ID Magnitude Duration
37 7.37 29

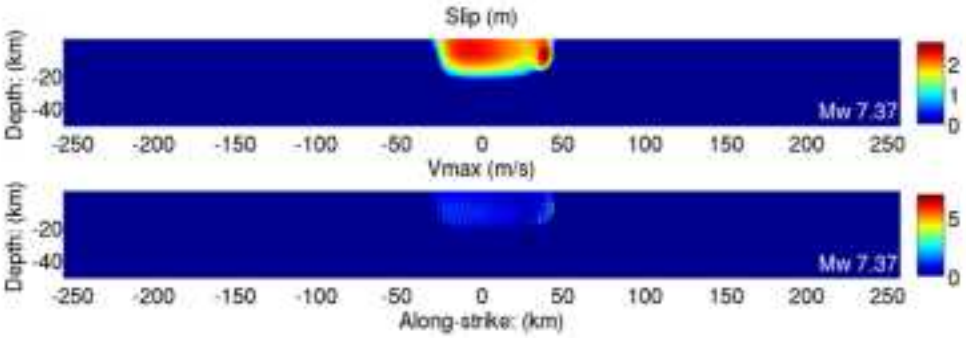

File_ID Magnitude Duration
13 7.36 31

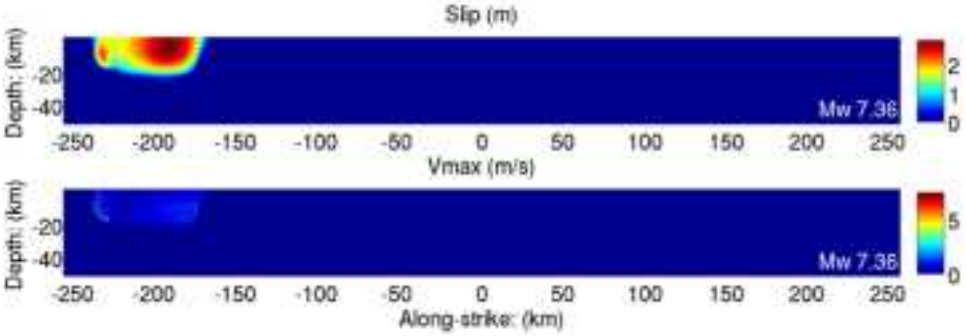

File_ID Magnitude Duration
36 7.36 27

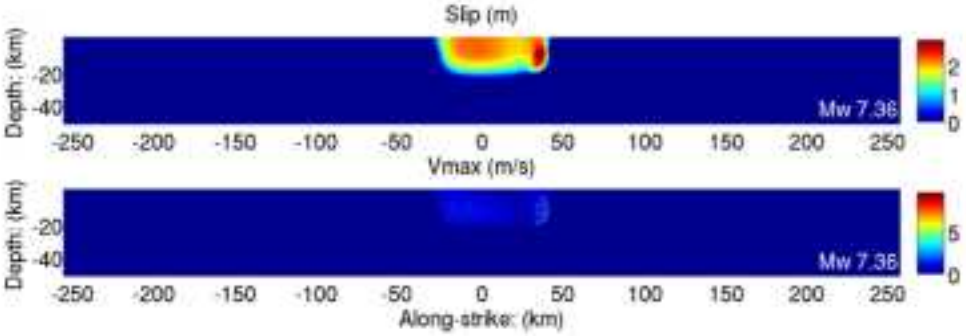

File_ID Magnitude Duration
90 7.34 26

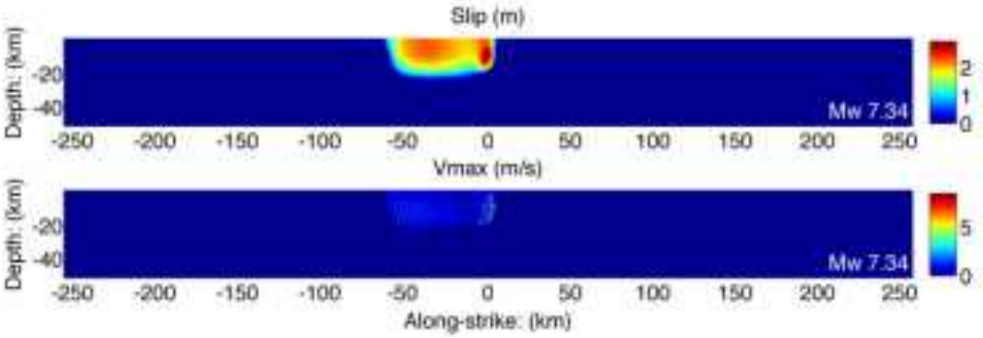

File_ID Magnitude Duration
35 7.34 27

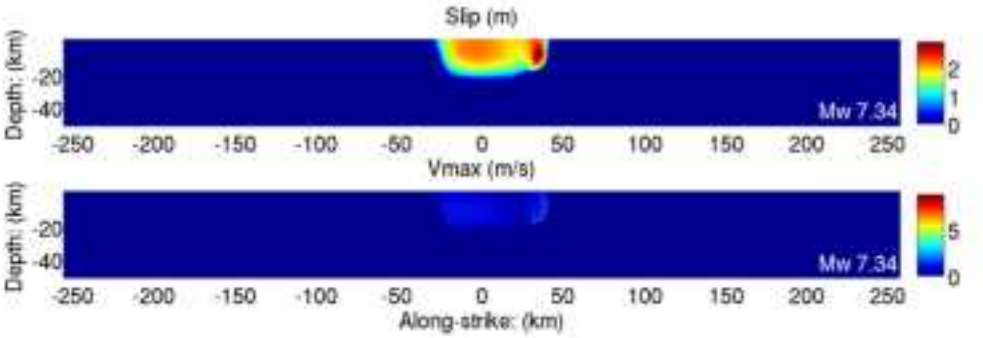

File_ID Magnitude Duration
89 7.31 24

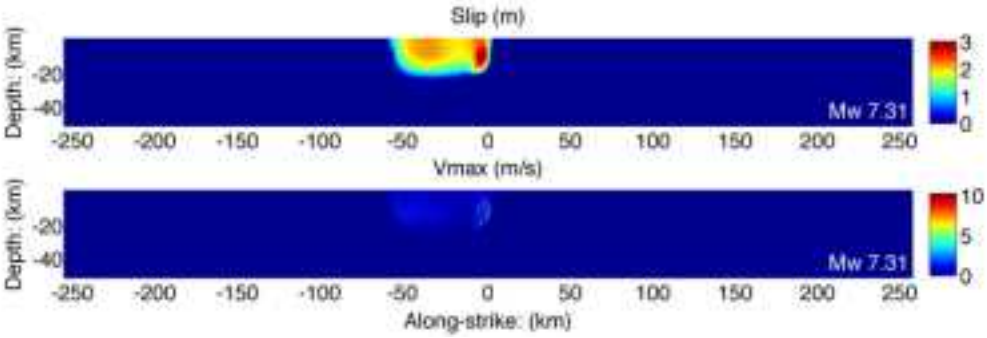

File_ID Magnitude Duration
62 7.31 27

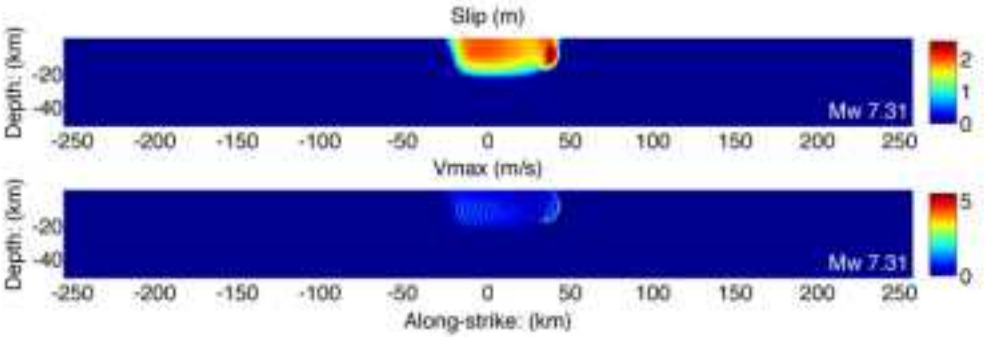

File_ID Magnitude Duration
61 7.30 25

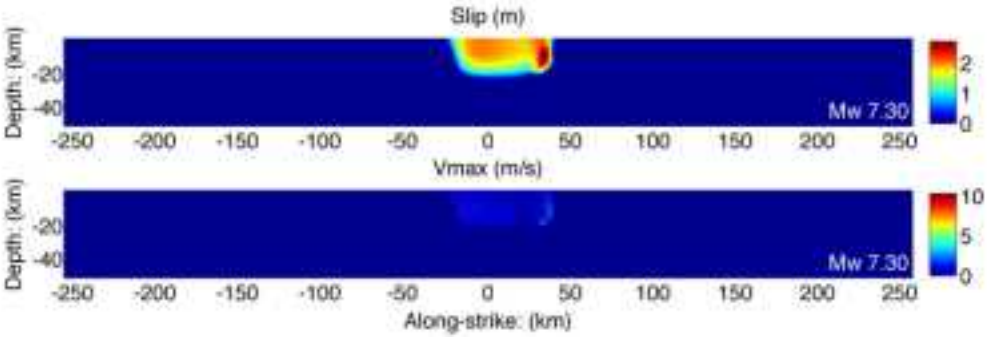

File_ID Magnitude Duration
48 7.28 25

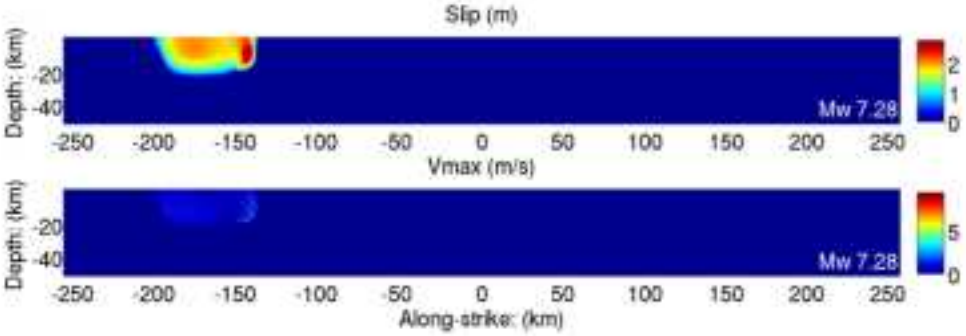

File_ID Magnitude Duration
34 7.27 24

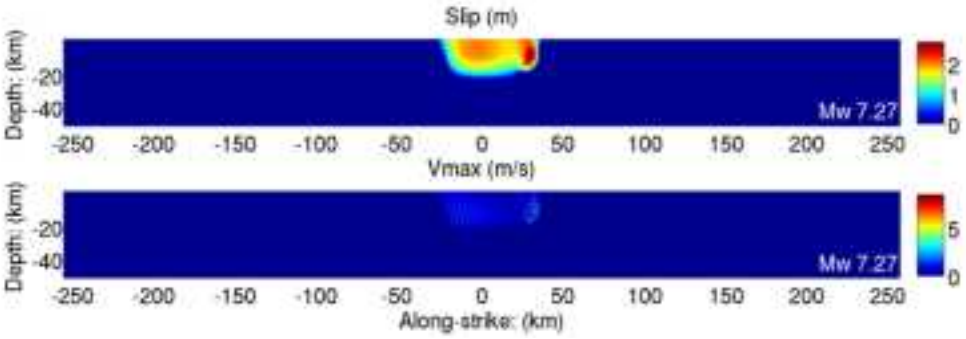

File_ID Magnitude Duration
47 7.26 24

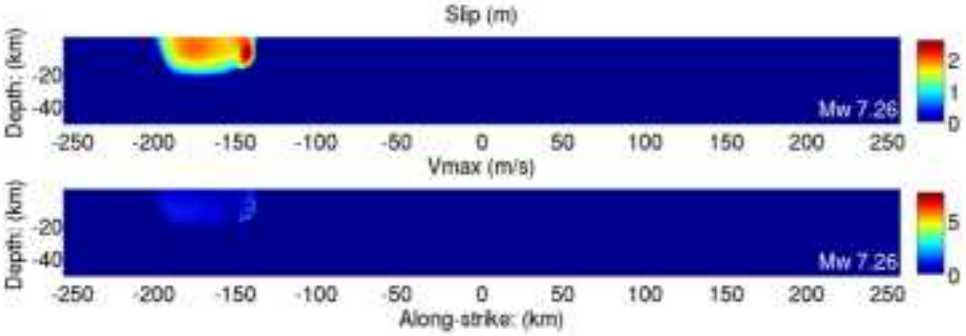

File_ID Magnitude Duration
33 7.26 22

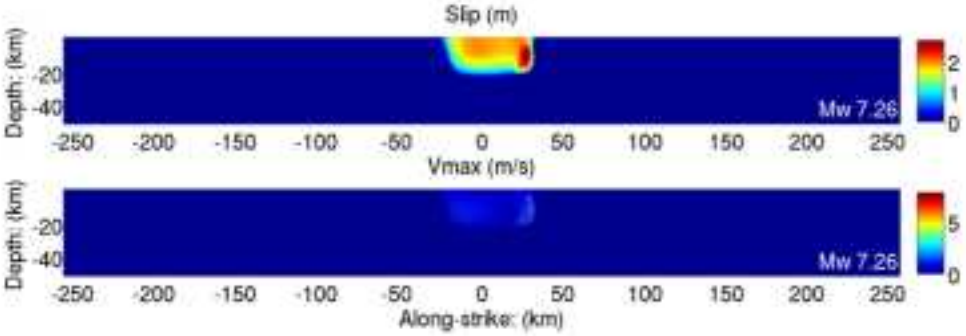

File_ID Magnitude Duration
60 7.25 24

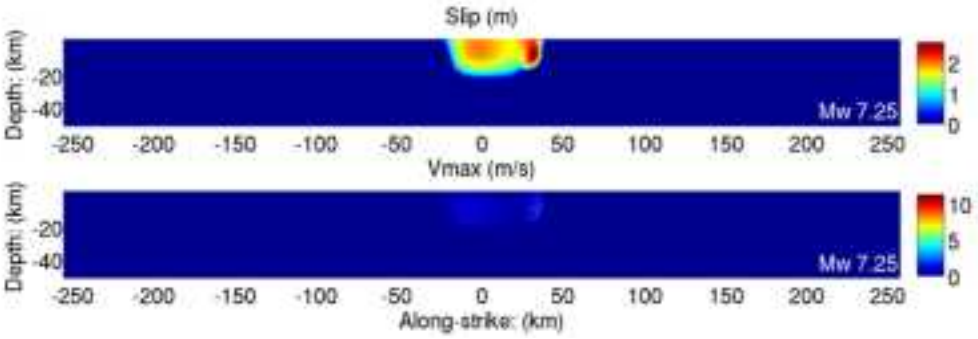

File_ID Magnitude Duration
59 7.25 23

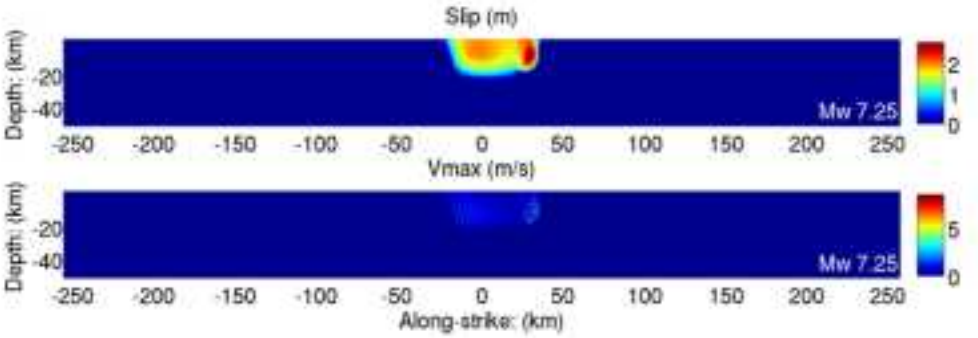

File_ID Magnitude Duration
17 7.24 23

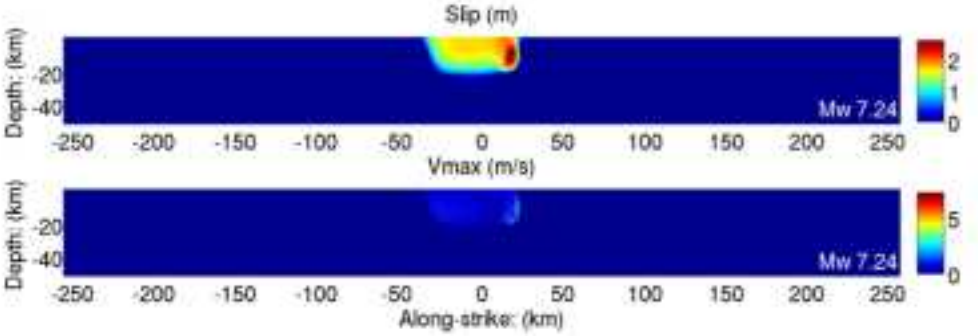

File_ID Magnitude Duration
58 7.23 22

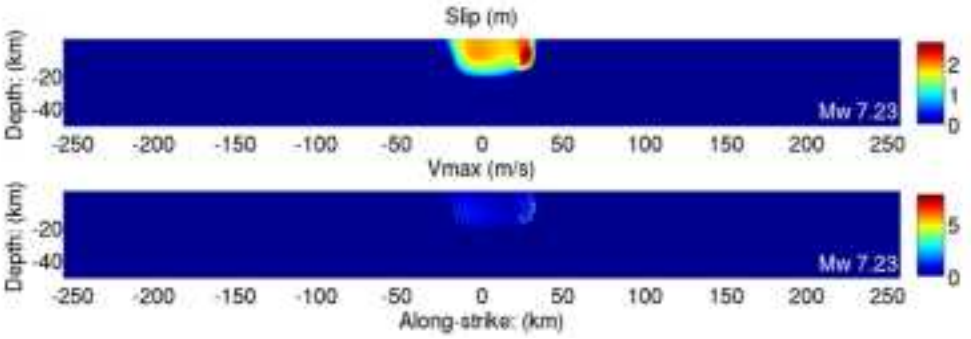

File_ID Magnitude Duration
86 7.22 25

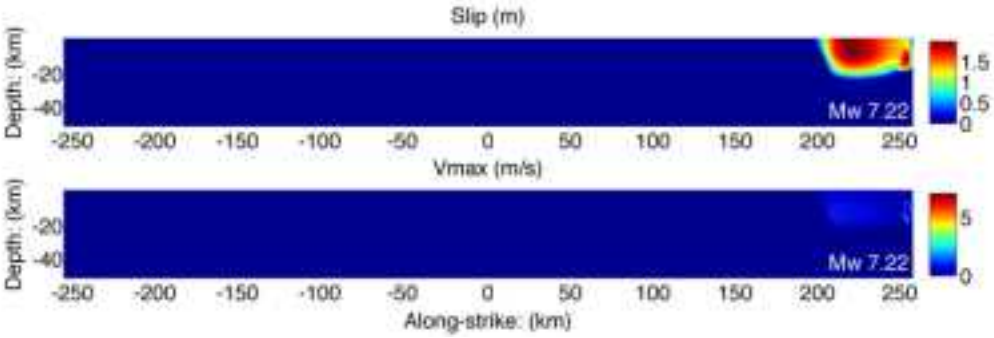

File_ID Magnitude Duration
69 7.22 21

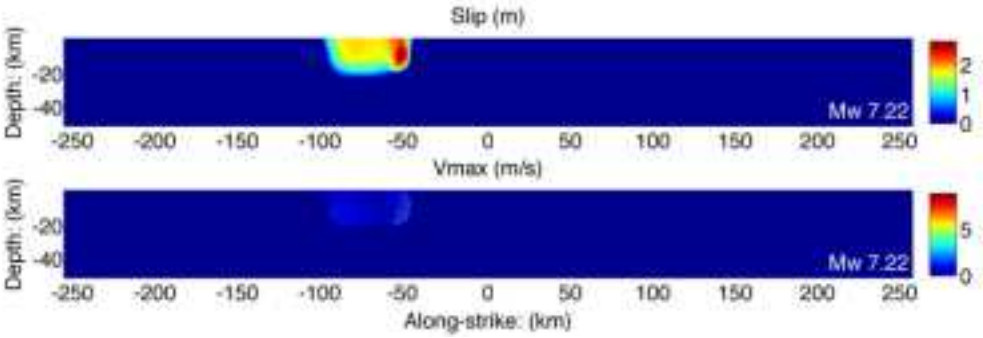

File_ID Magnitude Duration
11 7.22 22

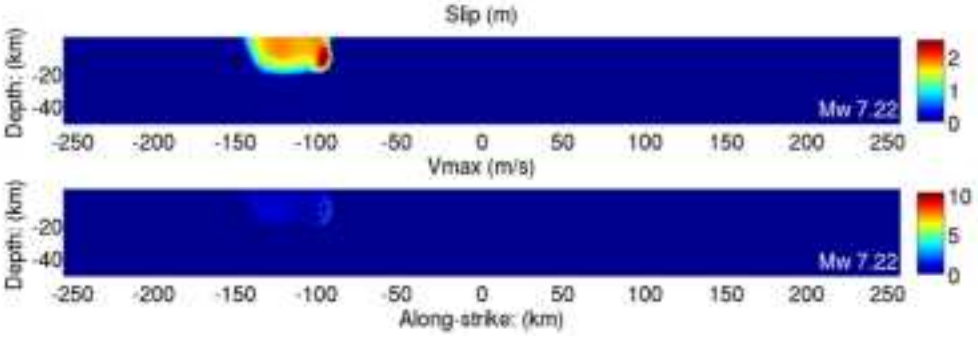

File_ID Magnitude Duration
16 7.22 22

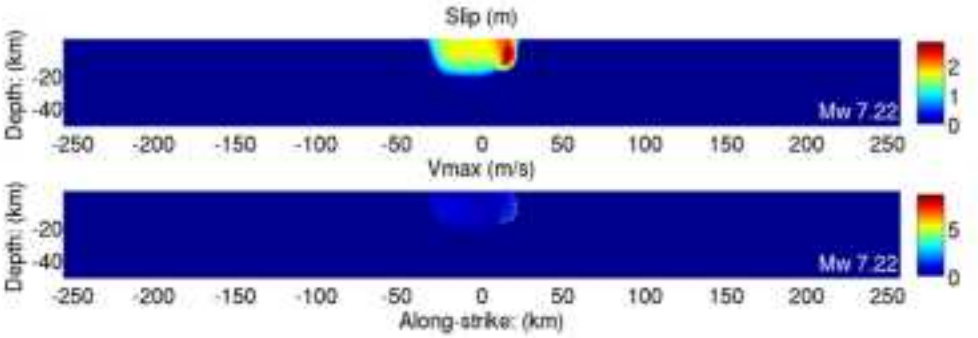

File_ID Magnitude Duration
32 7.21 21

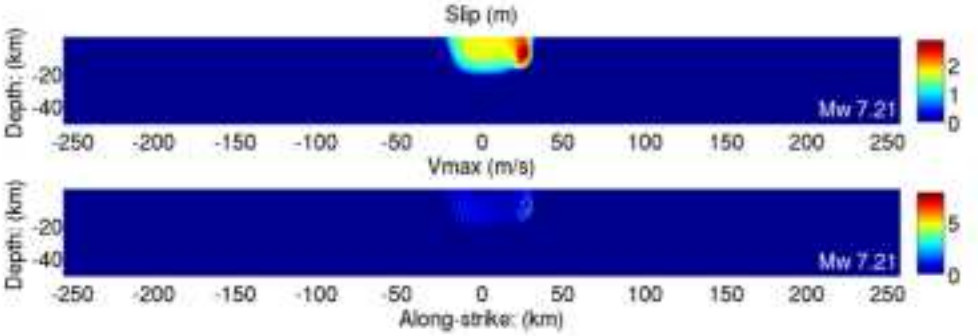

File_ID Magnitude Duration
57 7.20 20

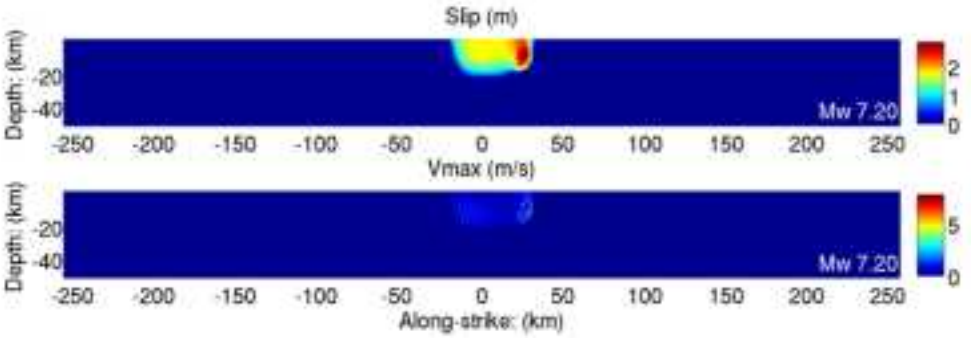

File_ID Magnitude Duration
10 7.20 22

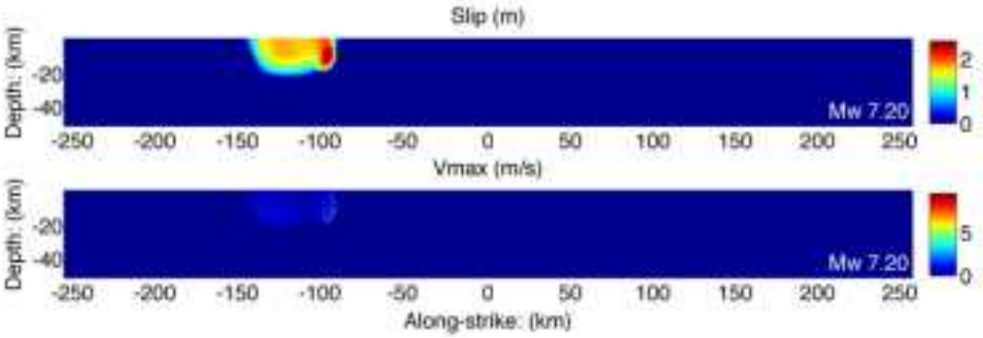

File_ID Magnitude Duration
9 7.19 20

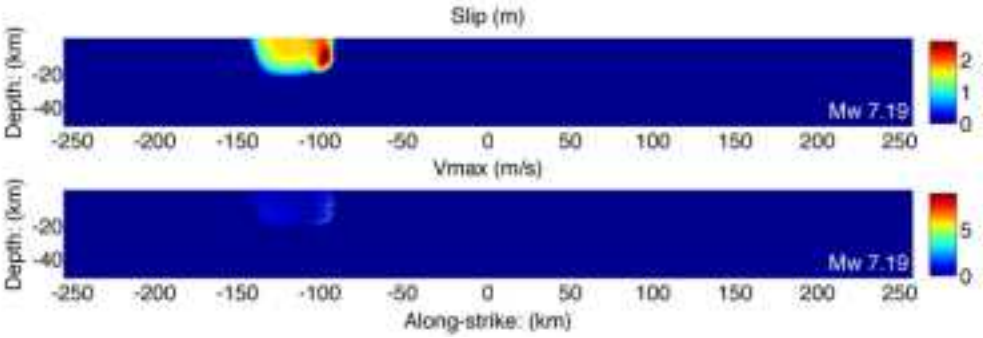

File_ID Magnitude Duration
21 7.18 20

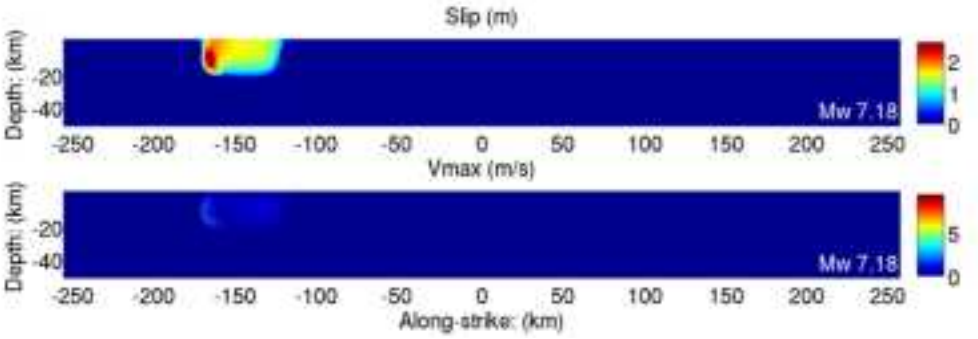

File_ID Magnitude Duration
30 7.17 21

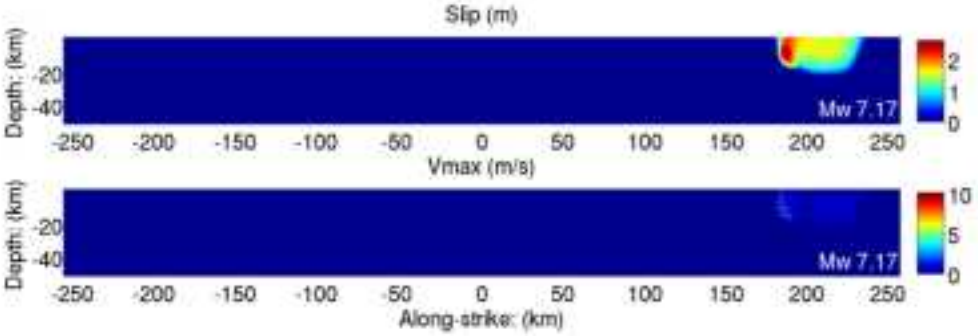

File_ID Magnitude Duration
72 7.17 21

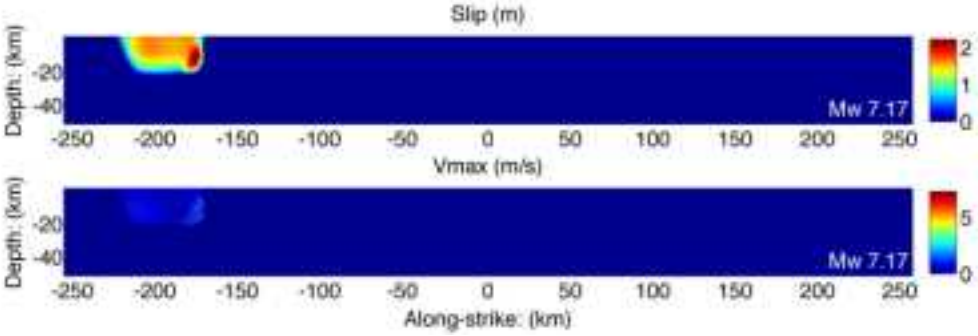

File_ID Magnitude Duration
73 7.17 21

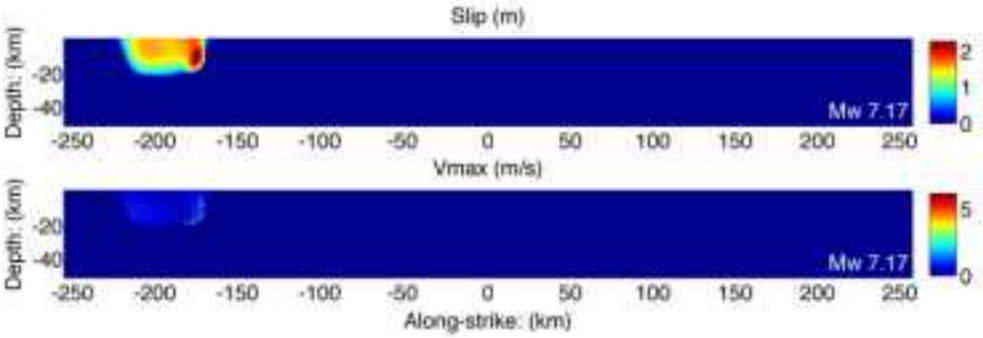

File_ID Magnitude Duration
71 7.16 21

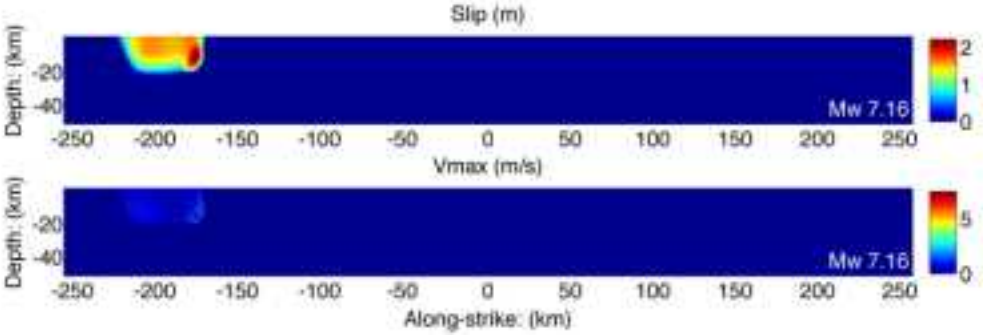

File_ID Magnitude Duration
29 7.16 19

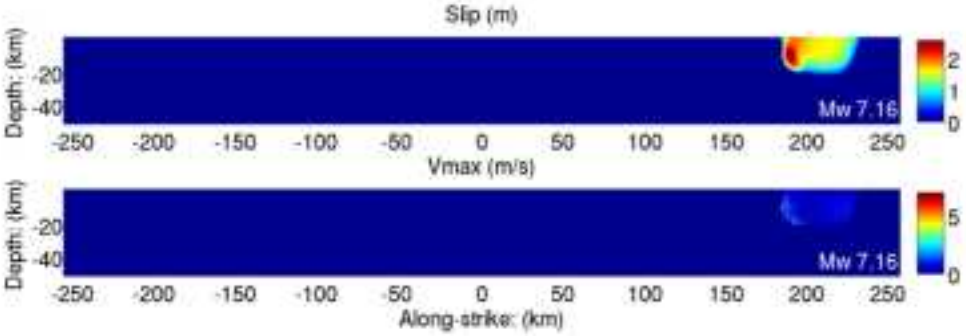

File_ID Magnitude Duration
70 7.14 20

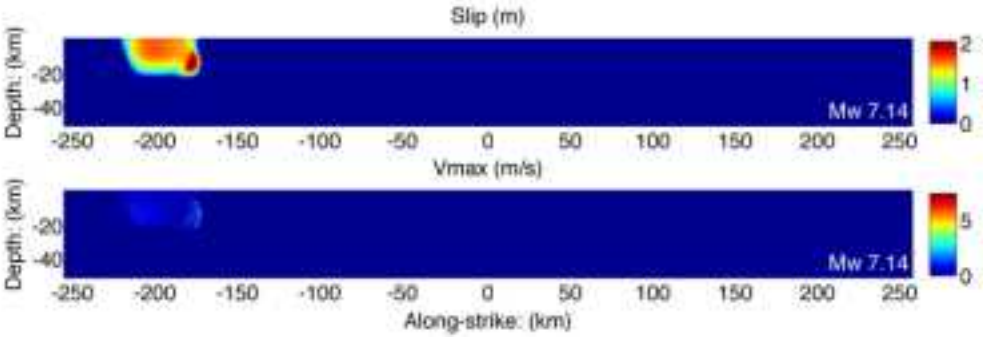

File_ID Magnitude Duration
28 7.12 18

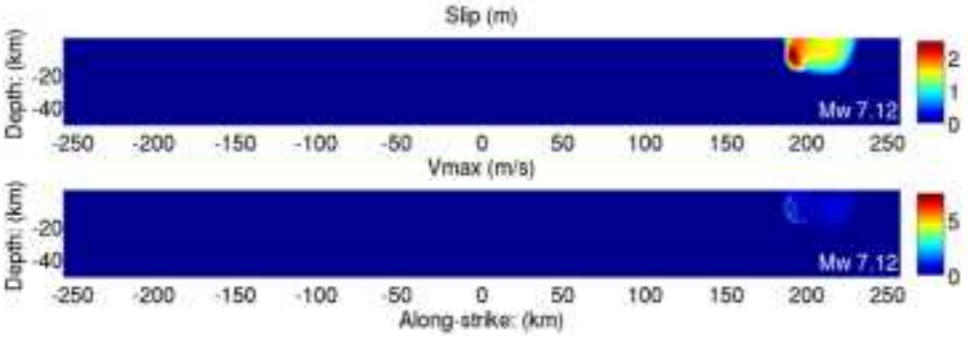

File_ID Magnitude Duration
14 7.03 18

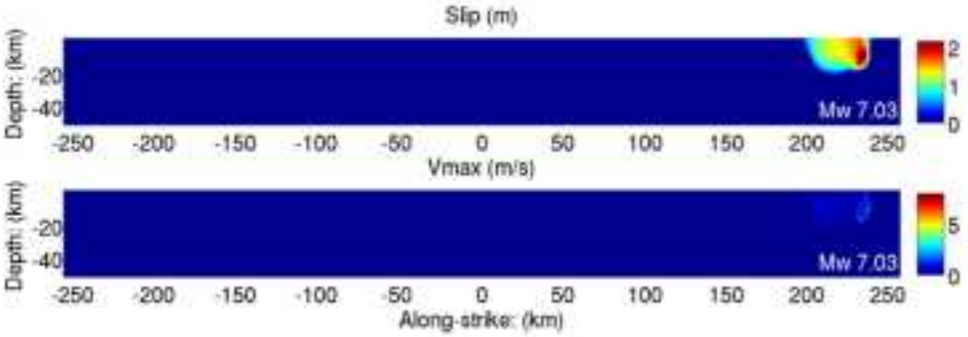

Appendix D. Spatial cross-correlation between slip and peak slip rate.